5-2015

Characterization of Mechanically Cooled High Purity Germanium (HPGe) Detectors at Elevated Temperatures

Joseph Benjamin McCabe
University of Tennessee - Knoxville, jmccabe2@vols.utk.edu

Recommended Citation

McCabe, Joseph Benjamin, "Characterization of Mechanically Cooled High Purity Germanium (HPGe) Detectors at Elevated Temperatures. " PhD diss., University of Tennessee, 2015.
https://trace.tennessee.edu/utk_graddiss/3350

To the Graduate Council:

I am submitting herewith a dissertation written by Joseph Benjamin McCabe entitled "Characterization of Mechanically Cooled High Purity Germanium (HPGe) Detectors at Elevated Temperatures." I have examined the final electronic copy of this dissertation for form and content and recommend that it be accepted in partial fulfillment of the requirements for the degree of Doctor of Philosophy, with a major in Nuclear Engineering.

Jason Hayward, Major Professor

We have read this dissertation and recommend its acceptance:

Eric Lukosi, Howard Hall, Brian Wirth, Mariya Zhuravleva

Accepted for the Council:
Dixie L. Thompson

Vice Provost and Dean of the Graduate School

(Original signatures are on file with official student records.)

Characterization of Mechanically Cooled High Purity Germanium (HPGe) Detectors at Elevated Temperatures

A Dissertation Presented for the
Doctor of Philosophy
Degree
The University of Tennessee, Knoxville

Joseph Benjamin McCabe
May 2015

Acknowledgements

At this time I would like to acknowledge a number of individuals who have supported me along my journey.

First and foremost I would like to thank my major professor Dr. Jason Hayward. Dr. Hayward inherited an individual whose background was primarily focused in mechanical engineering and in particular in electromechanical systems. My transition from electric motors and generators to radioisotope identification devices was assisted greatly by Dr. Hayward's guidance and support. Dr. Hayward was always willing to meet me in Oak Ridge, TN to review my research and assist in developing the plans and strategy necessary to succeed in achieving my Doctor of Philosophy in Nuclear Engineering objective.

Next, I would like to thank the staff at ORTEC with particular gratitude towards Mr. Frank Vorwald. Frank has supported my every endeavor and has been instrumental in helping shaping my career. He has offered me much advice on not only work but also life. He has taught me that professionalism and a genuine interest in people are both attributes that one should maintain inside and outside of work.

I would like to thank Pat and Kathleen McCabe. My parents gave me the greatest gift that any parent can ever give their child. They instilled in me that there is nothing that cannot be achieved if you are willing to commit to the goal. Anything is possible if you are willing to invest the time and energy towards that objective. Life is limited only by your imagination and perseverance. Small minds believe otherwise.

Finally, I would like to thank my loving wife Virginia and daughter Gisele who are the inspiration of my life. Virginia has supported my work and research regardless of the time of day or holiday that it may have happened to fall on. Gisele; may you look at life

with the same wonder, awe, and ambition that I still see every day and may you go on to decide to change the world.

Abstract

High resolution gamma spectroscopy is a tool used in nuclear security applications due to its achievable energy resolution and associated ability to identify special nuclear material. This identification ability is achieved by identifying the characteristic gamma-rays of a material. The challenges that have confronted industry concerning the use of hand-held high purity germanium (HPGe) in homeland security applications have centered on weight, geometry, and cool-down time. Typical liquid nitrogen cooled detectors ranging in size from 10% to 150% detectors will cool down sufficiently within 2-6 hours of filling. The cool-down time achieved in this research ranges from 45 min on the smallest detector to six hours on the largest 180 cm^3 detector; which is consistent with typical hand held HPGe devices. The weight and package geometry for HPGe-based designs is driven by the need to cool the HPGe detector to cryogenic temperatures. This is due to small bandgap (~0.7 eV) of HPGe. Liquid nitrogen or mechanical cooling is required to achieve such temperatures.

This dissertation presents work performed to characterize energy resolution performance as a function of temperature in a new mechanically cooled HPGe detector design based upon a split-Stirling cryocooler. This research also quantifies the microphonic noise contribution from this cryocooler. Measurements have been taken on detector sizes ranging from 6.75 cubic centimeters to 180 cubic centimeters. Focus has been placed on determining volume dependence on energy resolution at elevated temperatures. Microphonic noise contribution from the cooler has also been studied over the same temperature range. This energy resolution degradation was most pronounced at low temperatures (<110ºKelvin) and has been shown to be a function of cooler drive voltage. This research shows that in some cases the energy resolution degradation observed can be as much as 1.5 kiloelectronvolts.

This differs from previous studies where detectors were liquid nitrogen cooled. This research is also an expansion of previous research in that the size of the detectors studied is larger than previous. Previously identified research is limited to 75 cubic centimeter volume detectors whereas detectors up to 180 cubic centimeters will be reviewed.

Preface

I would like to begin by providing clear delineation between the research that I have been conducting as a part of my effort towards my Doctor of Philosophy Degree at the University of Tennessee at Knoxville in Nuclear Engineering and the development work that I have been conducting over the past three years as a part of my current roles and responsibilities as Division Vice President of Research and Development at Advanced Measurement Technologies Inc. with the ORTEC Business Unit. Although the work for each is related, upon recommendations of Dr. Hall and the balance of my PhD review committee, I will be taking measures in this dissertation to ensure that there is clear delineation between the two. This will ensure that there is no conflict of interest between the University of Tennessee at Knoxville and The Advanced Measurement Technologies Inc. organization. In addition, all intellectual property associated with the specifics of the design remain the sole ownership of Advanced Measurement Technologies Inc. and will be intentionally absent from this dissertation. What will be included, however, and specifically detailed are the fundamental research and contributions made to general nuclear engineering academia.

The primary objective in my research at the University of Tennessee *and* my research and development at ORTEC has been to fundamentally advance knowledge affecting the manner in which high purity germanium can be deployed in Homeland Security applications with a specific focus on radioisotope identification devices (RIIDs). This includes a specific focus on achieving an order of magnitude reduction in the overall weight of the RIID as compared to the current, commercially available state-of-the art devices. Specific development efforts related to the cryostat/detector assembly are the facilitator to achieving this goal. The temperature research and simultaneous examination of the microphonic effect of using mechanical cooling detailed as a part of this dissertation both provide interesting challenges that are fundamental to any new design. Care will be taken, however, to ensure that there is no company IP or design trade secrets are disclosed as a part of this dissertation. What can (and will) be disclosed are the basics of the design. This will include the primary sections of the detector and cryostat assembly.

Table of Contents

List of Tables

List of Figures

Chapter 1

Introduction

The nuclear security of the United States of America is dependent on the ability to detect and identify nuclear weapons and special nuclear material (SNM, including plutonium and certain types of uranium) [1]. The aforementioned detection and identification capability contributes directly to the ability to mitigate the illicit transportation and proliferation of special nuclear material. As a result, research and development in this area is becoming ever more critical.

The ability to detect and identify special nuclear material is made possible by the characteristic radiation (both type and energy) emitted by the radioactive isotope which may include uranium or plutonium [2]. Nuclear weapons require the presence of fissile material [3]. These are massive atoms that have the inherent capability of induced fission, the ability to split when struck by certain energetic particles including neutrons [4]. The fissile materials used in nuclear weapons are uranium (U-235) and plutonium (Pu-239). Weapons-grade plutonium (WGPu) is a mixture of isotopes containing at least 93% Pu-239 [5], and highly enriched uranium (HEU) is uranium enriched to at least 20% U-235 [6]. Although it may be possible to determine the presence of fissionable material through the measurement of coincident neutron emissions, it may also be possible to detect the presence of WGPu and HEU by the characteristic gamma emission of the plutonium and uranium isotopes, respectively [7].

Due to its excellent energy resolution and high efficiency for keV to MeV gamma rays, high purity germanium (HPGe) represents a superior detector material for gamma-ray spectroscopy. The resolution is especially important in the identification of special nuclear material in the scenarios identified above. Accordingly, this research is focused on HPGe detectors and their operational characteristics.

The current commercially available, state-of-the-art HPGe, RIID weighs approximately 15 pounds. The majority of the weight in an HPGe, handheld device resides primarily in the detector assembly (detector, embedded electronics, and associated cooling). Any significant advancement in reducing weight, therefore, requires specific focus in this area. If the overall heat load of the cryostat could be reduced, the size (and weight) of the cooler that would be required to cool the detector could be proportionately smaller. Further reductions in the weight associated in the cooling of the detector could be achieved, not only in reducing the heat load, but also in simultaneously increasing the detector operational temperature. This research will focus on the operation of HPGe detectors at elevated temperatures.

The infrared (IR) detection industry, which deals with many of the same detector challenges as seen in radiation/nuclear detection, has advanced in the direction of higher operating temperature detectors [8]. A class of higher operating temperature infrared detectors referred to as HOT (high operating temperature) detectors has already been an area of focus in the IR industry for some time [9]. Photon trap detectors on MBE HgCdTe/Si epitaxial wafers exhibit improved performance compared to single mesas, with measured noise equivalent difference temperature or NEDT [10] of 40 mK and 100 mK at temperatures of 180 K and 200 K, respectively, with good operability [11]. This work pursues the same type of higher operating temperature advancement in the area of radiation/nuclear detection with a specific focus on the mechanically cooled subset of the HPGe detection market.

Chapter 2

Background

2.1. Semiconductor Based Radiation Detectors

High Purity Germanium (HPGe) falls into the semiconductor class of detectors [12]. Prior to going into specific detail on HPGe detectors, this chapter will focus on semiconductor detector fundamentals and gamma-ray interaction in semiconductor detectors. A solid detection medium offers a number of advantages when considering gamma-ray detection and spectroscopy. One of these advantages is the higher density of solid state detectors as compared to gas or liquid-based detectors. For the same efficiency, this translates into much smaller detection systems. Another advantage of semiconductor-based detection is energy resolution. The best energy resolution from radiation spectrometers in routine use is achieved using semiconductor detectors. This is primarily due to the fact that with semiconductor detectors are capable of a much high number of carriers (electron-hole pairs in the case of semiconductor detectors) per radiation event than is possible with any other type of detector medium. The resolution capability of the detector, accordingly, is dependent on the number of carriers achieved per radiation event. In addition to superior resolution capability, semiconductor detectors also provide advantages including compact size and fast timing characteristics. Semiconductor based radiation detection devices have been used for over 50 years. Although the focus of this research is high purity germanium, other semiconductor materials used for radiation detector include silicon (Z=14), lead iodide (PbI_2), thallium bromide (TlBr), and CZT ($Cd_{1-x}Zn_xTe$) [13]. I have included table 1.1 as a reference of comparison of various semiconductor material characteristics.

Table 2.1: Properties of semiconductor materials [14].

Material	Z	Density (g/cm3)	Bandgap (eV)	Ionization Energy (eV per e-h pair)	Best Gamma-Ray Energy Resolution (FWHM)
Si (300 ºK)	14	2.33	1.12	3.61	
(77 ºK)	--	--	1.16	3.76	400 eV at 60 keV
(77 ºK)	--	--	--	--	550 eV at 122 keV
Ge (77 ºK)	32	5.33	0.72	2.98	400 eV at 122 keV
--	--	--	--	--	900 eV at 662 keV
--	--	--	--	--	1300 eV at 1332 keV
CdTe (300 ºK)	48/52	6.06	1.52	4.43	1.7 keV at 60 keV
--	--	--	--	--	3.5 keV at 122 keV
HgI2 (300 ºK)	80/53	6.4	2.13	4.3	3.2 keV at 122 keV
--	--	--	--	--	5.96 keV at 662 keV
$Cd_{0.8}Zn_{0.2}Te$ (300 ºK)	48/30/52	6	1.64	5.0	11.6 keV at 662 keV

2.2. Semiconductor Detector Characteristics

The performance capability of semiconductor detectors (resolution, fast timing, etc.) is a result of the crystalline, lattice structure of the material itself. This crystalline structure determines the allowable energy bands for electrons to exist within the material itself. The energy of any electron or hole within the semiconductor must be confined within one of these energy bands. Figure 2.1 provides a simplified representation and comparison of the energy band structure for electron energies between a semiconductor and insulator.

The lower band is referred to as the valence band and the upper band is referred to as the conduction band. The valance band corresponds to the outer shell electrons that are bound to specific lattice sites within the crystal. The alternate band shown in the simple representation is the conduction band. This band represents the energy levels that are free to migrate through the semiconductor. Electrons in the conduction band contribute to the electrical conductivity of the detector. The distance between the two aforementioned bands is termed the bandgap of the material which ultimately determines the classification of the material; semiconductor or insulator. In both insulators and semiconductors, the conductivity of the material is limited by that fact that the associated electrons must cross the bandgap to reach the conduction band. This band gap is shown in Figure 2.1. Typically, the bandgap is approximately 1 eV for a semiconductor [15]. The small bandgap is the primary reason why high purity germanium needs to be operated at cryogenic temperatures when operating as a radiation detector.

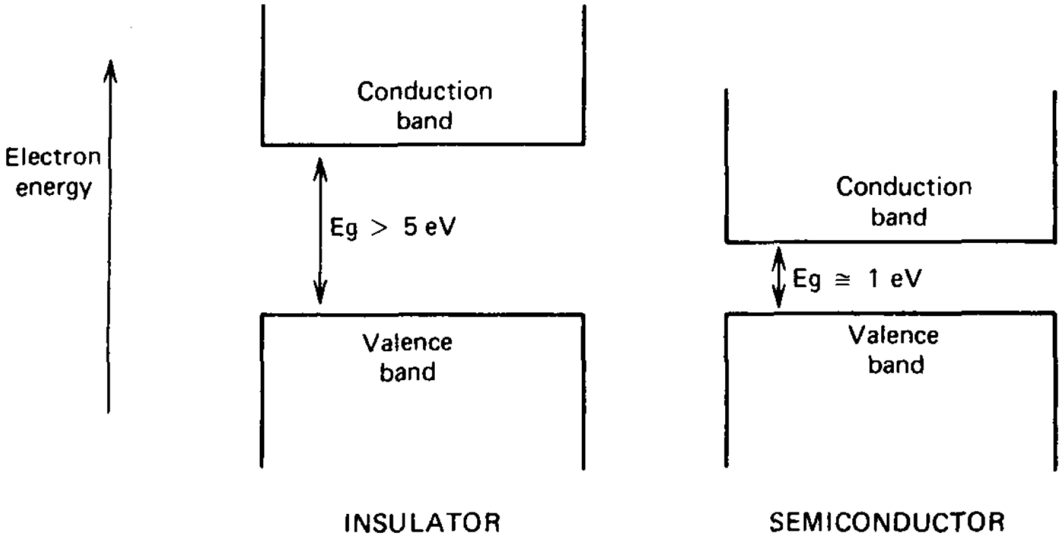

Figure 2.1: Simplified representation of the energy band structure for insulators and semiconductors [14].

2.3. The Mechanics and Migration of Charge Carriers

When an electron in the valence band gains sufficient energy through a gamma-ray interaction event, it is possible for that electron to be elevated across the band gap into the conduction band. This process results in the simultaneous addition of an electron in the conduction band and the creation of a vacancy (referred to as a *hole*) in the valence band [16]. These electron-hole pairs provide the fundamental mechanism that makes radiation detection in semiconductor detectors possible. Electrons within a semiconductor move along the conduction band when an electrical field is applied. The hole also moves, but in a direction that is opposite of the electron. It is this very motion of the electron and hole that contributes to the observed conductivity of the semiconductor. The probability per unit time that an electron-hole pair is thermally generated is governed by [14];

$$p(T) = CT^{\left(\frac{2}{3}\right)} exp\left(-\frac{E_g}{2kT}\right) \tag{2.1}$$

where T = absolute temperature

E_g = bandgap energy

k = the Boltmann constant, and

C = proportionality constant characteristic of the material

It can be readily observed from the above equation that the probability that an electron-hole pair is generated is dependent on the absolute temperature and the energy bandgap of the material. This equation also explains why materials with a large bandgap will have a low probability of thermal excitation. Conversely, materials with very small bandgap have a high propensity for thermal excitation and subsequently, electron-hole pair creation. If an electric field is applied, both the electrons and the holes will undergo a significant migration. This migration is parallel to the direction of the applied field. It is important to note that the migration of the hole is equally important as the migration of the electron. Electrons will always move in a direction opposite to the electric field vector whereas the hole will move in the same direction as the electric field.

The Shockley–Ramo theorem is frequently used calculate the instantaneous electric current induced by a charge moving in an electrode [17]. The Shockley–Ramo theorem states that the instantaneous current i induced on a given electrode due to the motion of a charge is given by [18]:

$$i = E_v q v \tag{2.2}$$

where q is the charge of the particle;

v is its instantaneous velocity; and

E_v is the component of the electric field in the direction of v

2.4. High Purity Germanium Gamma-Ray Detectors

A germanium detector element is simply a diode made by means of applying electrical contacts to a single crystal of germanium. In the case of research identified in this document, high-purity germanium was used. High-purity germanium is differentiated from traditional Ge(Li), that is germanium detectors produced by the lithium drifting process, by the level of purity achieved in the germanium.

The advantages identified in the use of semiconductor detectors for gamma-ray spectroscopy was that because of the relatively low band-gap energy, excellent energy resolution can be achieved. High purity germanium offers an additional performance advantage. High purity germanium has the ability to have much deeper depletion depth or active detector volume as compared to traditional silicon detectors. Traditional silicon detectors have depletion depth limitations on the order of 2 or 3 mm. This makes them unsuitable for gamma-ray spectroscopy where gamma-rays of high energies will penetrate more than the aforementioned 2 to 3 mm depletion depth [19]. Net impurity concentrations for HPGe can be as low as 10^{10} atoms/cm^3[14]. The thickness of the depletion region is governed by [20];

$$d = \left(\frac{2\epsilon V}{eN}\right)^{\frac{1}{2}} \tag{2.3}$$

where: V is the reverse bias voltage

N is the net impurity concentration in the bulk semiconductor material

$\in$ is the dielectric constant, and

e is the electronic charge

By simple inspection of equation 2.3, it can be observed that the depletion depth may be influenced by increasing the bias voltage, reducing the impurity concentration or a combination of the two. Subsequently, the performance of a detector depends on its depletion depth, which is inversely proportional to the net impurity concentration in the detector material. Achieving ultra-pure levels is only achieved by the use of advanced manufacturing techniques.

Table 2.2: General properties of germanium [14].

Property	**Germanium (Ge)**
Atomic Number	32
Atomic Weight	72.60
Stable Isotope Mass Numbers	70-72-73-74-76
Density (300 ºK); g/cm^3	5.32
Atoms/cm^3	4.41×10^{22}
Dielectric Constant (vacuum)	16
Forbidden energy gap (300 ºK); eV	0.665
Forbidden energy gap (0 ºK); eV	0.746
Intrinsic carrier density (300 ºK); cm^{-3}	2.4×10^{13}
Intrinsic resistivity (300 ºK); W · cm	47
Electron mobility (300 ºK); cm^2/V · s	3900
Hole mobility (300 ºK); cm^2/V · s	1900
Electron mobility (77 ºK); cm^2/V · s	3.6×10^4
Hole mobility (77 ºK); cm^2/V · s	4.2×10^4
Energy per electron-hole pair (300 ºK); eV	--
Energy per electron-hole pair (77 ºK); eV	2.96

The process by which high purity germanium is manufactured is complex in nature, including many critical steps. This complexity is one of the primary reasons why there are very few companies in the world today that produce high volumes of HPGe and distribute it on a commercial basis. The steps by which polycrystalline germanium is manufactured into a gamma-ray detector are shown in figure 2.2.

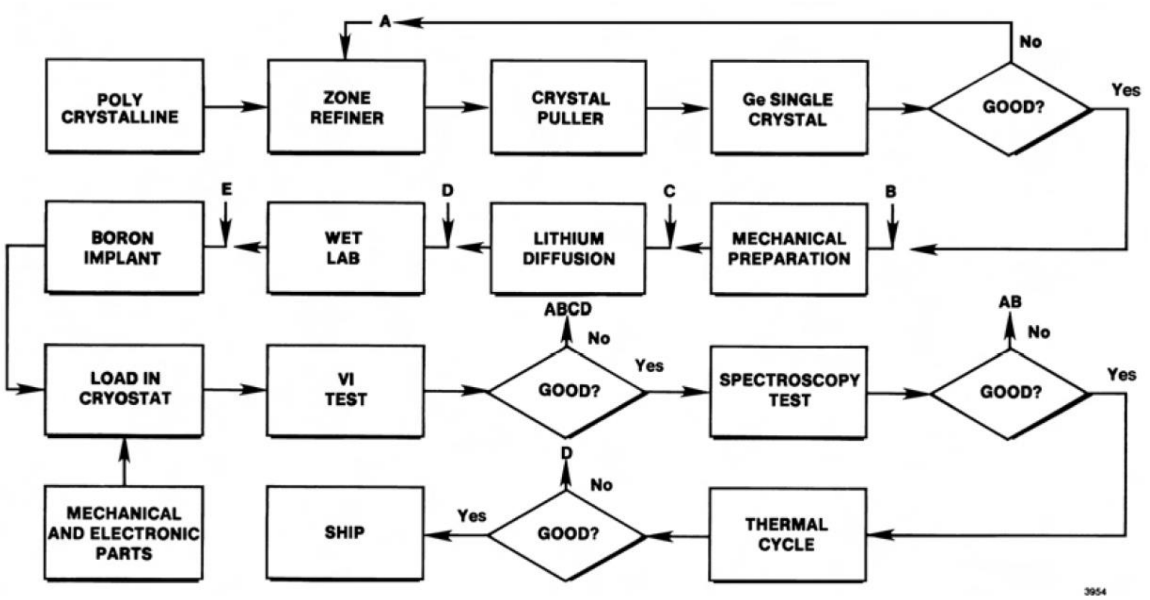

Figure 2.2: Flow chart of typical high purity germanium detector manufacturing process [21].

The process starts with electronic grade polycrystalline germanium metal which is refined in a quartz vessel to levels of impurity as low as 10^{10} atoms/cm^3 [22]. The ultra-purity of high purity germanium is achieved through additional refinement from what is already considered high levels of purity within the semiconductor industry. This refinement is achieved through a process called zone refining. In the zone refining process, the impurity levels are progressively reduced by locally heating the germanium and passing a melted zone from one end of the sample to the other. This is achieved by moving RF heating coils slowly along the length of the germanium ingot. This is based on the principle that most material impurities concentrate in the liquid phase as the material begins to freeze. As the RF heating coil translates along the length of the germanium ingot, it creates a liquefied portion of germanium beneath it. As the liquid portion of the germanium moves in conjunction with the coil, subsequently the impurities move also. This ‘sweeping’ operation of the RF coil is repeated many times until the impurities have been concentrated to one end of the ingot. This ‘impure’ end is then removed. The remaining portion of the germanium is then evaluated for impurity concentrations determined by the Hall Effect measurement. The Hall Effect is based on the theory that the conductivity (σ) of the germanium material is given by;

$$\sigma = \frac{1}{\rho} = \frac{l}{A}\frac{I}{V} \qquad (2.4)$$

where: ρ is the resistivity

l is the length of the sample

A is the cross sectional area

I is the applied current, and

V is the voltage

The principle behind the Hall Effect is that the voltage of the semiconductor sample is measured as a function of the doping in the crystal, the temperature and magnetic field. The results obtained can then be used to determine the associated energy gap, conductivity, type of charge carrier, and carrier concentration. Due to its relevance and importance to the discussion of high purity germanium detectors, further theory surrounding the Hall Effect and its use in the manufacturing process will be reviewed next.

The conductivity of any semiconductor is a function of temperature. In this range, charge carriers are activated as the temperature rises. This activation continues until all carriers from impurities have been activated. At moderate temperatures, depletion occurs. This impurity depletion that occurs is a result of all impurities being activated meaning that further increases in temperature do not result in further impurity generated carriers. Further increase in temperature results in what is referred to as intrinsic conduction. In this region, additional charge carriers are created by thermal excitation from the valence band to the conduction band, as discussed previously. In this region, the dependence of the conductivity (σ) on temperature can be described by

$$\sigma = \sigma_0 \left(-\frac{E_g}{2kT} \right) \tag{2.5}$$

where: E_g is the energy gap

k is Boltzmann’s constant and,

T is absolute temperature

Once that evaluation has been successfully completed, suitable sections of germanium are selected and loaded into the crystal growing equipment. The refined germanium is then used in conjunction with the Czochralski technique to ‘grow’ the crystal that will ultimately be used for the detector itself.

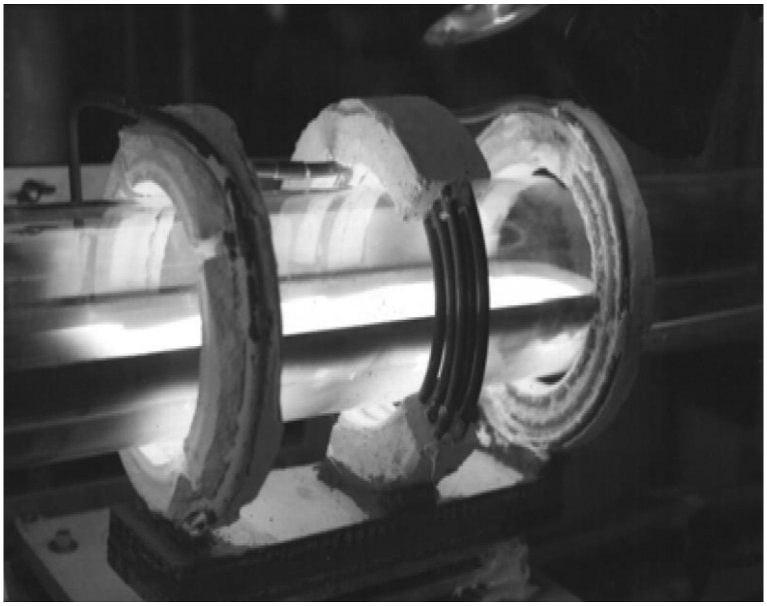

Figure 2.3: Three coil zone refiner [21].

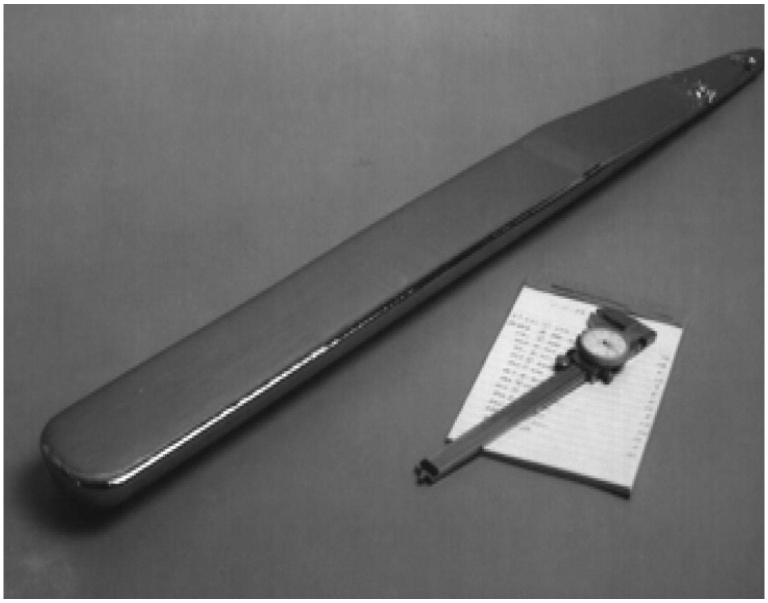

Figure 2.4: Refined germanium 'boat' [21].

In the Czochralski technique, a precisely cut seed crystal is dipped into the molten germanium and then withdrawn slowly, while maintaining the temperature of the melt just above the freezing point [23]. The rate of crystal withdrawal and temperature of the melt are adjusted to control the growth of the crystal. High-purity germanium crystals used for gamma-ray detectors are typically grown in a quartz crucible under a hydrogen atmosphere. Near the completion of the growth process, the crystal is tapered gradually at the tail to minimize thermal strain. It is critical that the crystal is grown to the exhaustion of the melt. This is due to the fact that molten germanium 'wets' the quartz and expands on freezing. This resulting freezing can lead to damage to the crucible if melt is left after the completion of the crystal growth.

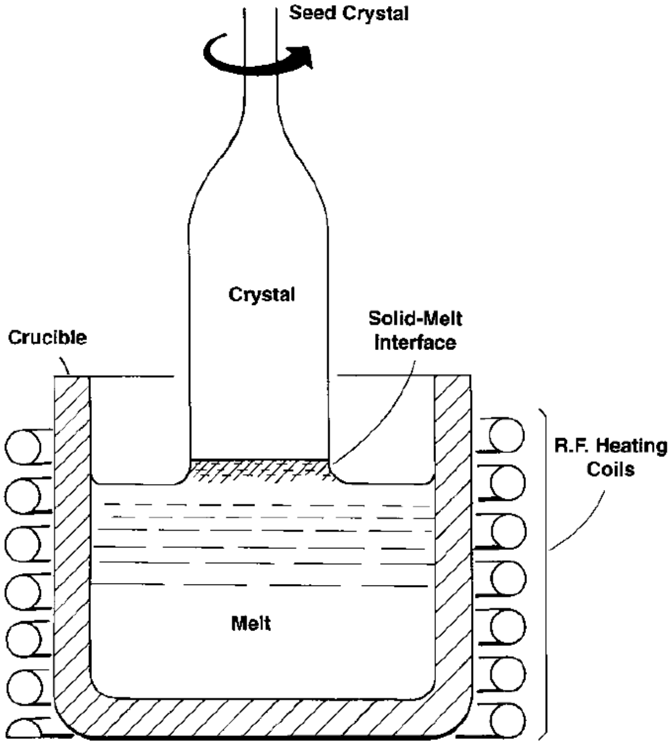

Figure 2.5: Detailed schematic of the Czochralski technique used for the growth of high purity germanium crystals [21].

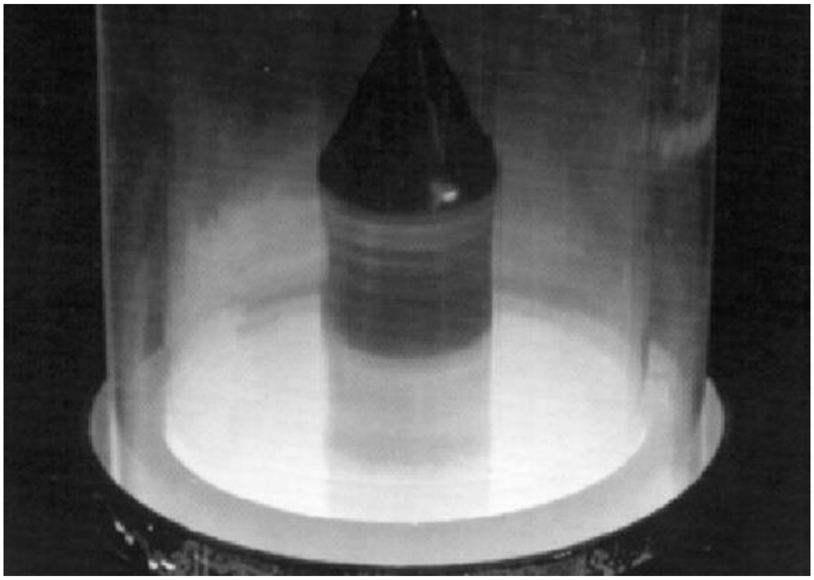

Figure 2.6: High purity germanium crystal growth using the Czochralski technique [21].

Figure 2.7: Germanium crystal being sliced [21].

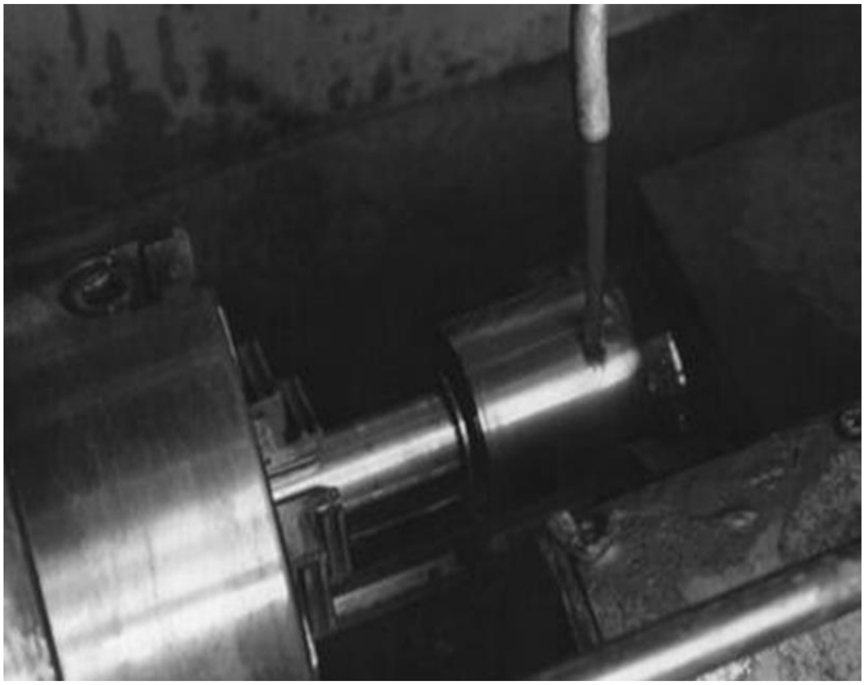

Figure 2.8: Germanium crystal being ground [21].

Once the germanium crystal has been successfully grown, it is removed from the puller and mounted in a cast for the slicing process. This step is shown in figure 2.7. The Hall Effect measurement is once again used to determine the impurity concentration and whether the detector is of p-type or n-type material. The type of the detector (p-type or n-type) is determined by the impurities present in the crystal. If the remaining low-level impurities are acceptors, the electrical properties of the crystal are mildly p-type. Alternately, if donor impurities remain, the resulting material is high purity n-type. As a point of reference, the designation π-type is often used to represent high purity p-type material while high purity n-type material is often designated as ν-type. The electrical conductivity of the high purity germanium crystal as a function of dopant concentration can be seen in Figure 2.9.

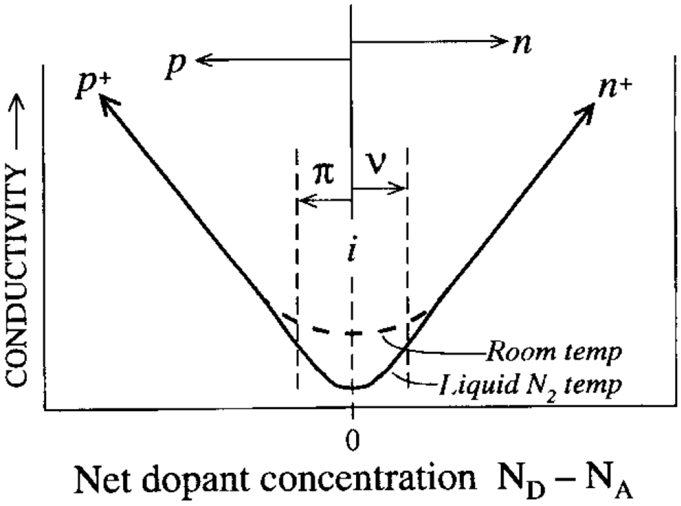

Figure 2.9: Electrical conductivity in high purity germanium as a function of net dopant concentration [14].

After the purity and crystallographic review has been completed, suitable germanium is selected for detector fabrication. In this stage of the process, the germanium crystal is machined into the final detector geometry. The geometry is dependent on the type of the desired detector (e.g. planar, coaxial, etc.). Contacts are then diffused on the detector using various materials. Detector geometry and diffusion techniques will be discussed further in subsequent chapters.

2.5. Gamma-Ray Spectroscopy with High Purity Germanium Detectors

High purity germanium is consistently the detector of choice when conducting gamma-ray spectroscopy due to the excellent energy resolution that it provides. In addition, due to the low impurity levels achieved through the purification process (refining), high purity germanium is capable of achieving relatively thick depletion regions. Chapter 2.5.1 will review different detector configurations used in gamma-ray spectroscopy.

2.5.1. Coaxial Detector Configurations

This research focused primarily on coaxial detector configurations. The coaxial configuration derives its name due to the cylindrical or *coaxial* nature of the detector itself. There are three primary types of coaxial detectors that will be discussed at this time. These three types of coaxial detectors are; true coaxial, closed-ended coaxial, and close-ended (bulletized) coaxial. The contacts are placed on the detector by two primary methods. These methods include a process of diffusion in which a contact material such as lithium is diffused onto the surface of the detector or by means of ion implantation on the surface via an accelerator. The most common approach used in p-type high purity germanium detectors is the lithium diffusion process.

The coaxial configuration is capable of achieving much larger active volumes than planar configurations due to the fact that the germanium crystals are ‘grown’ in the axial direction [14]. This means that detectors can be made relatively long in the axial direction. It is worth noting that another advantage of the coaxial configuration is that much lower capacitances are able to be achieved as compared to planar detectors. Lower capacitances within the detector provide improved noise conditions. This is made possible by making the inner diameter small so that the area of the central contact is relatively small. The capacitance per unit length of a fully depleted true coaxial detector is given by [20];

$$C = \frac{2\pi\epsilon}{\ln(r_2/r_1)} \tag{2.6}$$

where: C is capacitance per unit length

r_1 is the radius of the central hole

r_2 is the outer radius of the detector, and

$\in$ is the dielectric constant

The most common type of commercially produced coaxial detector is the closed-ended coaxial (bulletized) configuration. In this configuration, only one end of the detector is machined. In order to avoid the complications associated with leakage current at the front face, which is often observed in the true coaxial configuration. Finally, the 'bulletizing' or rounding of the corners at the front of the detectors is done to reduce the low electric field regions. Figure 2.10 shows commonly used coaxial configurations. All coaxial configuration identified are produced by fabricating one electrode into the outer cylindrical surface of the detector and one additional electrode along the inner cylindrical surface. For the case of the coaxial configuration, the rectifying contact that creates the semiconductor junction can be located at either the outer surface or inner surface of the detector. There are advantages of locating this surface at the outer diameter of the detector. In the case of the rectifying contact being located at the outer surface of the detector, the depletion region grows inward as the voltage is increased. This depletion continues as the voltage is increased. The voltage observed at the point where the depletion region reaches the inner diameter of the detector is considered the depletion voltage. Conversely, if the rectifying contact is located at the inner diameter of the detector, the depletion layer grows outward as the voltage is increased. In order for the detector to become fully depleted (when the depletion region reaches the outer diameter of the detector) much larger voltages are required. It is primarily for this reason, coupled with the fact that having the rectifying surface at the outer diameter of the detector results in larger electrics fields in larger portions of the active volume that the desired configuration is to have the rectifying surface at the outer diameter of the detector. This is true in either case whether the detector is of the p-type or n-type variety as shown in

Figure 2.11 where it can be seen that the outer contact for a p-type high purity germanium coaxial detector will be n^+. The outer contact for an n-type high purity germanium coaxial detector will be p^+. In either case, the diameter surface is of the opposite type.

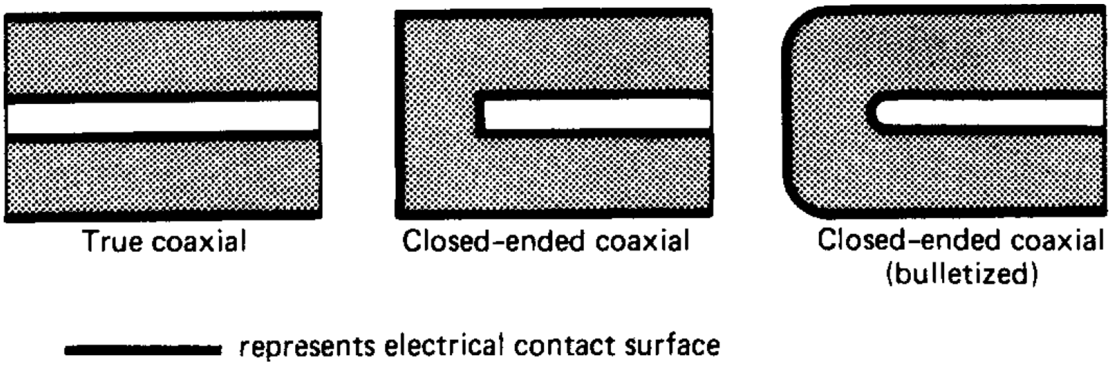

Figure 2.10: Tradition configurations used in coaxial detectors [14].

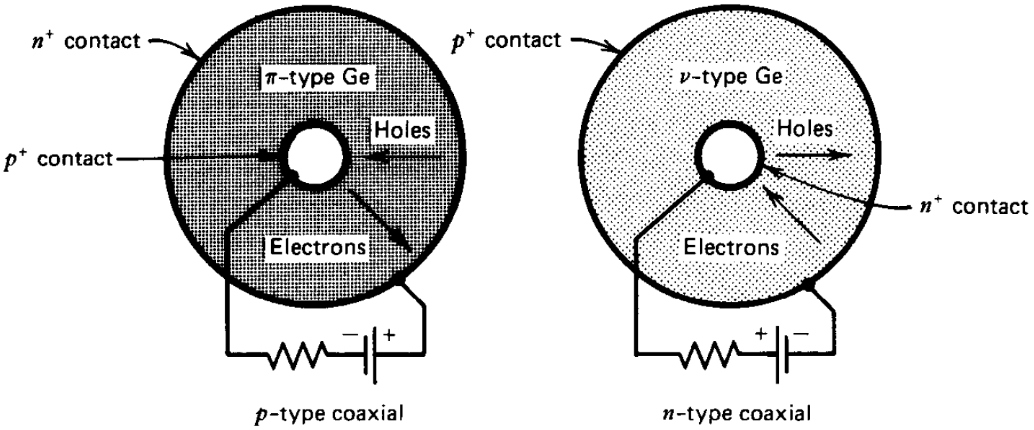

Figure 2.11: Cross section representations and associated contacts for p-type and n-type coaxial detector configurations [14].

2.6. Detector Properties and Operational Characteristics

In the case of gamma-ray spectroscopy, there are a number of detector properties and operational characteristics that are of primary concern. This chapter will specifically focus on these desired characteristics. In particular, five fundamental characteristics will be reviewed in detail. These six operational characteristics are energy resolution, detector noise contributions, charge trapping effects, rise time, and entrance window layer (dead layer). Energy resolution and the effects that contribute to its degradation will be given additional focus due to its relative importance to the measurements taken as a part of this research. In addition, energy resolution is the primary determining factor of the identification efficacy of any radioisotope identification device.

2.6.1. Energy Resolution

Energy resolution in its most basic form can be defined as the full width at half maximum (FWHM) divided by the peak centroid as shown in figure 2.12 [24].

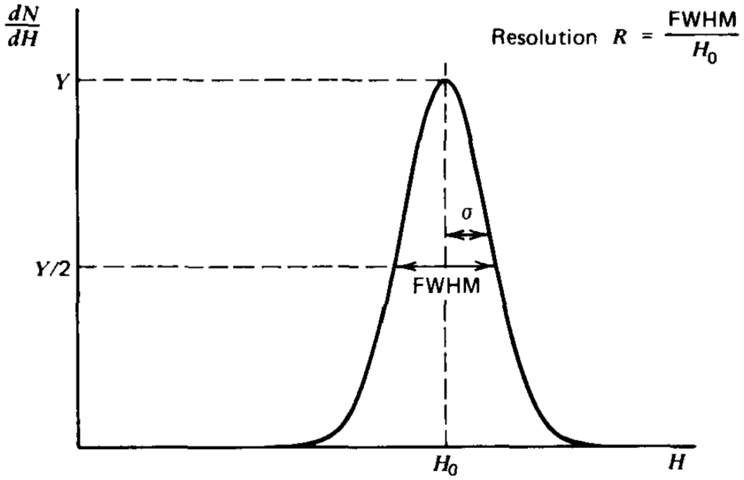

Figure 2.12: Formal definition of detector energy resolution [12].

The use of the term energy resolution typically refers to the total or overall energy resolution of a particular system. This overall energy resolution is determined by a combination of three factors: the inherent statistical spread in the number of charge carriers, variations in the charge collection efficiency, and contributions of electrical noise. The relative contribution of each of these three factors depends heavily on the size and quality of the detectors used. In general, the total energy resolution (FWHM), W_T is given by

$$W_T^2 = W_D^2 + W_X^2 + W_{EM}^2 \qquad (2.7)$$

where W_D^2 = energy resolution contribution from inherent statistical fluctuation in the number of charge carriers created

W_X^2 = represents the incomplete charge collection and is most significant in detectors of large volume, and

W_{EM}^2 = represents the broadening effects of all electrical and mechanical noise components.

When considering the statistical fluctuation in the number of charge carriers, the Fano factor quantifies the departure of the observed statistical fluctuations in the total number of charge carriers from pure Poisson statistics and is defined as [29];

$$F \equiv \frac{observed\ variance\ in\ N}{Poisson\ predicted\ variance\ (=N)} \qquad (2.8)$$

where N is the total number of charge carriers. This results in a statistical limit that is governed by the following [29];

$$R|_{Statistical\ limit} = \frac{2.35K\sqrt{N}\sqrt{F}}{KN} = 2.35\sqrt{\frac{F}{N}} \qquad (2.9)$$

where K is the proportionality constant.

Although the resolution performance variations exist between detectors of different types/material, it is important to note that detector noise originates from multiple sources. These noise contributions in spectroscopic measurements are series and parallel noise. This includes variations in the bulk generated leakage current (parallel), variations in the surface leakage (parallel), resistance noise and mechanically induced noise (series).

In homeland security and first responder applications, there is a benefit in being able to measure the energy distribution of the incident radiation; including specific identification of the radiation. This concept of measuring the energy distribution of the incident radiation is known as gamma spectroscopy. Previous references were made to the performance benefits of semiconductor detectors, specifically high purity germanium detectors in regard to the excellent energy resolution that they provide the user. This means that the energy distribution is relatively small. This concept can be observed in figure 2.13. The two curves; one labeled good resolution and the other labeled poor resolution. The width of each curve represents the pulse height fluctuation observed in the detector despite the same total energy being deposited in the detector. As the energy fluctuations are reduced, so also is the width of the peak. Legitimate commerce typically has large quantities of naturally occurring radioactive material (NORM) [25]. This includes items such as ceramic tiles, fertilizer, and medical isotopes. If the specific energy of the incident radiation is known, however, the radioisotope can be identified. Further, the radioisotope can be identified as a threat or non-threat material. Figure 2.14

offers a general comparison of relative energy resolution performance of NaI and HPGe. The use of the term energy resolution typically refers to the total or overall energy resolution of a particular system

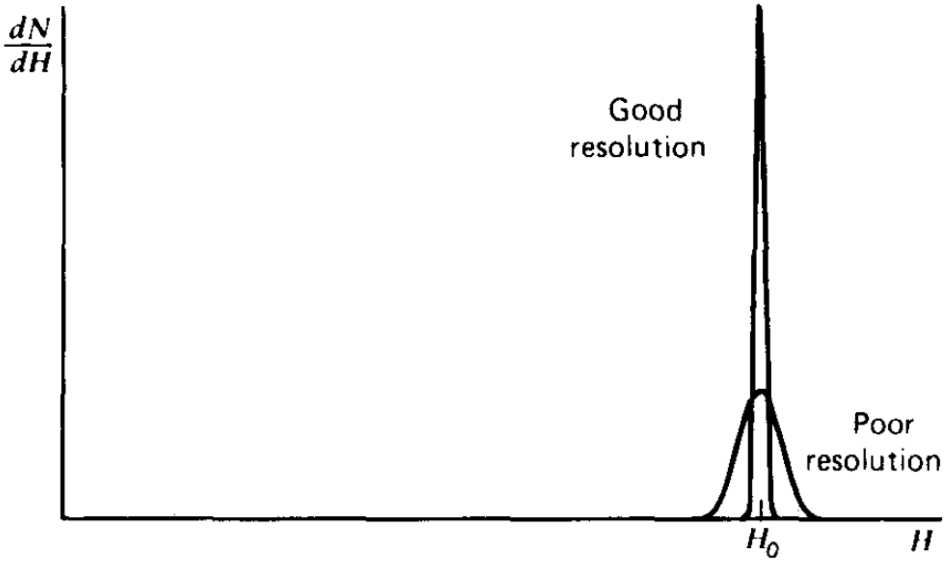

Figure 2.13: General comparison between good and poor energy resolution [14].

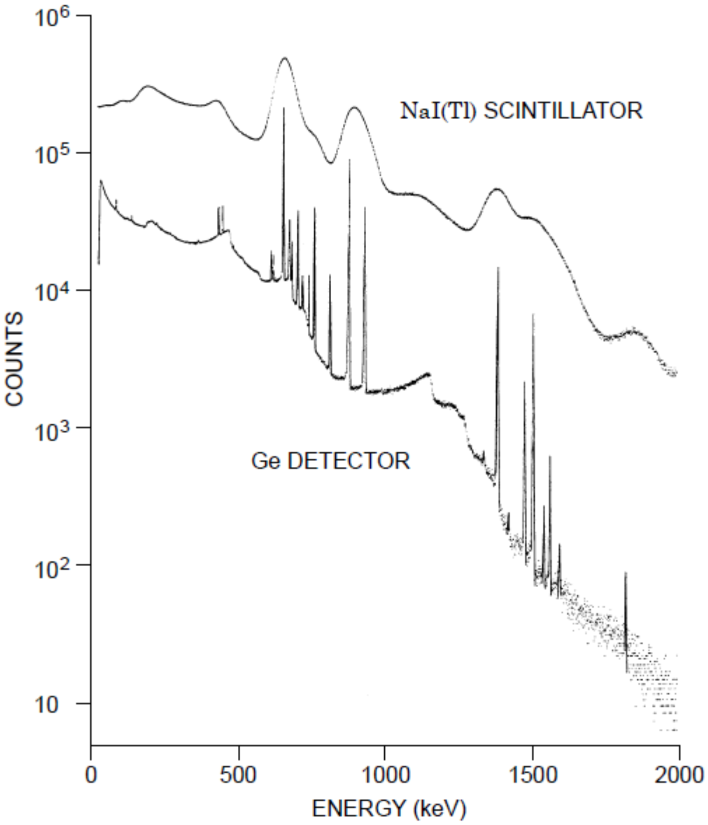

Figure 2.14: Relative energy resolution performance of NaI (scintillator), and HPGe (semiconductor) [26].

2.6.2. Detector Noise Contributions

The basic limitations on operating liquid nitrogen cooled high purity germanium detectors at elevated temperatures are due to increased trapping effects and increased electronic noise [27]. Section 2.6.2 will focus on the sources of noise degradation and Section 2.6.3 will focus on charge trapping effects.

When considering traditional HPGe semiconductor detectors there are three categories of noise sources: the thermal noise of the parallel resistance, the thermal noise of the series resistance, and the noise due to the leakage current of the detector [28]. The term traditional HPGe semiconductor detector is used with reference to LN_2 cooled detectors. One additional category of noise contribution introduces itself with the addition of mechanical cooling: microphonic related noise from the cryocooler. The parallel noise component is made up of two basic components: the bias noise current source and the detector capacitance [29]. The free electrons in an electrical conductor are in a constant state of thermal agitation. Small current fluctuations correspond to this constant motion of charges, which in turn give rise to voltage fluctuations at the ends of the conductor [28]. This small current due to the noise voltage from the parallel resistance can only flow through the detector capacitance. This noise voltage is characterized by

$$v^2 = 4kT_eR\Delta f \qquad (2.10)$$

where: k is the Boltzmann constant,

f is the frequency,

T_e is the absolute temperature, and

R is the resistance of the conductor in ohms.

The capacitance needs also to be accounted for. This results in;

$$\frac{v^2}{\Delta f} = \frac{4kT_eR}{1+(\omega R\Sigma C)^2} \qquad (2.11)$$

If integrated over the entire range of frequencies, equation 1.10 can be reduced to

$$v^2 = \frac{kT_e}{\Sigma C} \tag{2.12}$$

This is commonly referred to as 'KTC' noise [29]. One point of note concerning equation 2.9 is its independence on the parallel resistance. This is due to the fact that as this resistance increases (and subsequently the thermal noise increases) the noise bandwidth decreases. This results in the independence of the parallel resistance. The noise voltage associated with the series resistance is [29]

$$v^2 = 4kT_eR_s \tag{2.13}$$

A germanium detector spectrometer system, specifically, is limited by the following sources of noise: preamplifier input noise, detector contact noise, charge generation statistics, internal generated detector noise, and signal variations due to temperature fluctuations [27]. Preamplifier noise is a function of the input electronics, and the load capacitance is independent of temperature [27]. Detector contact noise and charge generation statistics are expected to not vary significantly with temperature. These leaves internally generated detector noise and the most temperature sensitive component. The primary cause of the internally generated noise is the detector leakage current.

The detector depletion region in a semiconductor detector is developed by reverse biasing the PN junction of the detector. When this reverse biasing occurs, a small current, typically on the order of a microampere is observed. This is referred to as leakage current. This leakage current is related to the bulk volume and the surface of the detector. Bulk leakage currents are referred to as 'bulk' because they originate internally within the volume of the detector. The following sources of current in a PN junction must be considered: diffusion current, injected currents, photon generated currents, breakdown currents, and thermally generated currents within the depletion regions. Each of these sources will be described in further detail at this time.

The *diffusion current* is a source of current due to the diffusion of minority carriers into the depletion region from the P and N contacts. The general expression for the magnitude of this current is [27]

$$I_{diff} = A\left[\left(\frac{D_p}{\tau_p}\right)^{\frac{1}{2}} P_{n_o} + \left(\frac{D_n}{\tau_n}\right)^{\frac{1}{2}} n_{p_o}\right] \tag{2.14}$$

where A is the junction area, D is the diffusion constant, τ is the carrier lifetime and p_{n_o} and n_{p_o} are the minority carrier concentrations.

The *injected currents* result from injecting currents on the P or N junction. These currents inject minority carriers through the junction region in a manner similar to transistor action [27]. *Photon generated currents* are due to free carrier production introduced by electromagnetic radiation. *Breakdown currents* can be either surface or bulk in origin. These currents usually result from large electric fields that cause avalanche breakdown. Avalanche breakdown is a phenomenon that can occur in both insulating and semiconducting materials. Avalanche breakdown is a form of electric current multiplication that can allow very large currents within materials. The avalanche process occurs when the carriers in the transition region are accelerated by the electric field to energies sufficient to free electron-hole pairs via collisions with bound electrons [30]. These currents dominate in limiting the maximum operating bias of a germanium detector at low temperatures [27]. *Thermally generated currents* within the depletion region are caused by thermal ionization of the electron-hole pairs within the volume of the detectors. This occurs either through direct transition (band-to-band) or through traps (trap-generated) [27].

The total current within the detector as a function of bias voltage and temperature can be represented by the following equation.

$$I(V,T) = I_o + I_1 \exp\left(-\frac{E_g}{kT}\right) + I_2 V^{\gamma} + I_3 V^{\frac{1}{2}} \exp\left(-\frac{E_g}{kT}\right) + I_4 V^{\frac{1}{2}} \exp\left(-\frac{E_t}{kT}\right)$$

(2.15)

where I_o = photo-excited + injected currents

$I_1 \exp\left(-\frac{E_g}{kT}\right)$ = temperature dependent diffusion currents

$I_2 V^{\gamma}$ = bias dependent breakdown current

$I_3 V^{\frac{1}{2}} \exp\left(-\frac{E_g}{kT}\right)$ = temperature dependent band-to-band generated current.

$I_4 V^{\frac{1}{2}} \exp\left(-\frac{E_t}{kT}\right)$ = temperature dependent trap-generated bulk current.

The temperature dependent terms generally are the limiting contributors to elevated temperature operation. It is worth noting, however, that a possible exception to this is the break-down current [27]. In the case of high purity germanium detectors, the junctions are typically heavily doped and normally fully depleted. This results in the diffusion current term being negligible. This leaves the band-to-band generated current and the trap-generated bulk current as the primary limiters in elevated temperature operation.

However, since high purity germanium is an indirect band gap semiconductor [31], simultaneous phonon transfer is required [27]. Further, indirect bandgap semiconductor detectors are not efficient light emitters because a phonon with a high momentum is required to transfer an electron from the conduction band to the valence band [32]. This decreases the probability of occurrence, reducing the overall impact on this current component. This leaves the final term, temperature dependent trap-generated bulk current as the dominant current at elevated temperatures; it is of primary interest in this study.

The trap-generated current flow involves the transition rate of electrons into and out of trap levels in the forbidden bandgap [27]. In semiconductors, the forbidden band separating the valence band and the conduction band is usually considered. In this case, the energy difference between the lower level (bottom) of the conduction band and the upper level (ceiling) of the valence band is called the width of the forbidden band [33]. A generalized expression that can be used to characterize the current due to a single trap is [34],

$$I = \frac{2V\sigma_n\sigma_p v_{th} N_t (N_c N_v)^{\frac{1}{2}}}{\sigma_n \exp\left[\frac{E_t-E_v}{kT}\right]+\sigma_p \exp\left[\frac{E_c-E_t}{kT}\right]} \tag{2.16}$$

where: V = depletion region volume

σ_n, σ_p = carrier capture cross sections

v_{th} = carrier thermal velocity

N_t = trap density

N_c, N_v = band effective density

$E_t - E_v$ = trap separation from valence band, and

$E_c - E_t$ = trap separation from conduction band

This bulk-generated type of current flow dominates the limitations to operating high purity germanium detectors at elevated temperatures.

An additional category of leakage currents occurs as a result of surface leakage effects. These leakage currents take place at the edges of the junction where large voltage gradients exist. The amount of surface leakage observed can vary greatly dependent on the integrity of the vacuum and any contamination that may exist on the detector face itself. In this regard, cleanliness and reducing any introductions of contaminations in the process are critical. Both bulk and surface leakage currents directly affect the energy resolution of the detector.

In addition to the degrading effects to energy resolution, leakage currents also introduce an additional challenges related to bias voltage in the detector. Consider figure 2.15. Figure 2.15a shows what is referred to as an ac-coupled detector configuration. In the ac-coupled configuration, a coupling capacitor is placed between the detector and the preamplifier circuit. This offers the distinct advantage of being able to adjust the values of R_L independent of the preamplifier input. Figure 2.15b shows a dc-coupled configuration. In the dc-coupled configuration, the coupling capacitor is removed which typically leads to better noise performance. In this configuration, the detector must be isolated from ground and changing the bias resistor may affect the input stage characteristics. When the preamplifier is dc-coupled to the detector, any leakage current that originates in the detector must be accounted for by the preamp [14]. For this reason, ac-coupling should be considered in situations where high leakage current is observed or anticipated. In the ac-coupled configuration, the leakage current from the detector is blocked by the coupling capacitor. The observed bias voltage applied to the detector is reduced by the product of the leakage current and the series resistance. If the leakage current becomes sufficiently large, the voltage drop across the resistor can result in a drop in actual bias voltage seen by the detector.

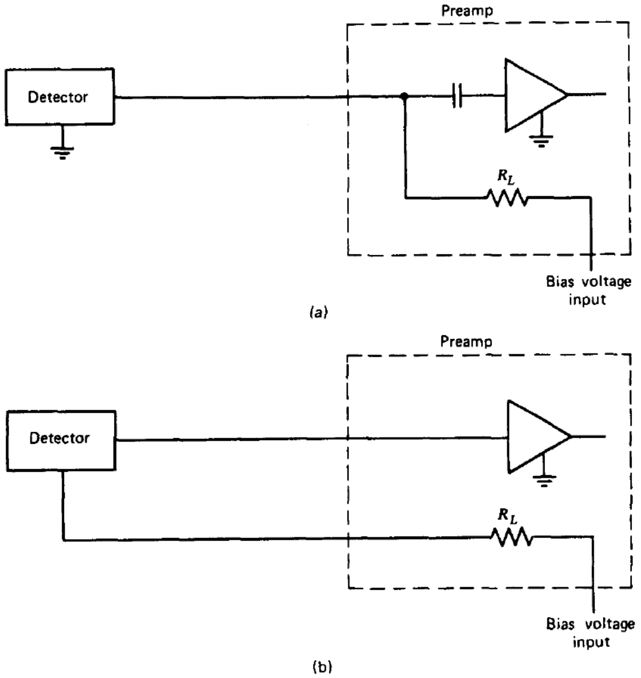

Figure 2.15: Two commonly used configurations used to supply detector bias through a preamplifier [14].

2.6.3. Charge Trapping Effects

In chapter 2.6.2, trap-generated current flow was identified as a significant contributor to noise degradation in a detector. Charge trapping itself also contributes to spectrum degradation at lower temperatures [27]. This associated spectrum degradation occurs as a result of charge loss in deep level traps [35]. Further, there are two components contributing to the associated spectrum loss; geometrical and statistics variations.

The charge loss due to charge trapping is on the order of $n_o \left(\frac{t_c}{\tau}\right)$;

where: n_o = the original signal

t_c = the charge collection time, and

τ = the mean time before trapping

In high purity germanium detectors, biasing is such that the charge collection velocities are approaching saturation (~10^7 centimeters per second) [36]. This effectively means that the charge collection times are on the order of 10^{-7}d where d is the depletion depth in centimeters. As the temperature is increased, carrier mobility decreases as a result of increased lattice scattering effects [37]. This creates challenges to obtaining additional and adequate electrical fields resulting in a decrease in the overall collection velocity [38]. For example, at 300°K t_c is reduced to approximately 10^{-6} d which causes a significant increase in the trapping induced charge loss [39] and an associated decreasing detector performance. Shaping time adjustment does present an effective means of compensating for trapping induced charge loss.

In order for the trapping to have negative consequence on the performance of the detector, the charge must remain trapped for a time period longer than the shaping time constant of the amplifier [40][41]. Alternatively stated, if the escape is shorter than that of the shaping time constant, the charge trapping does not significantly contribute to the worsening of the detector performance. Accordingly, the mean escape time from a trap can be approximated by [27].

$$\tau = \frac{1}{\sigma v_{th} N * exp\left(-\frac{|E_t - E_b|}{kT}\right)} \tag{2.17}$$

where

v_{th} = carrier thermal velocity (~10^7 cm/sec)

N = effective density of state of either the valence or the conduction band, and

$|E_t - E_b|$ = trap energy difference from either the valence or conduction band edge

2.7. Prior Research

Setting aside mechanical cooling, the currently available research appears to be limited to detector volumes up to 80 cm^3. Four specific research studies will be highlighted at this time. These particular studies have been selected for thorough review because of their specific relevance to this research;

- G. H. Nakano, W. L. Imhof, IEEE Trans. *Nucl. Sci.*, NS-18, No. 1, 258 (1971).
- G.A. Armantrout, *IEEE Trans. Nucl. Sci*., NS-19, No. 3, 289 (1972).
- R. Pehl, E. Haller and R. Cordi, *IEEE Trans. Nucl. Sci*., NS-20, No. 1, 494 (1973).
- G.H. Nakano, D.A. Simpson, and W.L. Imhof, *IEEE Trans. Nucl. Sci.* NS-24(1), 68 (1977).

The results and significant relevance of each research study will be reviewed as a part of this chapter.

2.7.1. Nakano and Imhof Study

In this study, Nakano and Imhof undertook a measurement program to investigate design criteria for satellite-borne Ge(Li) detector systems [42]. Through their research the knee (point where rapid changes occur) in the energy resolution versus temperature was determined for three Ge(Li) detectors. At the time this publication was written, very little data had been reported concerning the temperature dependence of ‘large’ (>25 cubic centimeter) detectors, particularly at temperatures above 77°K.

For this research, three commercially available detectors were used with properties shown in table 2.3. Each of the three detectors used for this research were mounted in a standard right-angle dipstick. A simple example of a right-angle dipstick can be seen in figure 2.16.

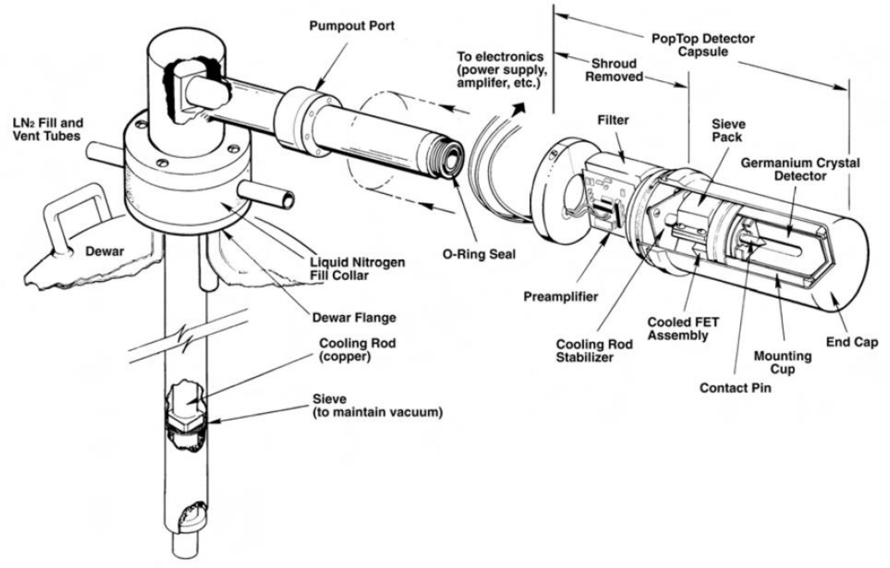

Figure 2.16: Exploded view of a right-angle dipstick configuration used in conjunction with a liquid nitrogen dewer [43].

The temperature of each of the detectors was measured using thermocouples embedded into the copper cold finger of each assembly. A heater was used as a means of controlling the temperature of the detector. Each detector was studied through a range of temperatures between 22ºK and 160ºK. Key observations include.

a. With lower bias voltages, even poorer quality detectors can be made to operate with broader but reasonable resolution [42]. This is due to the fact that leakage current is a function of bias voltage. This will be discussed in further detail in this chapter.

b. This research was able to demonstrate the feasibility of operating a large Ge(Li) detector with good resolution at temperature up to 130ºK to 140ºK.

The first of these two points is observed in figure 2.17. For each respective detector, the leakage current is observed to increase with temperature at a given bias voltage [44]. Another observation that should be made is that the leakage current increases with increased bias voltage. This is consistent with the temperature dependent leakage current components discussed in chapter 2.6.2. The practical implication of this is that a detector should be operated at only the bias necessary to achieve full depletion as a means of reducing the overall leakage current. This leakage current versus bias voltage relationship translates into reduced overall energy resolution performance with temperature as seen in figure 2.17. As the bias voltage is increased, the energy resolution is degraded. This is due to specifically to the relationship observed in figure 2.17: leakage current increases with increasing bias voltage.

Table 2.3: Detector properties for the three detectors used for the evaluation of energy resolution as a function of temperature in the Nakano, Imhof study of 1971 [42].

Parameter	Ge(Li) Serial Number		
	483A	519	575
Type:	Single-Ended	Single-Ended	Single-Ended
Diameter	39.0 mm	40.5 mm	39.0 mm
Length	22.0 mm	25.0 mm	21.8 mm
Drift Depth	17.0 mm	16.5 mm	14.75 mm
Efficiency	4.2%	4.8%	4.5%
Capacitance	20 pf	22 pf	17 pf
Resolution (1.33 MeV) FWHM	2.25 keV	2.61 keV	2.37 keV
Resolution (1.33 MeV) FWTM	4.50 keV	4.95 keV	4.50 keV
Peak / Compton	20:1	20:1	22.6:1

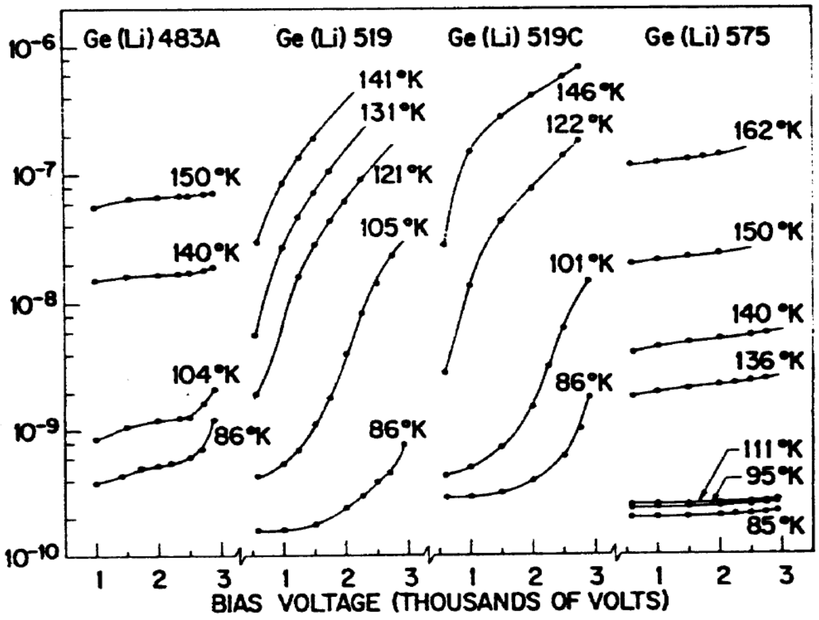

Figure 2.17: Leakage current versus bias voltage [42].

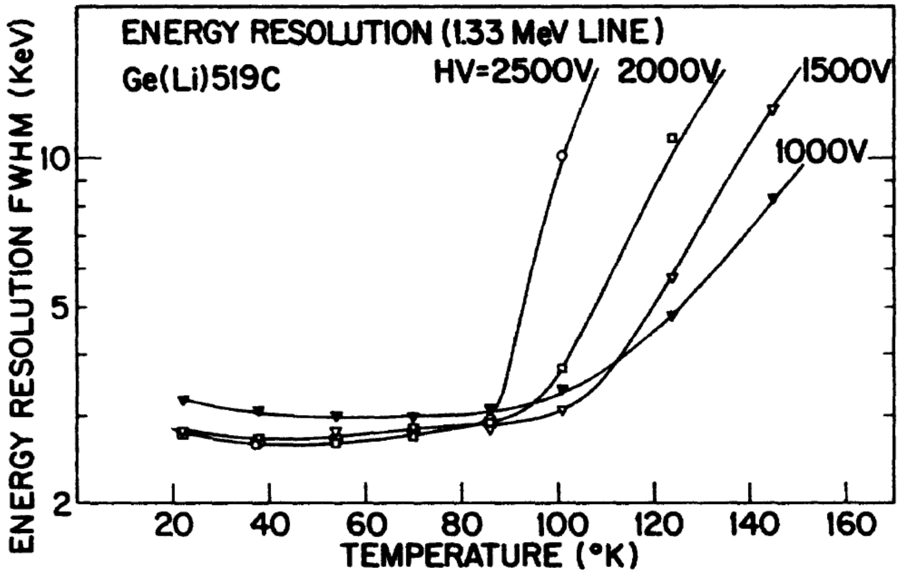

Figure 2.18: Observed energy resolution at the 1.33 MeV Co-60 gamma-ray line as a function of temperature for various applied bias voltages [42].

2.7.2. Armantrout Study

Guy Armantrout's 1972 publication provided an extensive analysis of noise contribution in germanium detectors as a function of temperature and provided substantiating measurements. Specifically, Armantrout focused on measuring and quantifying the various components of the total noise contribution. This research used high purity germanium detectors for most of the data collected. Although a number of observations were made, one significant observation was the bulk generated leakage current as a function of volume. Armantrout was able to show (figure 2.19) that at lower temperatures the bulk generated current appears to be dominated by trap-generated current likely due to excitation through crystal defects. At higher temperatures, the slope is much different and is more likely dominated by band-to-band excitation [27]. In each case, the leakage current increases with increasing volume. This observation is of particular significance and will be an integral part of the analysis section detailed in chapter 6. Further, Armantrout was also able to show volume generated current as a function of temperature as shown in figure 2.20. The significance of this observation is that the volume-generated current is significantly higher than the band-to-band generated current at all temperatures. At lower temperatures the current is exclusively trap generated. Armantrout notes that at a temperature of 200ºK this current is more than 100 nA/cm^3; more than two orders of magnitude greater than the band-to-band generated current [27]. One final observation from Armantrout is the electrical noise as a function of leakage current shown in figure 2.21. It is observed that as the leakage current of the detector at a given bias and temperature increases, the electric noise contribution to the detector also increases in a linear fashion.

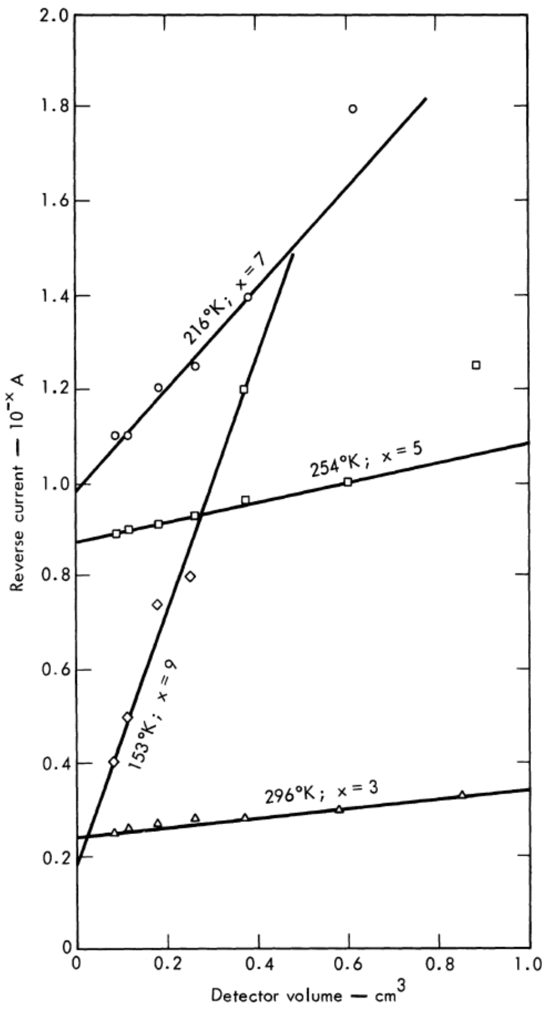

Figure 2.19: Leakage current versus volume as a function of temperature [27].

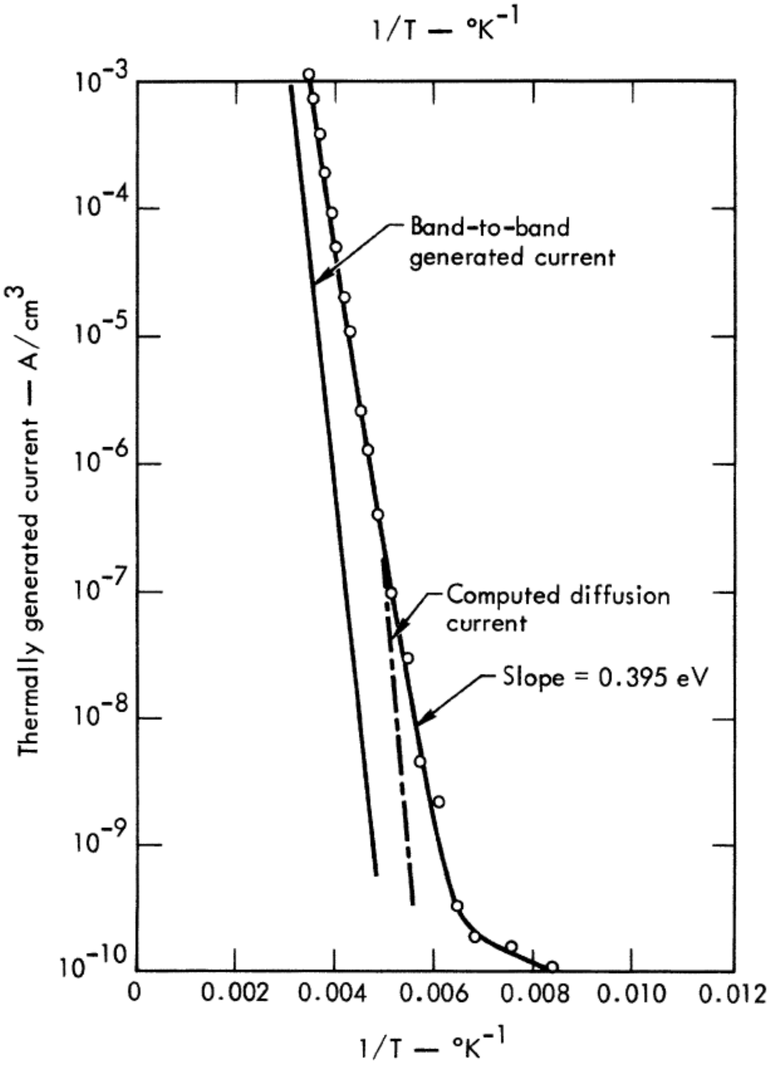

Figure 2.20: Thermally generated current as a function of temperature [27].

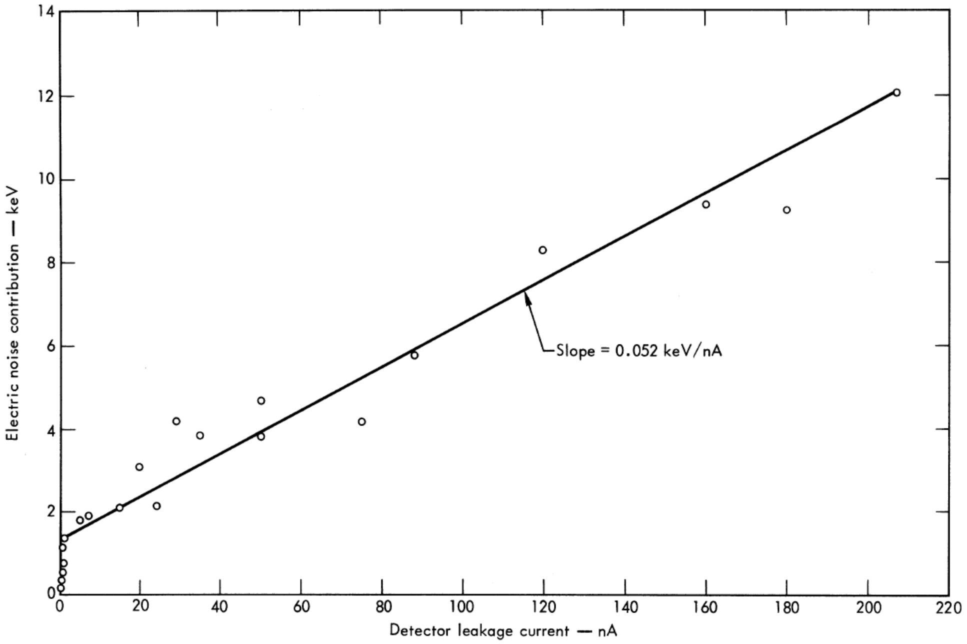

Figure 2.21: Electronic noise contribution versus detector leakage current [27].

2.7.3. Pehl, Haller and Cordi Investigation

In 1973, Pehl, Haller, and Cordi attempted to extend the previous research on a series of high purity and lithium drifted germanium detectors. In a similar manner to the Nakano research, this study provided further evidence of the relationship between leakage current as a function bias voltage and temperature as well as energy resolution performance as a function of temperature.

Table 2.4: Detector properties for the detectors used for the evaluation in the Pehl, Haller, and Cordi study of 1973 [45].

Detector	Type	Diameter (cm)	Thickness (cm)	Depletion Voltage (V)	Maximum Voltage (V)	^{60}Co (1.17MeV) FWHM Resolution
172-7.0	P skin / N core	3.2	1.0	400	2000	1.7
195-3.2	P	3.0	1.0	400	2200	1.6
158-4.0	N	2.7	1.0	250	1500	1.7
214.60	P skin / N core	2.8	1.0	100	1500	1.6
155-1.0	P	1.0	0.5	250	600	1.6
155-1.8	P	1.0	0.5	250	500	1.6
102-3.0	Li-drifted	2.3	0.9	--	3500	1.7
215-5.0	P (homogeneous)	3.4	0.225	50	400	--
133-9.0	P (homogeneous)	2.5	0.4	400	1000	No peak
217-5.0	P (homogeneous)	1.8	0.8	400	1200	--

The energy resolution measurements reported in table 2.4 were taken standard cryostats that maintained the detector temperature at approximately 85°K [27]. This study was able to confirm some of the observations seen in the Armantrout and Nakano studies previously reviewed as well as provide some additional observations and conclusions. Considering observations that we consistent with previous research, the Pehl study was able to show the same relationship of increasing leakage current as a function of bias voltage plotted at various temperatures. This observation can be seen in figure 2.22.

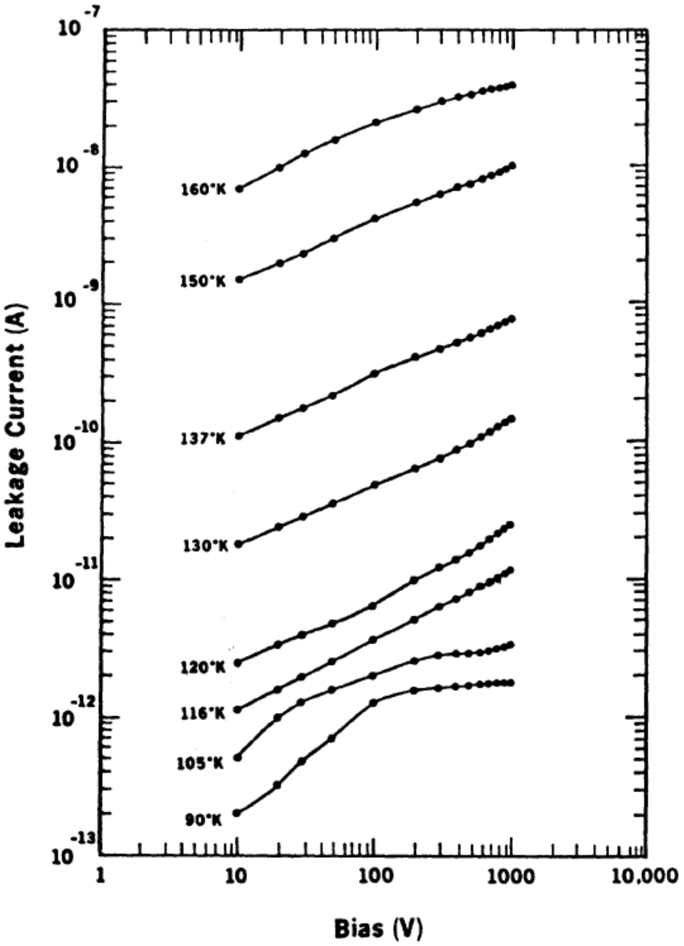

Figure 2.22: Voltage-current characteristics as a function of temperature for detector 214.6.0[45].

Two key observations can be taken from figure 2.22. The first of these observations is the relationship between bias voltage and leakage current. As the bias voltage increases at a given temperature, the leakage current also increases. The second observation that can be taken is that as the temperature increases, at a given bias voltage, the leakage current also increases.

The Pehl study also provides indication that there is no significant difference between the temperature-resolution relationship observed on lithium-drifted and the high purity germanium detectors [45]. Pehl further references the Armantrout study in regard to this conclusion. The apparent discrepancy between these measurements and the conclusions of Armantrout [27] can be explained by the fact that Armantrout compared relatively large lithium-drifted detectors with very small high purity detectors [45]. Figure 2.23 provides the results of the comparison of all detectors; lithium drifted and high purity.

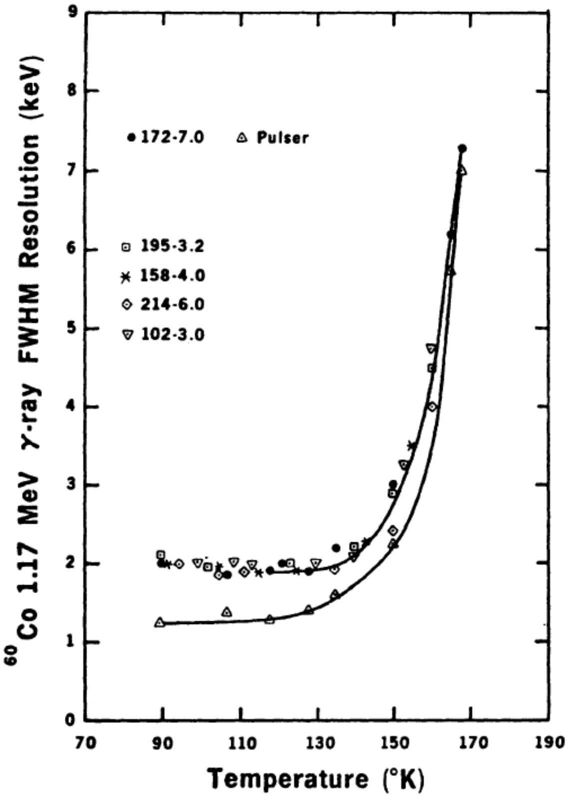

Figure 2.23: Energy resolution of the ^{60}Co 1.17 MeV gamma ray obtained with five detectors as a function of temperature [45].

Further, Pehl advises that measurements made with very small detectors should not be used to generalize the performance of much larger detectors. The Pehl study does, however, provide an indication that shaping times can be used to improve the energy resolution of the detector. Figure 2.26 shows the results obtained with a 0.2 cm^3 high purity germanium detector as a function of temperature. The amplifier peaking time was set at 2.25 μsec to minimize the effects of leakage current noise. This technique is increasingly effective for thinner detectors. This is due to the fact that charge mobility decreases rapidly with temperature [46]. The drift velocity ν is proportional to the applied field. Accordingly, the mobility μ for the electrons and holes can be defined by [14];

$$\nu_h = \mu_h \mathcal{E} \tag{2.18}$$

$$\nu_e = \mu_e \mathcal{E} \tag{2.19}$$

where $\mathcal{E}$ = electric field magnitude

In germanium, the mobility of the electron and hole are of the same order of magnitude. Electron and hole mobility values at different temperatures are provided in table 2.5. The drift velocity is also dependent on the value of the electric field up until the point where a saturation velocity is achieved. At this saturation velocity, further increases in the electric field do not affect the velocity further. This is demonstrated in figure 2.24 (electrons) and figure 2.25 (holes).

Table 2.5: Mobility properties of intrinsic silicon and germanium

	Si	Ge
Electron Mobility (300 °K); $cm^2/V \cdot s$	1350	3900
Hole Mobility (300 °K); $cm^2/V \cdot s$	480	1900
Electron Mobility (77 °K); $cm^2/V \cdot s$	2.1×10^4	3.6×10^4
Hole Mobility (77 °K); $cm^2/V \cdot s$	1.1×10^4	4.2×10^4

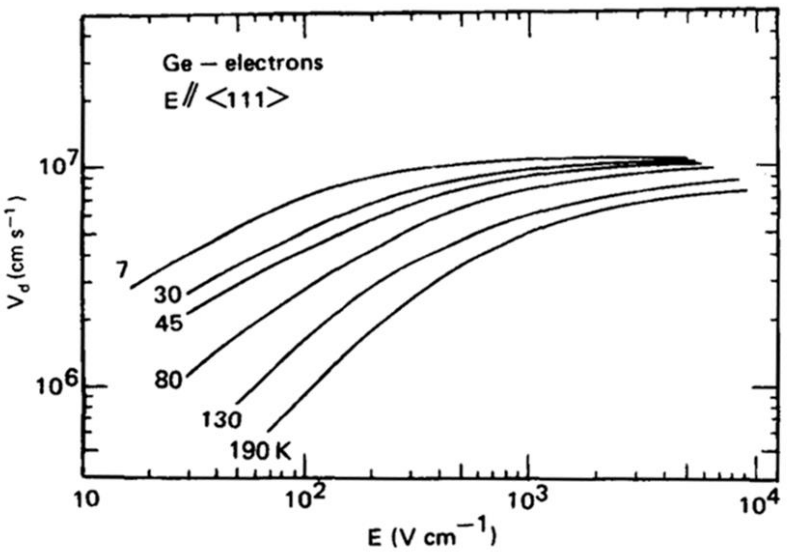

Figure 2.24: Drift velocity as a function of parallel applied electric field at absolution temperature for electrons in germanium [14].

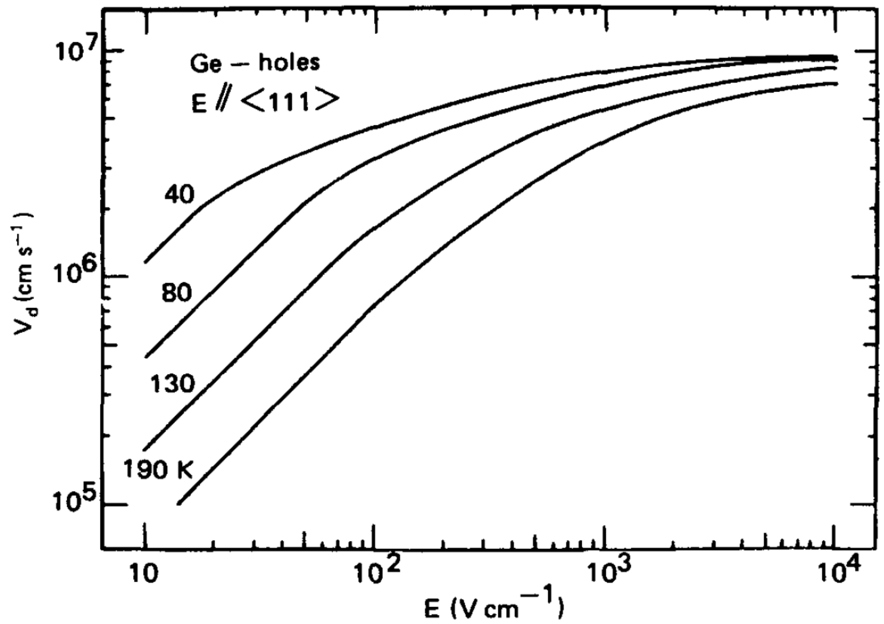

Figure 2.25: Drift velocity as a function of parallel applied electric field at absolution temperature for holes in germanium [14].

In many situations, the semiconductor detector is operated at electric fields that are sufficient to achieve saturation drift velocity. These saturation velocities are in the order of 10^7 cm/s [14]. Accordingly, the collection time required over typical dimensions of 0.1 cm is under 10 ns.

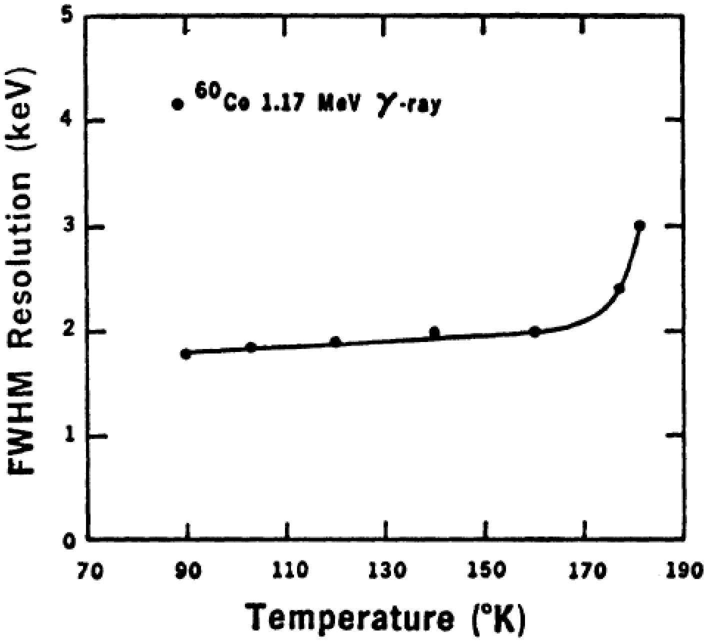

Figure 2.26: Energy resolution of the ^{60}Co 1.17 MeV gamma ray obtained with a 0.2 cm^3 detector as a function of temperature. This detector used an amplifier peaking time of 2.25 μsec in order to minimize the effects of the leakage current noise [45].

2.7.4. Nakano, Simpson, and Imhof Investigation

Up until 1977 the research conducted on the operational characteristics of germanium detectors operating at elevated temperature appears to have focused on smaller detectors (<35 cm^3). In 1977, Nakano, Simpson, and Imhof investigated the operational characteristics of two 'large' intrinsic germanium detectors. The volumes of these detectors were 25cm^3 and 75cm^3 [47]. For this research, two commercially available, single ended coaxial, detectors were used with the following properties.

Table 2.6: Detector properties for the detectors used for the evaluation in the Nakano, Simpson, and Imhof research of 1977 [47].

Parameters	Detector Serial No.	
	125	323
Nominal Volume	25 cm3	75 cm3
Diameter	31 mm	47-49 mm
Length	35 mm	42 mm
Depletion Voltage	~2000 V	2300 V
Efficiency	4.1%	14.3%
Resolution (1.33 MeV) FWHM	1.99 keV	1.96 keV
Resolution (1.33 MeV) FWHM	3.90 keV	3.70 keV
Peak to Compton Ratio	25	40

The temperature of each of the detectors was measured using thermocouples embedded into the copper cold finger of each assembly. A heater was used as a means of controlling the temperature of the detector. Each detector was studied through a range of temperatures between 100ºK and approximately 200ºK with a number of relevant conclusions / observations. This study was successful in demonstrating the same increasing leakage current as function of bias voltage and temperature with a larger volume detector. This relationship is seen in figure 2.27. This observation, coupled with the results shown in the previously identified studies suggests that the relationship between leakage current and increasing temperature and increasing bias remains present with increasing detector volume. This observation is of particular interest and relevance to the research associated with this dissertation as the volume of the detectors used is significantly larger (~180 cm^3).

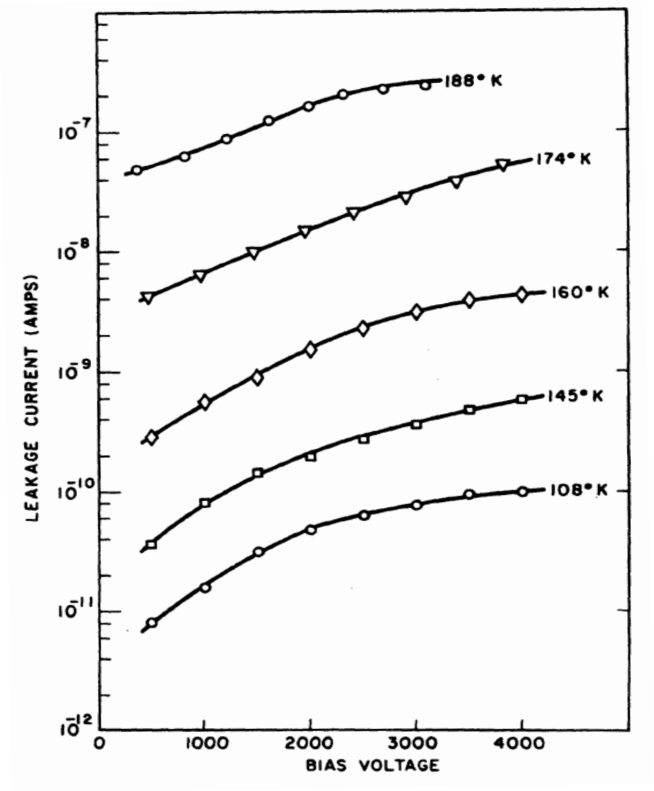

Figure 2.27: Detector leak current presented as a function of bias voltage and temperature in the 75 cm^3 detector [47].

This study was also successful at depicting the leakage as a function of temperature and volume. In figure 2.28 shown below, the leakage current of the two detectors used in this study were plotted against temperature.

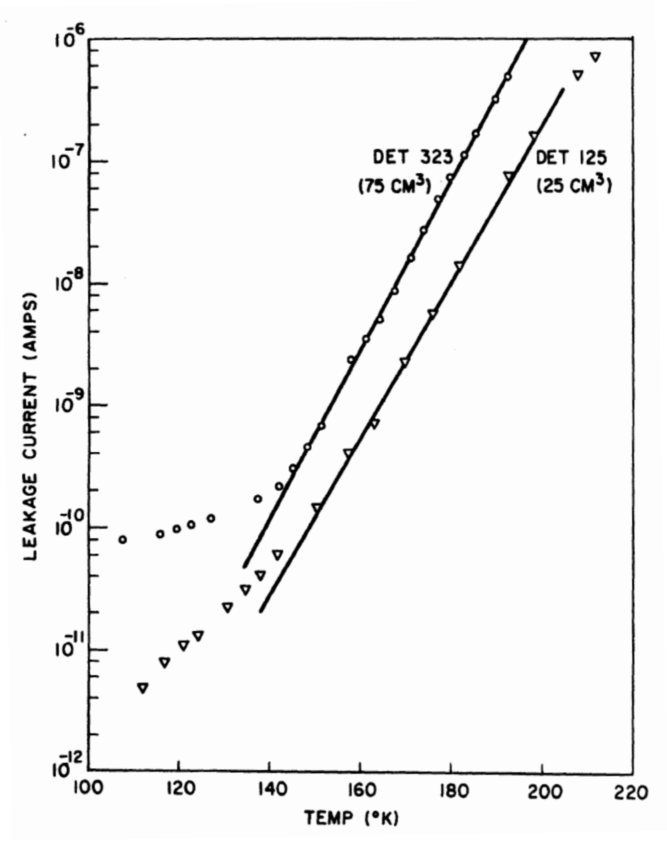

Figure 2.28: Detector leak current presented as a function of temperature [47].

The research publication points out an interesting observation; the ratios of the leakage currents exceeds the ratio if the detectors corresponding volumes [47]. Finally, Nakano, Simpson, and Imhof summarized the energy resolution performance of each detector as shown in figure 2.42. The resolution curve for the smaller of the two detectors maintains a very flat profile below 160°K and then begins to degrade rapidly above the knee at around 170°K. The energy resolution performance of the larger of the two detectors does not exhibit as flat of a profile below the knee which occurs between 155°K and 160°K.

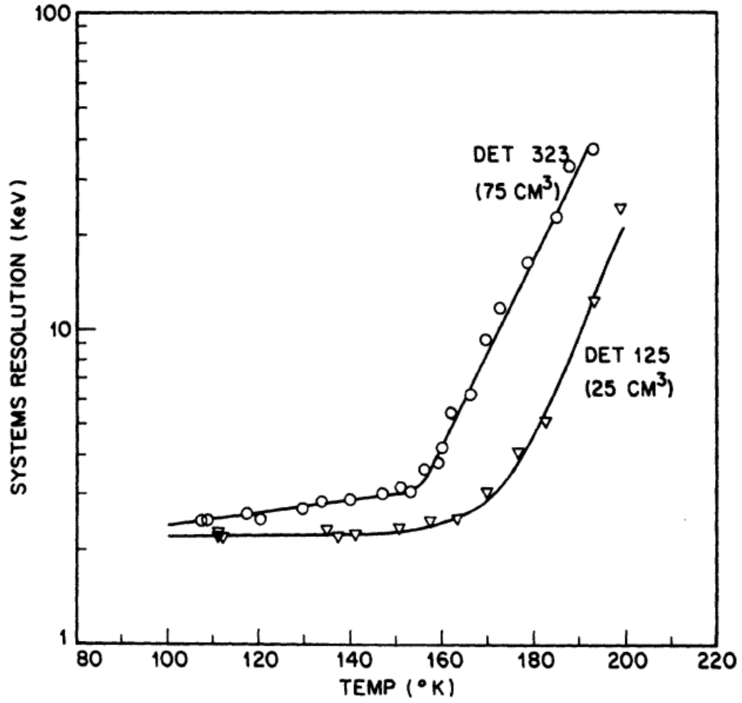

Figure 2.29: System energy resolution for the two detectors used in the Nakano, Simpson, and Imhof study of 1977 [47].

Nakano, Simpson, and Imhof conclude that on the basis of limited data, it appears that there are advantages of utilizing intrinsic instead of Ge(Li) detectors due to their ability to perform exceedingly well over a large range of operation temperatures [47].

2.8. History of Mechanically Cooled Designs

HPGe detectors have traditionally been cooled with liquid nitrogen (LN_2). This proved to be inconvenient for field use. Maintenance, operating cost, availability at remote locations, and the hazardous nature of liquid nitrogen all combine to limit the practicality of a LN2-cooled device. These challenges drove the development efforts to replace liquid nitrogen with a mechanically cooled device. The first mechanically-cooled HPGe systems appeared commercially in the early 1980s [48]. At that time, three categories of mechanical cooling were used: thermoelectric, Joule-Thompson refrigerators, and closed-cycle cryogenic mechanical refrigerators powered by electric motors [48]. Despite achieving the removal of LN2, these mechanical systems were primarily used as laboratory detectors due to the size and power requirements of the system. The Joule-Thompson systems weighed as much as 25 pounds and used as much as 300W of power in steady-state operation [48]. Size and portability was improved with the use of Stirling-cycle coolers in HPGe systems. Current, commercially available Stirling-cooled systems typically operate between 100ºK and 110ºK.

One example of a Stirling-cycle design is the LLNL-designed Stirling cycle cooler used in the Field Radiometric Identification System, FRIS [49]. In this design, the Stirling cooler was battery operated and transportable. The device demonstrated an improvement over what one may achieve with scintillation detectors [50]. The device did, however, require significant battery capacity to operate. Steady state power consumption was nearly 60W [49]. Such battery consumption makes the overall weight of the design a challenge for a truly portable device.

In 2002, LLNL presented a mechanical cooled, HPGe detector called the Cryo3. The Cryo3 offered improvements in weight and battery size to the FRIS design. The miniature Stirling cooler used in the Cryo3 design required only 15 W of power input. However, the cooler itself is limited in its cooling capacity to the point that the Cryo3 can only operate a small HPGe detector element. Additionally, it requires the use of a Peltier cooler to cool an internal infrared shield [51]. The novel detector design developed as a part of this research does not incorporate an internal infrared shield. This driven inner shield reduces the radiative heat load of the HPGe detector element. The Cryo3 also suffers from poor energy resolution with measured values of 3.5 keV Full Width Half Max at 662 keV [48].

In 2002, ORTEC also began development work on a small, handheld, battery-powered HPGe design. This system utilized a larger capacity cooler allowing for performance improvements over the previously discussed Cryo3 [48]. The cooler used in this design was the SAX101-002B cooler from Hymatic Engineering, Ltd. [48]. This cooler used less than 16W at steady state operation. The size of the cooler required is determined by the total heat load of the system. These mechanical designs utilized a malleable copper braid as means of providing a thermal path between the cooler cold finger and the detector housing [52]. The malleability of the copper braid served to minimize the microphonic vibration introduced to the system.

In 2002, additional efforts were also being applied to develop modified digital filtering for processing the preamplifier signal to correct for the microphonics with software rather than through mechanical means [48]. This digital filtering corrected the pulse output signal for any changes in the baseline caused by the microphonics. This concept will now be reviewed in further detail. Consider Figure 2.30. The left hand side of Figure 2.30 displays the typically voltage step output produced at the preamplifier stage as the result of charge collection produced by the absorption of a gamma-ray. The right hand side of Figure 2.30 shows the resulting trapezoidal weighting function in a digital spectrometer. The height of the step pulse is estimated by averaging the digitalized samples of the signal before and after the step. An ‘M’ number of samples immediately after an event are first ignored. This allows for a maximum rise time of M times the sample interval to be achieved. N samples after the rise time samples are then averaged. This average is subtracted from the average of the baseline before the event. The defined procedure results in a trapezoidal weighting function with a rise time of N sample intervals and a flat top of M sample intervals. The maximum value of the trapezoidal output provides the best estimate of the step height. This represents the energy of the incident gamma-ray. With a proper selection of M and N, this filter is very nearly the optimum filter for a system with noise arising only from the detector leakage (parallel noise) and the FET current (series noise) [48]. The averaging and subsequent subtraction removes the DC component of the signal. This essentially enables the filter to independent of DC offsets. Figure 2.30 shows the output of the trapezoidal filter is equal to the slope of the baseline signal multiplied by the full width at half maximum of the trapezoid. If a step pulse were to be measured on such a baseline, the filter output value will be too high by an error equal to the difference in the average values A_1 and A_2. Since the microphonic noise component in a signal is approximately a sine wave as illustrated in Figure 2.31, the error induced can be positive, negative or zero. This error signal contributes as a widening of the spectral lines thus appearing as degraded resolution performance from the detector. This can be a dominant noise source especially at lower energies.

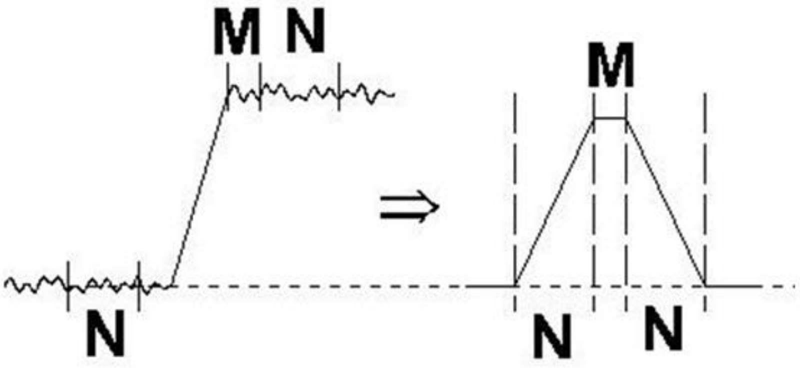

Figure 2.30: Typical trapezoidal weighting function (right) arising from detector preamplifier output signal (left) [48].

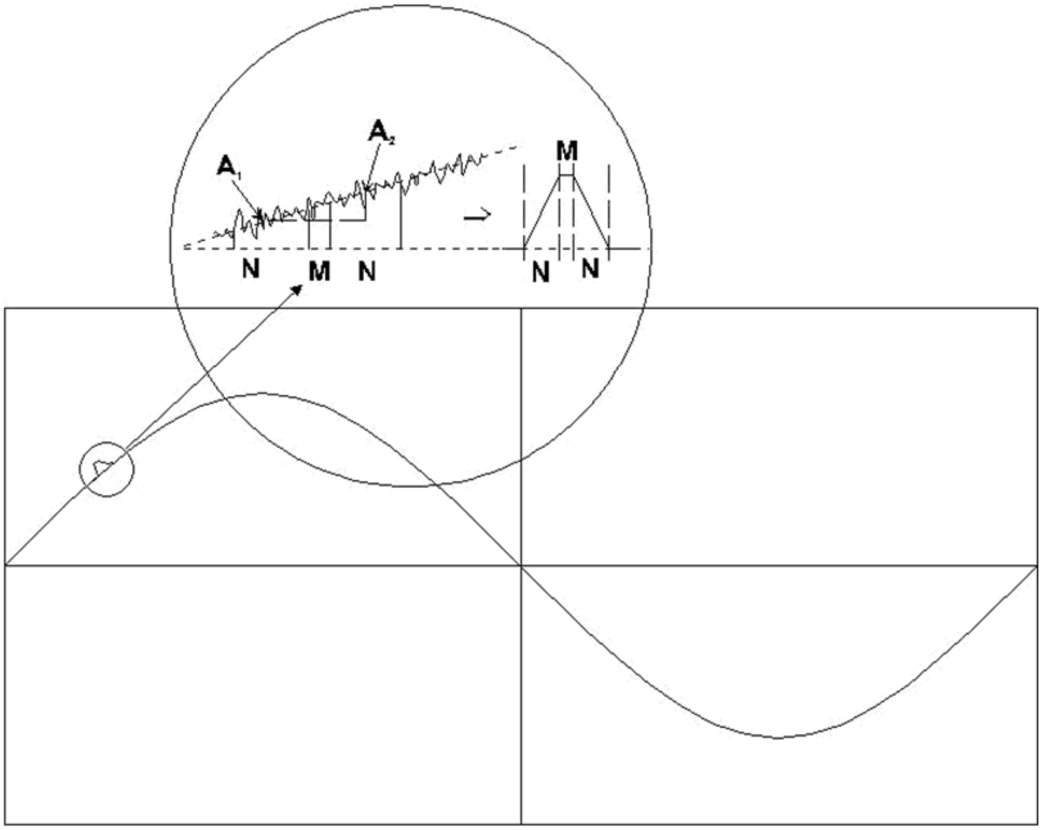

Figure 2.31: Low frequency noise (shown as a sine wave) and the resulting weighting function output [48].

2.9. Original Contributions

This dissertation presents work performed to understand the performance limits of high purity germanium at elevated operating temperatures. This understanding has been achieved in the context of a novel type of mechanically cooled HPGe detector assembly which will be described in Chapter 3. In addition to this new detector design, this dissertation work is intended to expand the prior research in the area of elevated temperature operation of HPGe in two regards. Previous studies used detectors that were liquid nitrogen cooled whereas this research investigates mechanically cooled detectors. This research can also be considered an expansion of previous research in that the size of the detectors studied is larger than previous. Previously identified research is limited to 75 cubic centimeter volume detectors whereas detectors up to 180 cubic centimeters are investigated here. This research also quantifies the microphonic noise contribution from the new cryocooler design. Design implications for lower mass, handheld high purity germanium detectors are also discussed.

2.10. Dissertation Overview

This dissertation investigates a new design for a more portable mechanically cooled high purity germanium detector as well as energy resolution performance as a function of temperature for such as design. Chapter 3 will provide an overview of the novel detector assemblies that have been designed and tested as a part of this dissertation. Sufficient detail will be included in Chapter 3 to provide the reader a complete understanding of the design. Chapter 4 will transition immediately into the experimental setup and testing procedure used for the characterization of each detector as a function of operating temperature. Chapter 5 will provide a review of the test results achieved through the characterization testing. In addition to providing the measurement results, Chapter 5 will also provide discussion and explanation of the results themselves. Finally, Chapter 6 will provide conclusions regarding sources of detector system noise and in operating high purity germanium detectors at elevated temperatures.

Chapter 3

Design of a Novel Directly Coupled HPGe Detector Assembly

Figure 3.1 shows the detector construction designed as a part of this research. This design construction represents a significant departure from the commercially available, hand held, high purity germanium systems that utilize a thermal braid or thermal spring to couple between the cryocooler and the detector housing. This is done for the primary reason of isolating the cryocooler from the detector for the minimization of any microphonic noise contribution. The disadvantage of this approach, however, is reduced thermal transfer between the cooler and the detector and associated cooling performance. As mentioned previously, the direct coupling approach differs from the currently available commercial detectors that utilize a copper braid thermal couple between the cooler cold finger and the detector housing. This approach is done specifically to reduce the microphonic contribution from the cooler.

The direct coupling approach offers two very distinct advantages that were of interest for this work. The first of the two advantages is thermal-cooling efficiency. By directly coupling to the cryo-cooler cold finger itself, the need for the coupling braid (or alternative mechanical-thermal bridge elements) is eliminated. All thermal losses or inefficiencies associated with such a mechanical-thermal bridge can be eliminated. This does present the situation of higher potential microphonic contributions to the energy resolution of the device. This is a direct result of the detector being rigidly mounted to the cooler versus the detector being independently mounted from the cooler and thermally coupled through the braid only. The flexibility of the copper thermal braid prevents the microphonic vibration of the cooler from directly transferring into the detector housing itself. Microphonics refers to mechanically generated noise resulting from such sources as bubbling of nitrogen in the dewar or moving components within the cryocooler itself [53]. This contribution has been measured as a part of this research for a split-Stirling cooler design and is shown to contribute up to 1.5 keV of energy resolution degradation at 122 keV. Full results are reported in chapter 5. The second of these advantages is packaging. In theory, much smaller cryostats can be developed with this approach. The detector design includes each of the following main components:

1. Mechanical Cryocooler / Cold Finger
2. Direct-Coupled Detector Housing
3. HPGe Detector
4. Integrated Electronics
5. Detector Endcap / Encasement

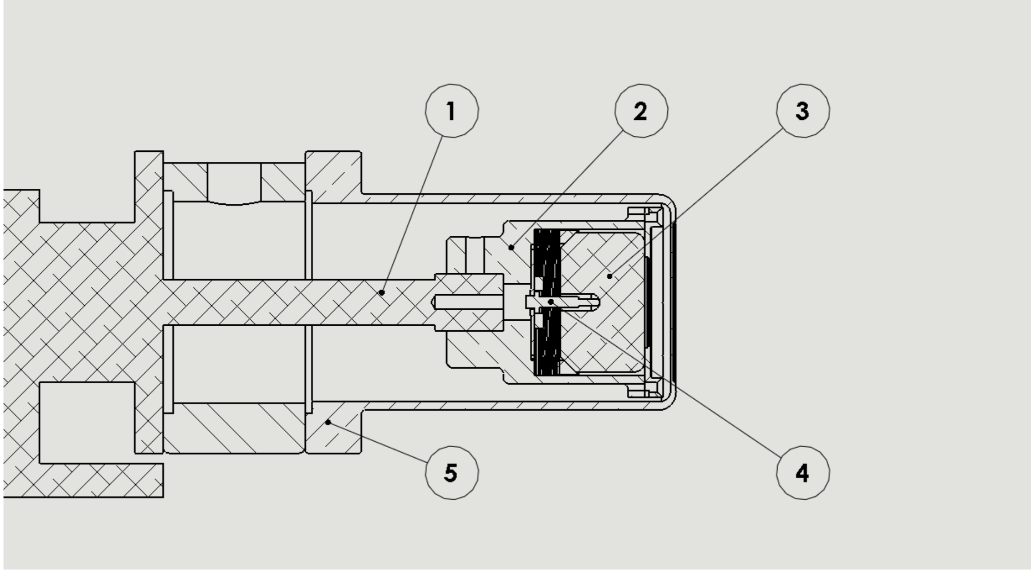

Figure 3.1: Basic design for a miniature high purity germanium detector used to conduct temperature and microphonic characterization.

3.1. Mechanical Cooler

Item 1 in Figure 3.1 is the cold finger extension of the dual piston, split Stirling cryocooler used. Conventional operation of HPGe detectors uses liquid nitrogen at a nominal 77K temperature value. For field deployment, this represents a non-practical limitation. One important consideration for this design is that since mechanical coolers are based on moving mechanical parts, their connection with the HPGe crystal must be carefully engineered to avoid compromising the system energy resolution by introducing vibration [14]. Joule-Thompson coupled HPGe detector designs have been shown to exhibit as much as 7% degradation in resolution performance versus the same detector cooled with liquid nitrogen [54]. The level of resolution degradation can be slightly higher on a direct coupled design – as much as 20% degradation at the 135^{o}K operating temperature. A form of electronic noise known as microphonics is a consequence of vibration and can result in a resolution that is inferior to that of liquid nitrogen cooling. The microphonic contribution of the cryocooler is due to the fact that for a split Stirling cooler, the regenerator/displacer has moving mechanical parts. The movement of the displacer results in mechanical vibrations termed microphonic noise [55]. A simplified representation of a split Stirling cryocooler can be seen in Figure 3.2.

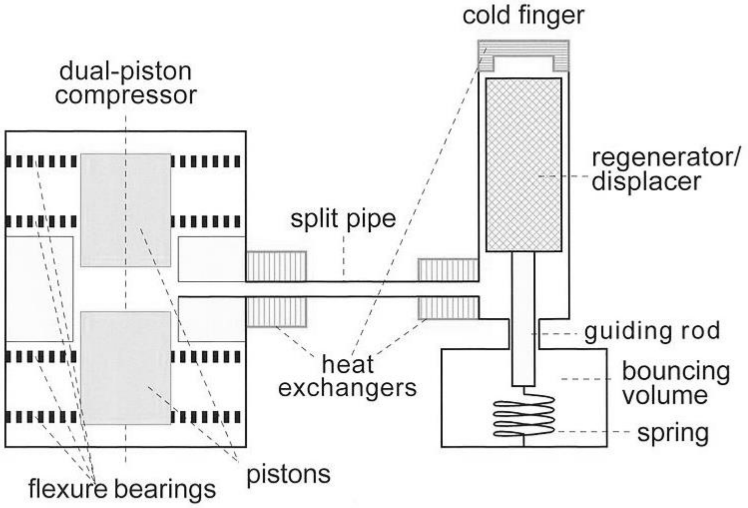

Figure 3.2: Simple cross section representation of a split Stirling cryocooler [70].

Miniature split cryocoolers are available in both single and dual piston configurations. The most popular commercial application for these types of coolers is for infrared photon detection and imaging. Stirling coolers have been used in other commercially available HPGe radiation detection systems. Current, commercially available mechanically cooled systems typically operate between 100ºK and 110ºK. Figure 3.2 shows a dual piston configuration. This research also used dual piston coolers for all testing completed. The cryocooler is made up of three basic components; the compressor, split pipe, and coldfinger (regenerator/displacer). The compressor and coldfinger are connected by a small internal delivery tube. The cooler is charged with high purity helium gas which serves as the refrigerant of the system. The gas is compressed inside the piston-cylinder assembly by the axial movement of the piston. The piston moves at a frequency between 50 and 75 Hz. This movement generates axial thrusts due to inherent inertia, which in turn generates high vibrations [71]. The gas then expands in the coldfinger allowing for the completion of the Stirling cycle.

3.1.1. Stirling Cycle

The Stirling cooler works on the principle of Stirling cycle. In the Stirling cycle, the compressor cyclically presses the working fluid and presses it back and forth between the hot and cold regions across a regenerative heat exchanged (coldfinger). The pressure-volume (PV) and temperature-entropy (TS) diagrams have been provided in Figure 3.3. The compression (1-2) and expansion processes (3-4) occur as isothermal processes and regenerative cooling (2-3) and heating (4-1) occur as constant volume processes. The overall performance and cooling capacity of all Stirling cycle coolers depends on the swept volume ration, the phase angle and the temperature ration [72]. The energy resolution degradation associated with this microphonic contribution will be specifically measured. The results for these measurements will be reviewed in Chapter 5.2.

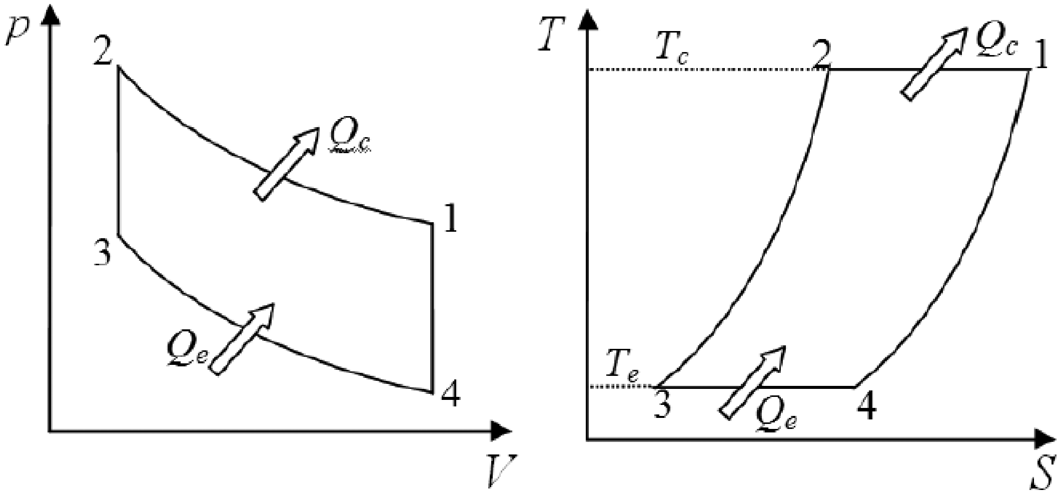

Figure 3.3: Ideal Stirling cycle. The figure on the left is the pressure-volume diagram and the figure on the right is the temperature-entropy diagram [72].

3.1.2. Mechanical Vibrations

The mechanical vibrations produced by Stirling cryocoolers introduce an additional source of degradation to the energy resolution of the detector system. Stirling coolers have several sources of vibration. The first of these sources is the Stirling cycle itself. Cooling is achieved through the controlled motion of mechanical elements (a piston and a displacer) to alternately compress and expand a working fluid [73]. The linearly reciprocating motion of these elements gives rise to a momentum imbalance. Although the piston is driven with a sinusoidal signal, it oscillates against the nonlinear gas spring of the compression space, resulting in a nonsinusoidal piston motion. This manifests itself in the cooler-generated vibration through the presence of harmonics of the piston's drive frequency [73]. An additional source of vibration present within Stirling cryocoolers is mechanical impact. Coolers that are designed for longer operational life feature linear motor controlled displacers; however, some coolers use free displacers. These free displacers are driven by pneumatic forces and have their travel limited by mechanical bumpers. Impact with these bumpers produces additional harmonic vibration. This introduces an additional source of noise and subsequent degradation of the detector system's energy resolution performance. At this time, further detail will be provided to characterize the mechanical equations of motion.

There are two masses that need to be considered. These two masses are the mass of the piston and the mass of the displacer. The mass of the piston and the associated components that are attached rigidly to it are shown in figure 3.4 as m_p [kg]. The combined mass of the displacer (with the regenerator and drive rod) is shown in figure 3.4 as m_d [kg]. The travel distances of the piston and displacer are defined as y_p and y_d, respectively. Each of these two distances is measured vertically from the upper face of the piston in its rest position ($y_p = 0$). The piston and displacer each have their own respective linear stiffnesses, shown in figure 3.4 as k_p [N/m] and k_d [N/m], respectively. The quantity F shall be defined as the driving force and is given in units of Newton [N]. Displacer motion and the corresponding expansion-space volume variations are the net result of instantaneous spring force, pressures acting on the exposed areas (and, assuming operation along the vertical axis, acceleration g [m/s^2]). The relationship of the mass, displacement, and pressure are [71]:

$$m_d y_d'' = (-m_d g) + k_d\left(Y_{sep} - y_d\right) + p_{buff} A_{xrod} + p_c(A_{xd} - A_{xrod}) - p_c A_{xd} \tag{3.1}$$

where Y_{sep} = separation distance between the regenerator and upper face of the piston

p_{buff} = instantaneous buffer space pressure

A_{xrod} = cross sectional area of the drive rod exposed to p_{cc}, and

p_c = variable crack shaft pressure

The piston experiences different pressures between the compression space and buffer space. In addition to the pressure differentials, the piston is also subjected to loading induced by the spring force and the driving force F_{sol} as follows [71]:

$$m_p y_p^{''} = \left(p_{buff} - p_c\right)\left(A_{xc} - A_{xrod}\right) - k_p y_p + F_{sol} \tag{3.2}$$

where: A_{xc} = cross sectional area of the case, and

F_{sol} = periodic driving force induced by the solenoid

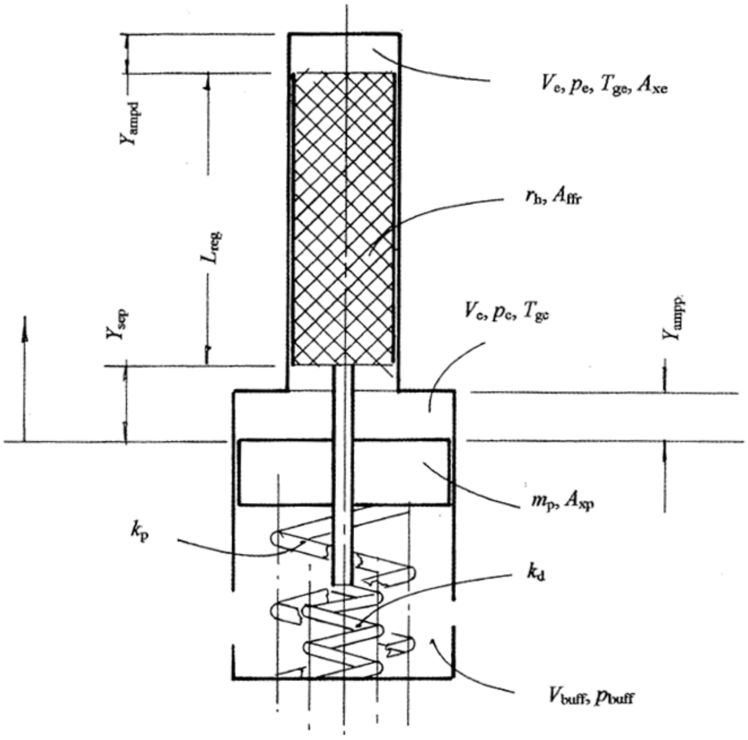

Figure 3.4: Schematic of the dynamic system formed by the piston, displacer, and associated spring system within a cryocooler [71].

3.2. Detector Housing

Item 2 in Figure 3.1 represents the detector housing. The detector housing serves multiple purposes in the design. The first of these functions is that it houses the detector itself. In addition, the detector housing provides a thermal path through which the detector can be cooled. Further, the detector housing provides a mounting location for the detector electronics. This last fact presents a practical challenge with this design that will be discussed shortly. One of the novel aspects of the design is that the detector housing is direct coupled to the cooler itself. This allows for more efficient cool down of the detector. Typical liquid nitrogen cooled detectors ranging in size from 10% to 150% detectors will cool down sufficiently within 2-6 hours of filling. This value is dependent on the size of the detector. Current commercially available detector systems may be as large as 150%. In this case, the cool down time may exceed the six hours previously specified. As a point of perspective, detector 1 used in this research achieved a cool-down sufficient for taking measurements in 30-45 minutes. This relatively short cool down time is a desirable feature for field deployed applications. Design protection is currently pending with the United States Patent Office. This protection is currently being done under U.S. Patent Application No. 14/059,534. Detector 2 cooled down on the order of 4.5 hours and detector 3 and detector 4 (approximately the same volume) achieved sufficient cool down in approximately 6 hours.

3.3. High Purity Germanium Detector

Item 3 in Figure 3.1 represents the high purity germanium detector. Each of the detectors tested were closed-ended coaxial detectors. The closed end of the detector has rounded corners to improve charge collection [75]. Each detector used was p-type. Figure 3.6

represents the solid model rendering of the design prior to build and test. Figure 3.7 represents the bench-top proof of concept that was developed for testing.

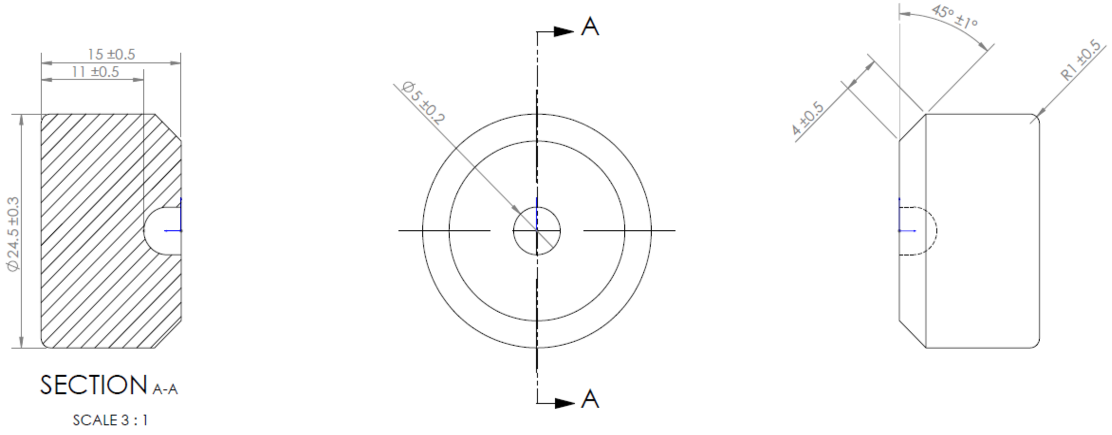

Figure 3.5: Representation of the detector geometry used.

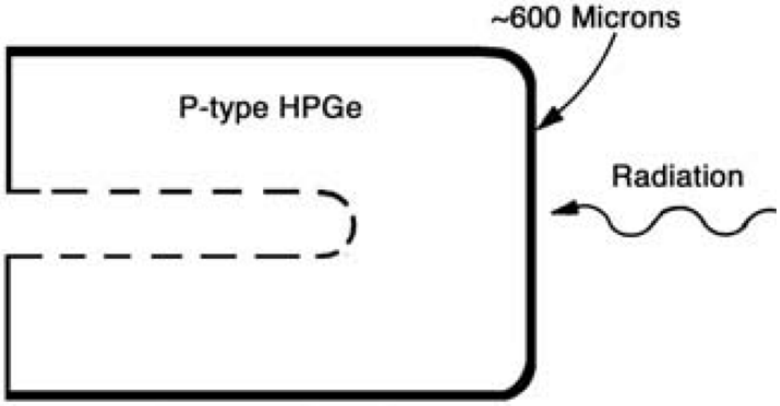

Figure 3.6: Basic diagram of the p-type, coaxial, HPGe detectors used for testing [36].

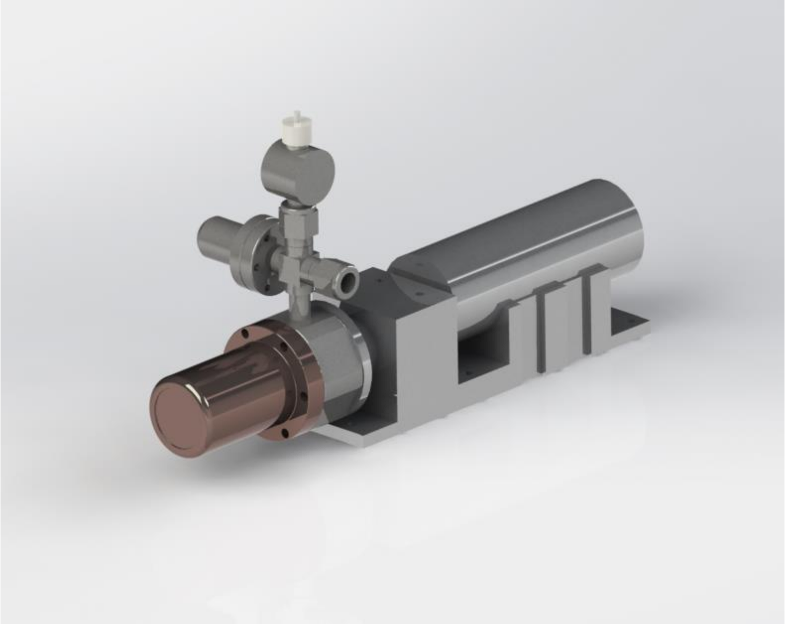

Figure 3.7: Solid model proof of concept design

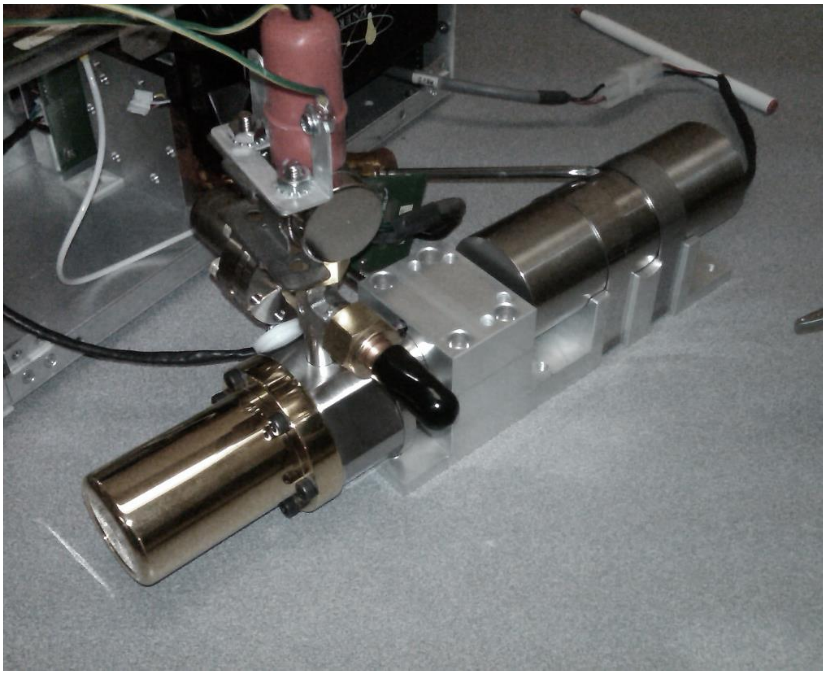

Figure 3.8: Detector design on test bench.

Chapter 4

Experimental Setup

4.1. Introduction

This research is framed around the desire to extend the prior research in two separate regards. The first is to extend the energy-resolution versus temperature research into larger detector volumes; up to 180 cm^3. The second area where this research will expand on the prior research is with the introduction of a new mechanical cooling design for use with HPGe detectors. Due to the moving parts within a split Stirling cryocooler [71], an additional component of noise (and associated energy resolution degradation) is introduced into the system. This research will characterize the additional noise component introduced by the cooler in the design.

4.2. Detector Geometry & Properties

Four different detectors were selected for use in this investigation and temperature characterization. The four detectors chosen had the following properties.

Table 4.1: Properties of the four detectors used.

Parameter	Detector No.			
	1	2	3	4
Nominal Volume (cm^3)	6.75	72.75	180.85	180.80
Diameter (mm)	24.5	55.0	67.0	85.0
Depletion Voltage (V)	700	2400	1600	1600
Operating Voltage (V)	875	3000	2500	3500
Efficiency ^{60}Co (%)	1.85	14.60	49.1	52.75
Peak to Compton Ratio	No data	51.4	70.95	59.19

All detectors used were p-type, coaxial detectors of varying geometry (diameter and length). In p-type material, the holes are the majority carrier and therefore dominate the electrical conductivity.

4.3. Measurement Configuration

Two specific industry accepted standards were referenced for the measurements taken as a part of this research. These two standards are as follows;

- IEEE Std. 325-1996(R2002): IEEE Standard Test Procedures to Germanium Gamma-Ray Detectors [76].

- ANSI N42.34-2006: American National Standard Performance Criteria for Hand-Held Instruments for the Detection and Identification of Radionuclides [77].

Figure 4.1 provides the general block diagram used to conduct all measurements. The basic test setup was kept consistent for all tests and measurements taken. The primary variable that did change throughout the testing was the geometry of the detector and the associated cryostat mechanical components. Care was taken to keep all other aspects of the detector assemblies as consistent as possible. For this research an in-house designed shaping amplifier was used. An amplifier peaking time of 2.5 μs was used for all measurements. The detector assembly is divided into two main sections: cryostat and signal analysis/management shown as 'computer' in Figure 4.1. The primary focus of this research and design work focused exclusively on the cryostat portion of the design. This was done due to the fact that the largest opportunities for improvement in regard to the overall reduction in weight reside in this section. What is not shown in the block diagram, however, is the cooling mechanism used in the 'cold region.' All detectors used in this study were mechanical, split-Stirling coolers. The particular relevance of this condition is the introduction of the observed microphonic noise into the design which will be reviewed thorough in the Chapter 5.

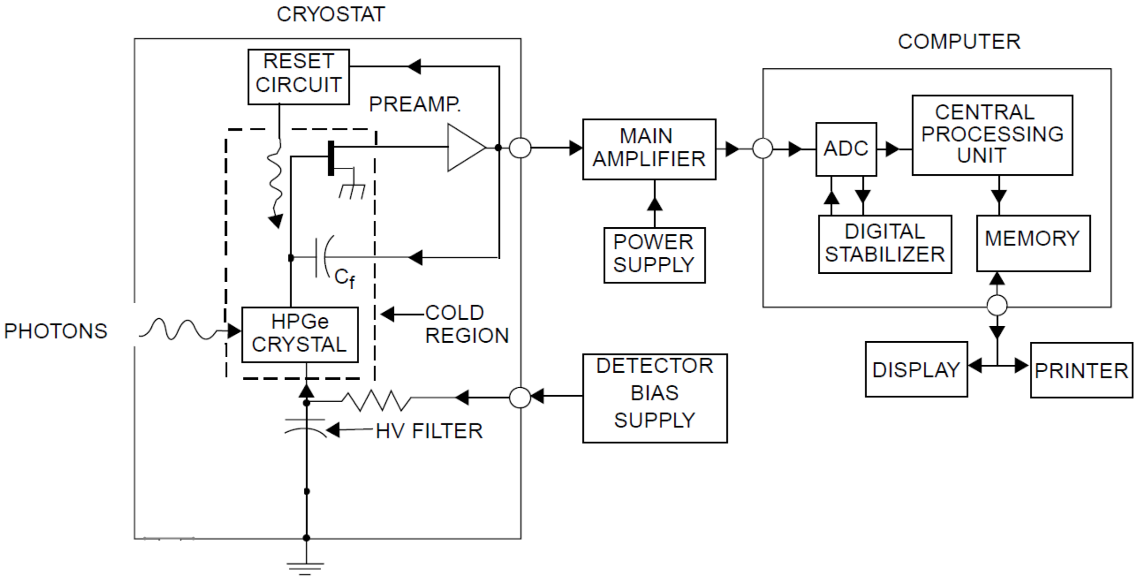

Figure 4.1: Basic block diagram of the detector assembly used for resolution measurements.

4.3.1. Test Setup and General Procedure

Chapter 4.3.1 will be used to describe the test setup and general procedure used for the temperature characterization measurements. Source placement, calibration, count consideration and general test methodology will be reviewed.

4.3.1.1. Source Placement

For all measurements taken, the following source placement was strictly maintained.

i. The source was located axially with respect to the detector element. Care was taken to ensure that source was position along the centerline of the detector crystal. For a coaxial detector, the centerline is axial with the inner diameter of the detector [34].

ii. The source was carefully measured to ensure that it was 25 cm from the face of the detector crystal face.

iii. The place of the source was positioned such that it was parallel with the face of the detector element.

iv. There was nothing but air in between the source and the detector assembly.

In addition to each of the above four provisions being carefully monitored and maintained, careful measures were taken to ensure that there were no high-Z objects such as shields, mechanical structures, etc. in the vicinity of the measurement setup. This was to ensure that there was no photon scatter into the detector element [78]. Also as mentioned previously, the same two sources (^{57}Co and ^{60}Co) were used throughout the duration of the test and measurement process.

4.3.1.2. Channel Width Calibration

For each measurement that was taken, the device was recalibrated prior to measurements being recorded. The following general calibration procedure was used. Each device, on each measurement, was calibrated in kiloelectronvolts per channel. Two peaks from the same two sources were used for all devices and for all measurements. Specifically, the 1332.5 keV line of ^{60}Co and the 122.1 keV line of ^{57}Co were used. The choice of ^{57}Co and ^{60}Co was made purely on the basis of availability. Other sources that are commonly used for resolution measurements can be seen in table 4.2.

The specific source information at the time that the measurements were taken was as follows.

- ^{57}Co: Total decay corrected activity of 26 μCi at the time of start of measurements.
- ^{60}Co: Total decay corrected activity of 70 μCi at the time of start of measurements.

For each measurement that we made, the calibration of each detector assembly we repeated. Consistent with the prescribed procedure defined in IEEE Std. 325-1996(R2002), all calibrations were completed on the basis of gamma-ray energy.

Table 4.2: Commonly used radionuclides used for the determination of energy resolution [22].

Radionuclide	**Half-life**	**Energy**
^{55}Fe	2.74 years	5.90 keV
^{241}Am	433 years	59.54 keV and 26.3 keV X-rays
^{109}Cd	463 days	22.2 keV and 88.0 keV (X-ray doublet)
^{57}Co	272 days	122.1 keV and 136.5 keV
^{137}Cs	30.2 years	661.7 keV
^{22}Na	2.60 years	1274.5 keV
^{60}Co	5.27 years	1173.2 keV and 1332.5 keV
^{208}Tl	1.91 years	2614.5 keV (^{228}Th source)

The energy calibration function calculates two sets of parameters: the energy vs. channel number, and the peak shape or FWHM vs. energy. The inputs to this function are the spectrum or series of spectra with isolated peaks distributed over the energy range of interest, and either a library or table of peak energies. The library referred to here is an analysis gamma-ray library. The equation used for energy vs. channel number is as follows.

$$E = a_1 + a_2C + a_3C^2 \tag{4.1}$$

where: E = Energy

a_i = coefficients, and

C = channel number

The equation used for FWHM vs. channel is as follows.

$$F = b_1 + b_2C + b_3C^2 \tag{4.2}$$

where: F = FWHM in channels

b_i = coefficients, and

C = channel number

The FWHM is then calculated in energy using the following equation.

$$F(e) = F(c)(a_2 + 2a_3 * C) \tag{4.3}$$

where: FI = FWHM in energy
I(c) = FWHM in channels at channel C
a_2 = energy calibration slope defined in equation 5.1
a_3 = energy calibration slope defined in equation 5.1, and
C = channel number

When the FWHM fit is made, the fit is automatically checked for validity.

4.3.1.3. Number of Counts in Peak

For each of the calibrations performance resolution measurements taken, this research used a minimum of 10,000 counts accumulated at the photopeak centroid. This proved to not be a problem with the source strengths that were being used.

4.3.1.4. Test Procedure

Care was taken to ensure that test conditions were maintained as consistent and repeatable as possible. Each detector was allowed to reach uniform and stable temperature at the time the measurements were taken. This was achieved by only taking one test measurement per day per detector. This would provide confidence that the detector has completely and uniformly achieved the desired temperature throughout the detector. The following represents the general test procedure that was used in an identical manner throughout the duration of the testing performed.

Each detector was arranged in a specific location on the test bench with adequate clearance around each detector. This was done to ensure that there are no scattering effects that may alter the measurements taken. Each detector would remain in the same location throughout the duration of the testing. Each detector was initially set at 100^{o}K. Prior to conducting the calibration and measurements, each detector was checked to ensure that the desired detector temperature was achieved. In addition, general condition/performance was checked. Care was taken to ensure that the same sources were used throughout the duration of the test. These sources were the ^{57}Co and the ^{60}Co discussed previously.

In the same order and with the same daily steps, each detector was calibrated on the 122.1 keV and 1332.5 keV energy peaks of ^{57}Co and ^{60}Co respectively. Once all detector assemblies had been calibrated, measurements were taken on each detector assembly in the same order as they were calibrated. Excellent care was taken to ensure that the source placement was consistent for all calibrations and measurements taken. This was made possible through the use of placement fixtures designed specifically for each detector assembly. This measure was done to ensure that there were no measurement variations due to source placement. Each detector assembly was allowed to achieve a minimum of 10,000 counts at each of the 122.1 keV (^{57}Co) and 1332.5 keV (^{60}Co) energy lines respectively.

Once the 10,000 counts had been achieved, the energy resolution was taken at both the 122.1 keV and 1332.5 keV peaks. In addition to recording the FWHM at each peak, the full width at 1/5 max was also recorded. This is referred to as FW(0.2)M. This nomenclature is used throughout the remainder of the dissertation. Once the FWHM and the FW(0.2)M energy resolutions have been recorded the cooler was then disabled. This provided energy-resolution measurements without the cooler in operation. The difference of the two energy-resolution measurements (with cooler on and with cooler off) is the microphonic energy-resolution degradation in eV.

After all measurements were taken, the detector temperature set points were increased by 5^{o}K. In order to ensure that each detector has achieved temperature equilibrium at the elevated temperature set up, a period of 24 hours was allowed prior to conducting the next round of testing. The procedure was then repeated on a daily basis starting at step 3 with the new temperature.

Chapter 5

Results and Discussion

This chapter reviews the results of measurements performed. The format for reporting the results will be as follows. For each of the detector sizes the resolution versus temperature plots will be provided. In addition, the table of associated data will also be included.

The first set of graphs for each detector will be with the cooler on. These will then in turn be followed up by similar resolution data with the cooler off. This data will be overlaid on the original ‘cooler on’ data so that the two can be referenced.

5.1. Detector Results with Cooler On

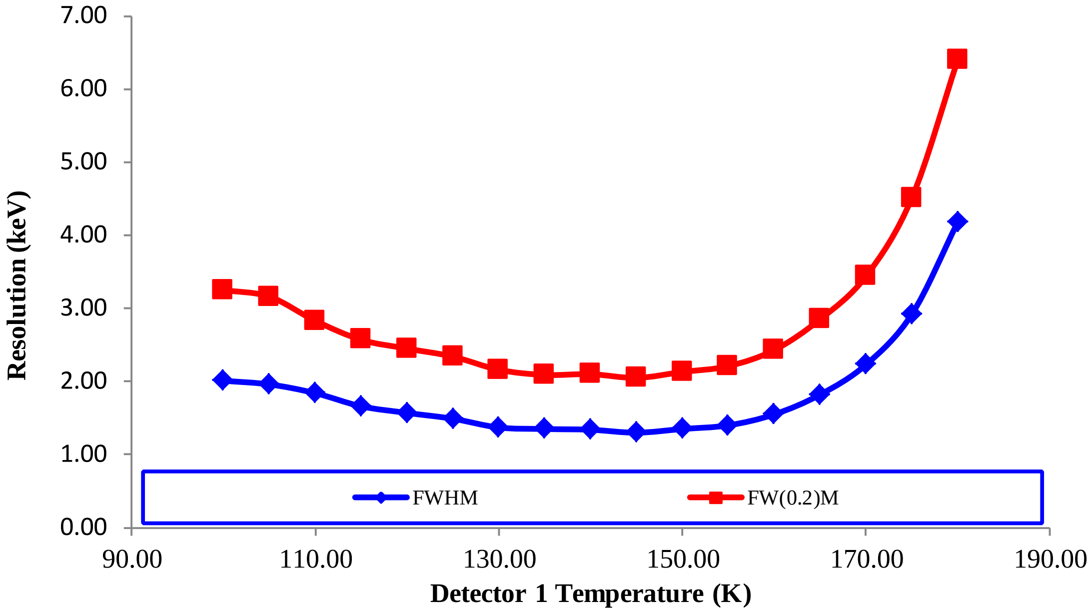

Figure 5.1: Energy resolution versus temperature for detector 1 at 122.1 keV.

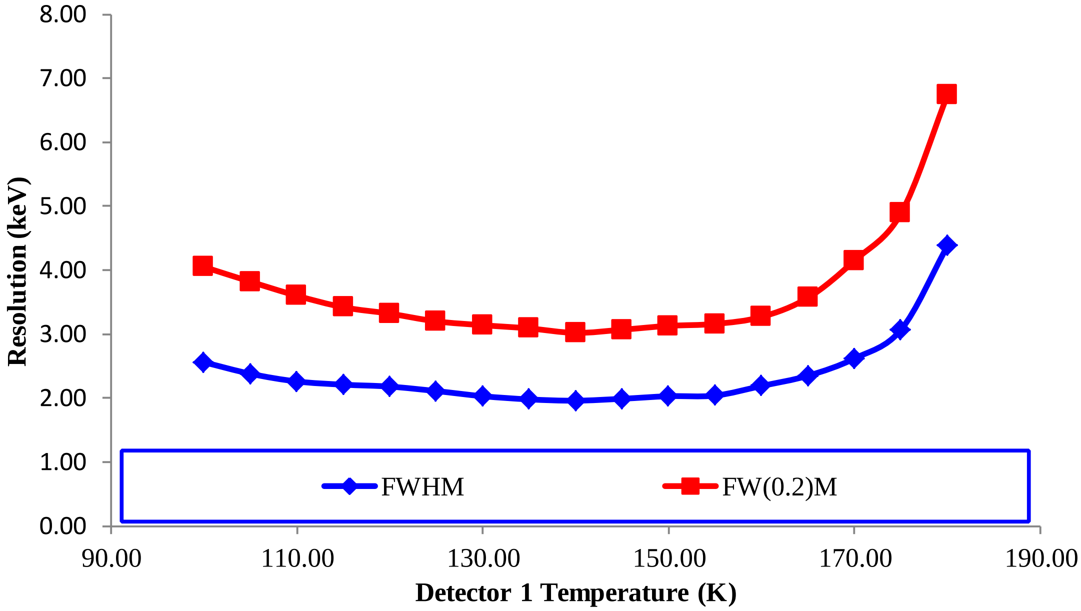

Figure 5.2: Energy resolution versus temperature for detector 1 at 1332.5 keV.

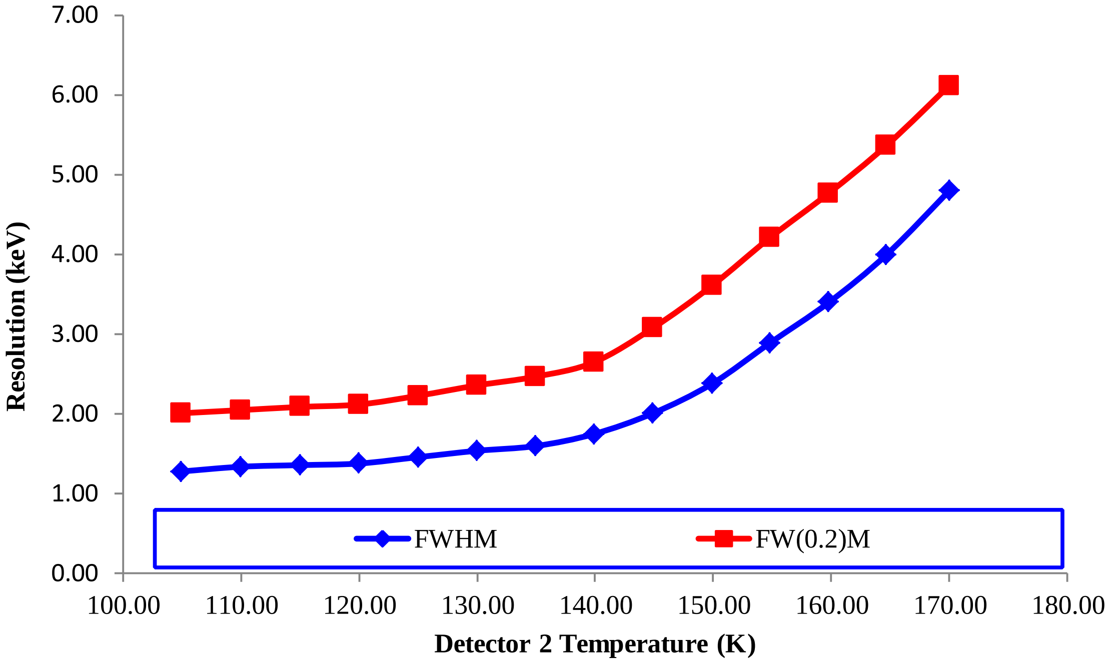

Figure 5.3: Energy resolution versus temperature for detector 2 at 122.1 keV.

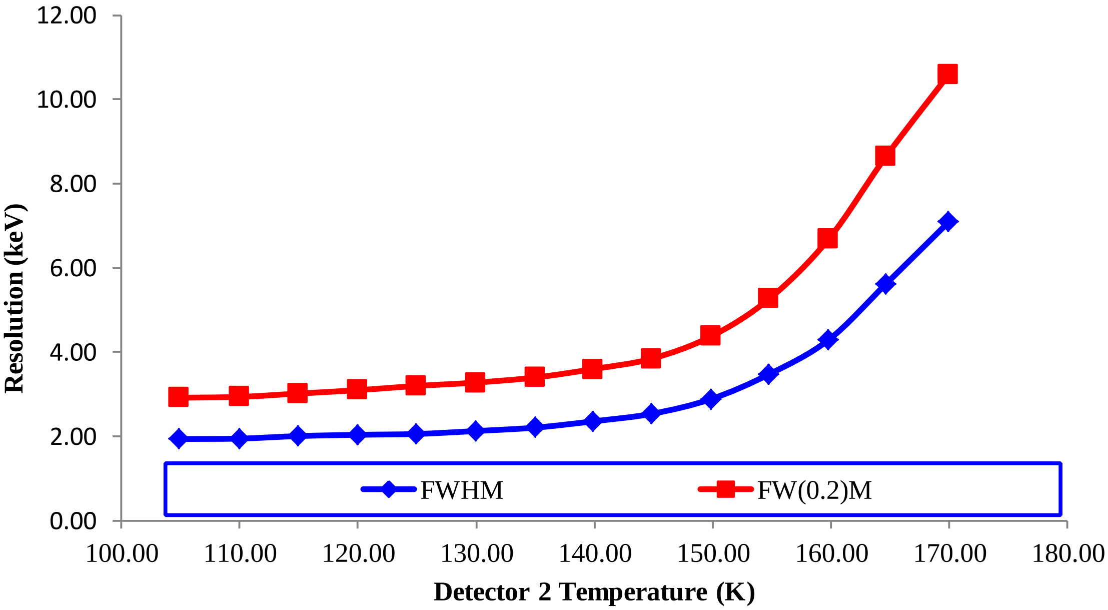

Figure 5.4: Energy resolution versus temperature for detector 2 at 1332.5 keV.

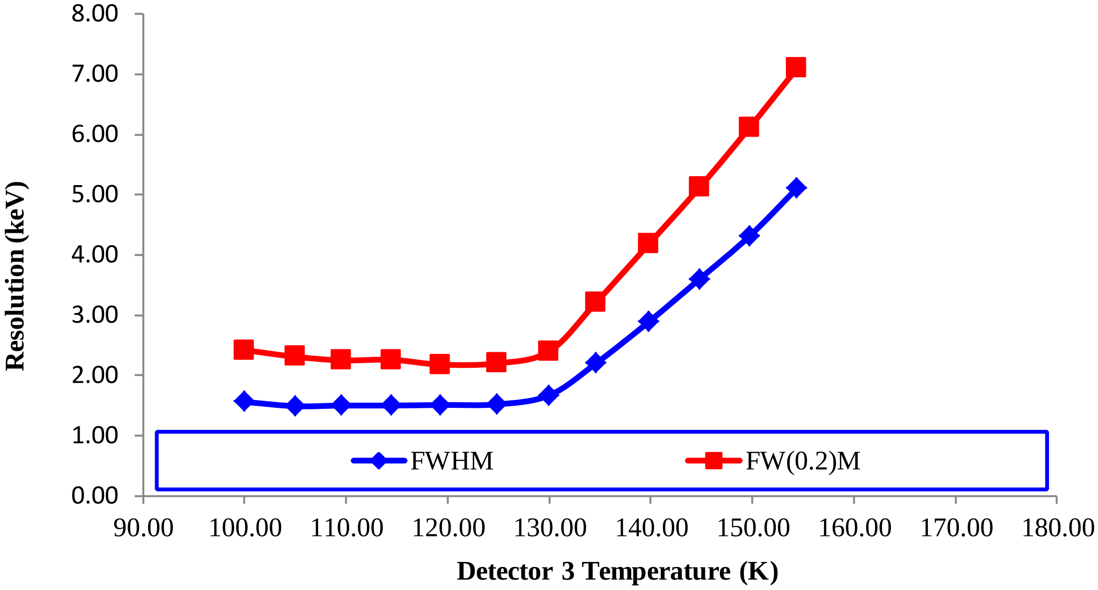

Figure 5.5: Energy resolution versus temperature for detector 3 at 122.1 keV.

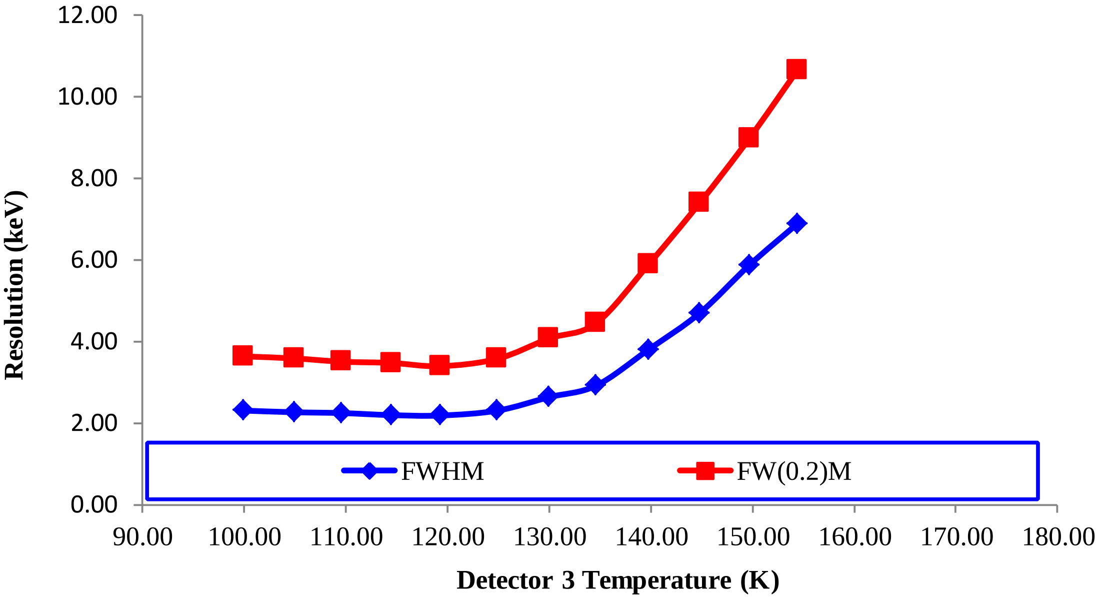

Figure 5.6: Energy resolution versus temperature for detector 3 at 1332.5 keV.

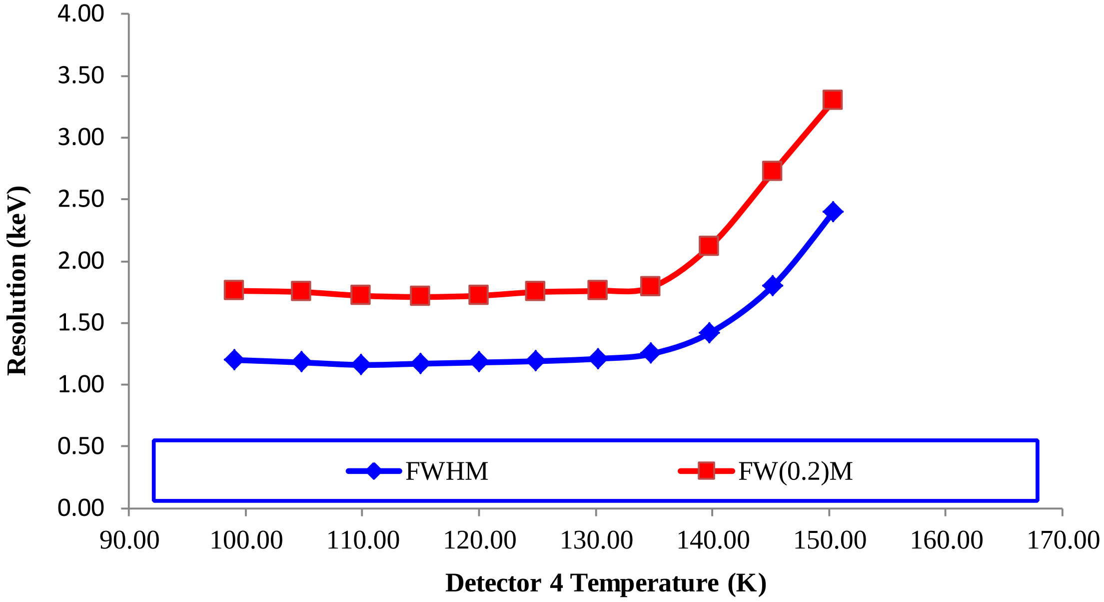

Figure 5.7: Energy resolution versus temperature for detector 4 at 122.1 keV.

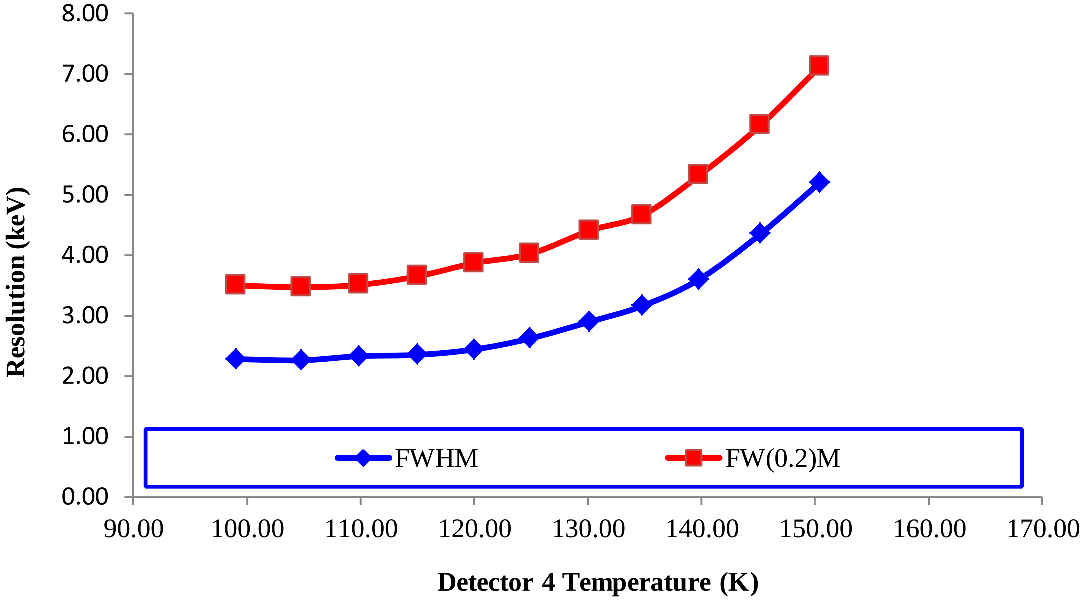

Figure 5.8: Energy resolution versus temperature for detector 4 at 1332.5 keV.

5.2. Detector Results with Cooler Switched Off

The results that have been shown at this point have focused solely on the energy resolution performance of each detector as a function of temperature. This section focuses on the energy resolution degradation resulting from the microphonic contribution of the Stirling cryocooler.

At this time the energy resolution results achieved with cooler on and cooler off will be presented on the same plot for each respective detector. Finally, a table containing the energy resolution values at each temperature has been included in the Appendix section of this dissertation.

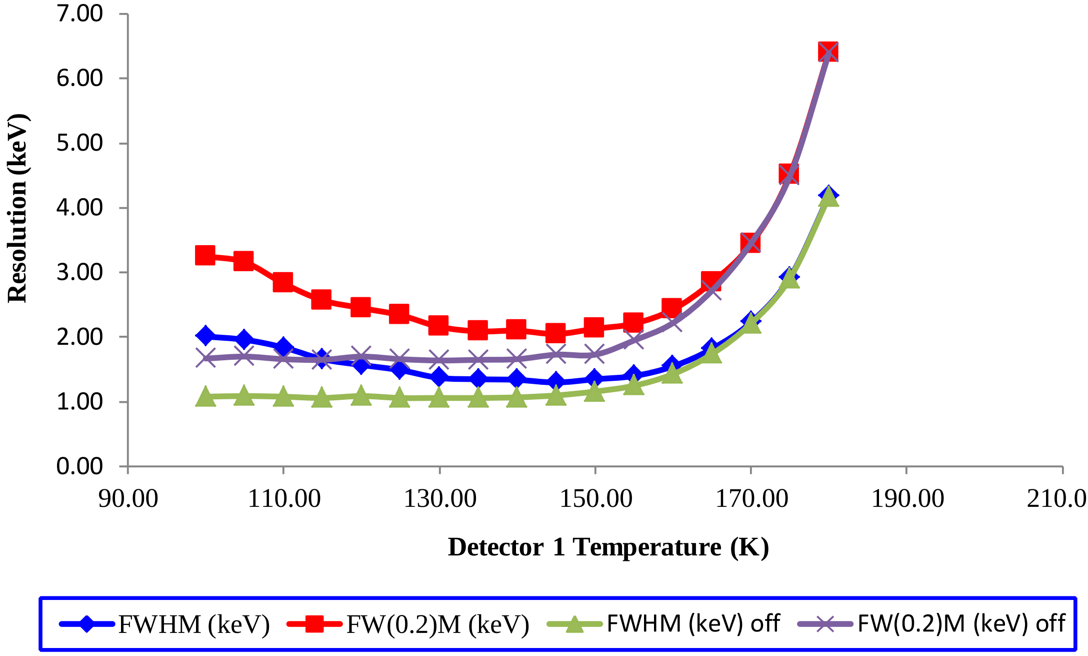

Figure 5.9: Full width half max and full width one-fifth max energy resolution at 122.1 keV for detector 1 with the cooler on and off.

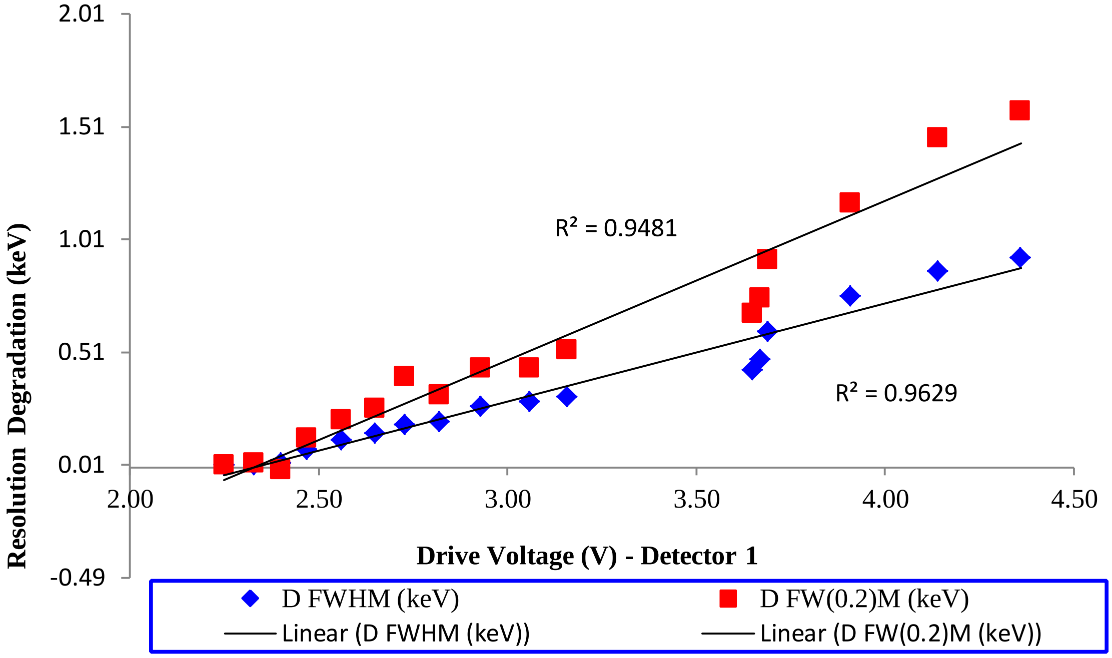

Figure 5.10: Energy resolution degradation at 122.1 keV plotted against drive voltage of the cryocooler (detector 1).

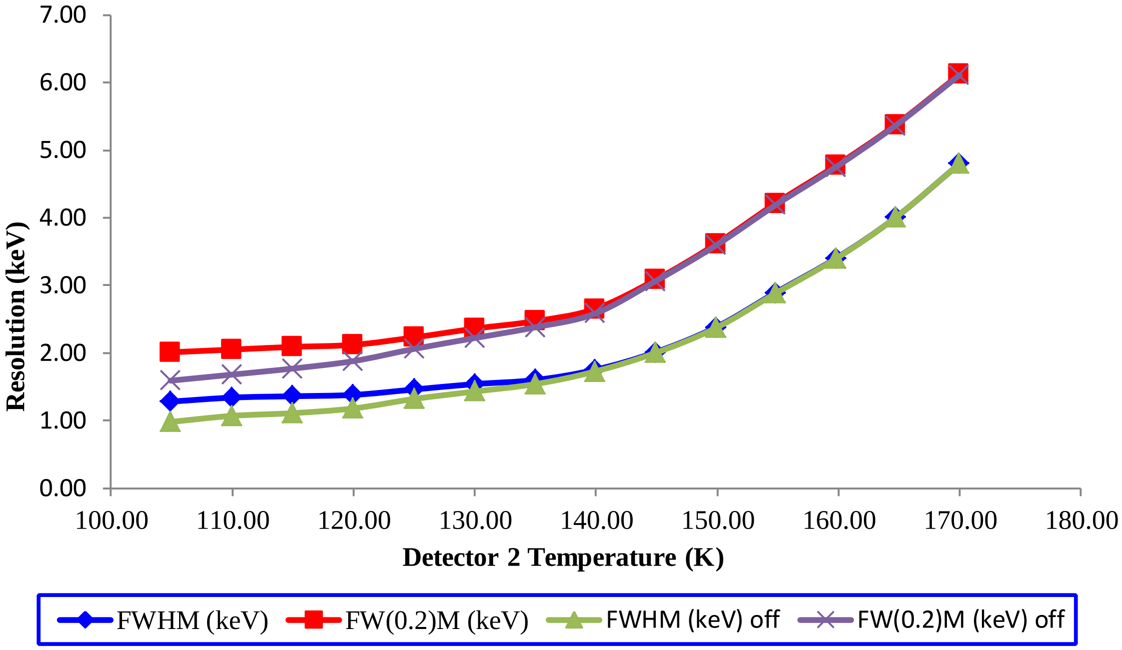

Figure 5.11: Full width half max and full width one-fifth max energy resolution for detector 2 at 122.1 keV with the cooler on and off.

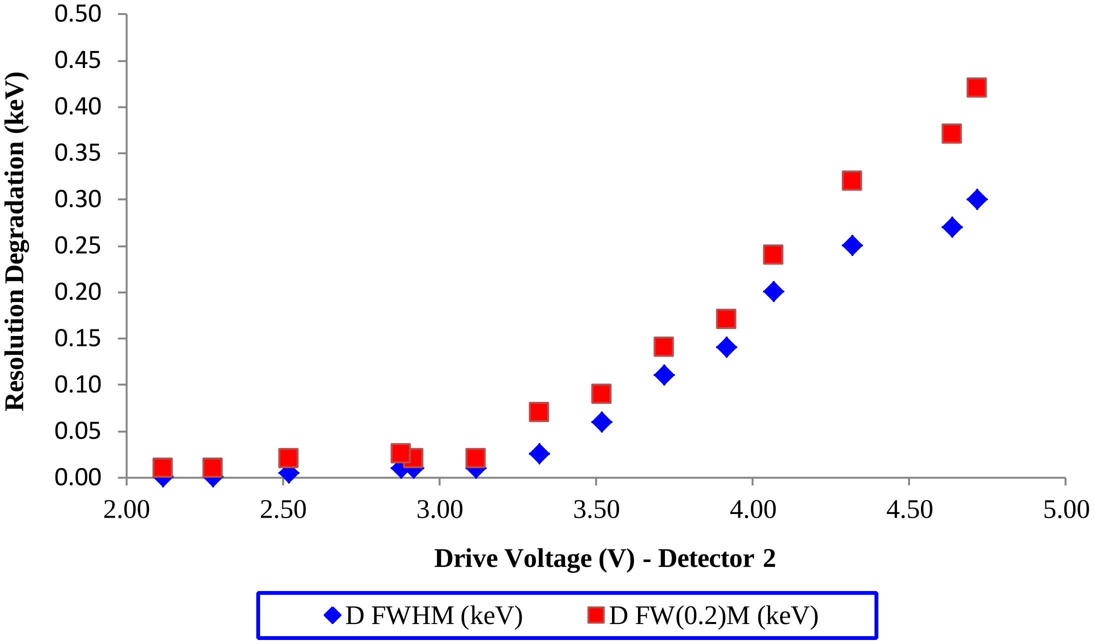

Figure 5.12: Energy resolution degradation at 122.1 keV plotted against drive voltage of the cryocooler (detector 2).

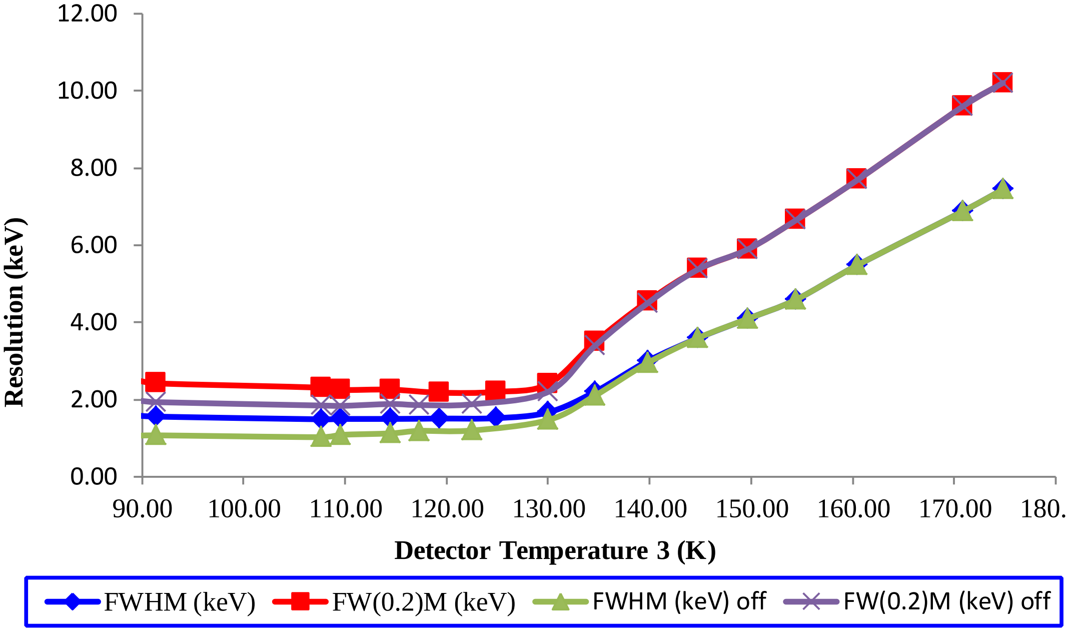

Figure 5.13: Full width half max and full width one-fifth max energy resolution at 122.1 keV for detector 3 with the cooler on and off.

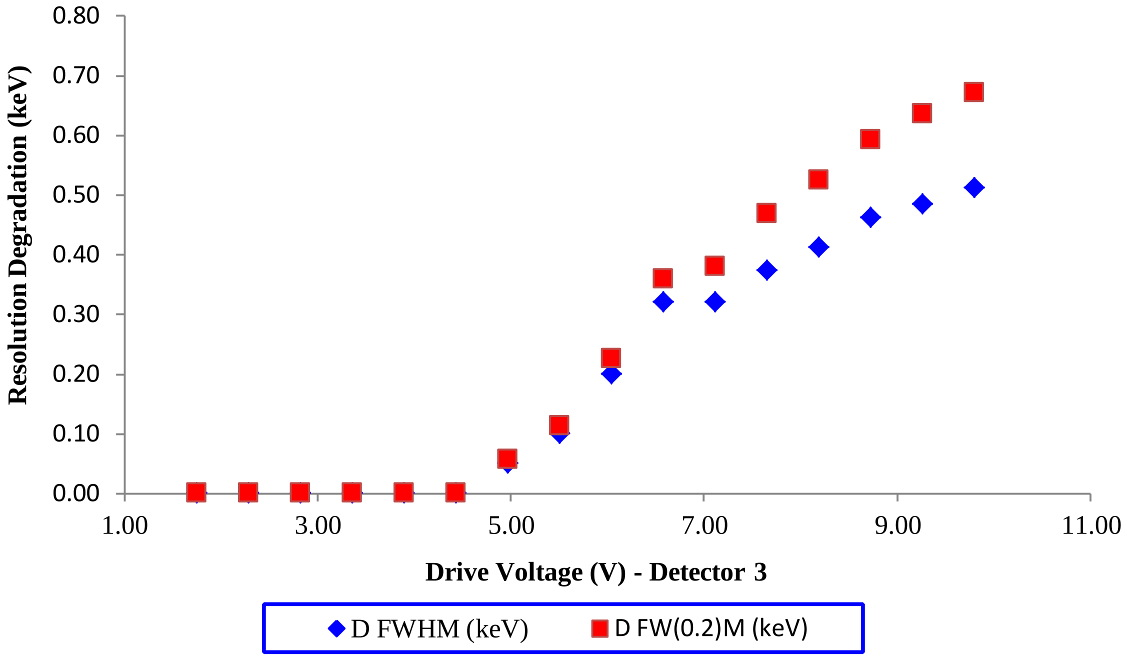

Figure 5.14: Energy resolution degradation at 122.1 keV plotted against drive voltage of the cryocooler (detector 3).

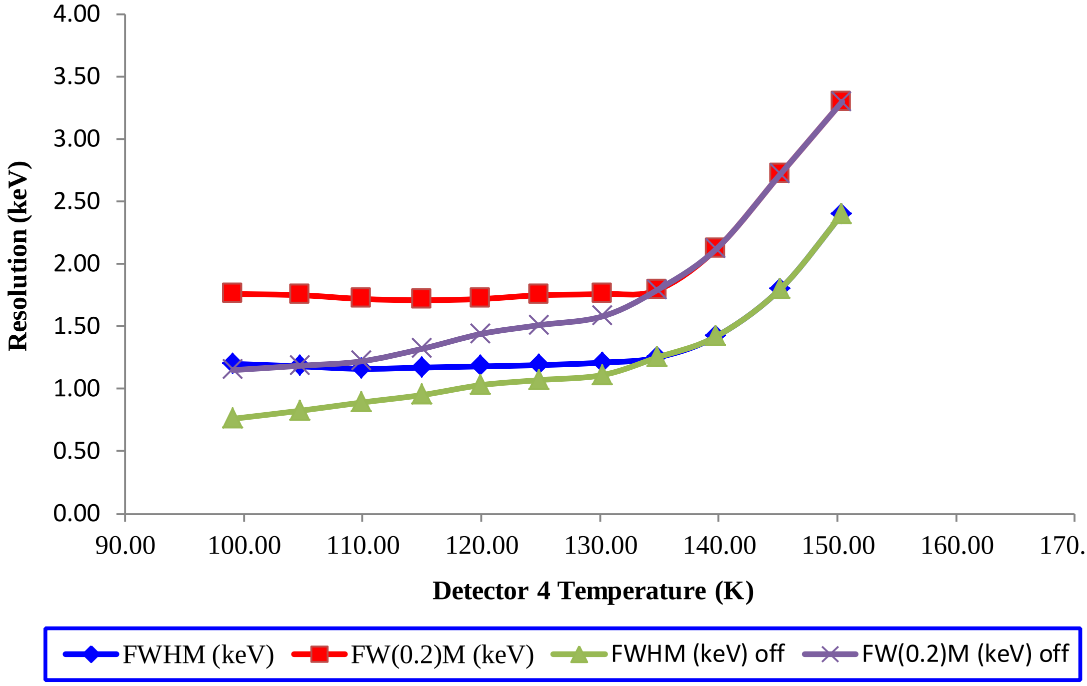

Figure 5.15: Full width half max and full width one-fifth max energy resolution at 122.1 keV for detector 4 with the cooler on and off.

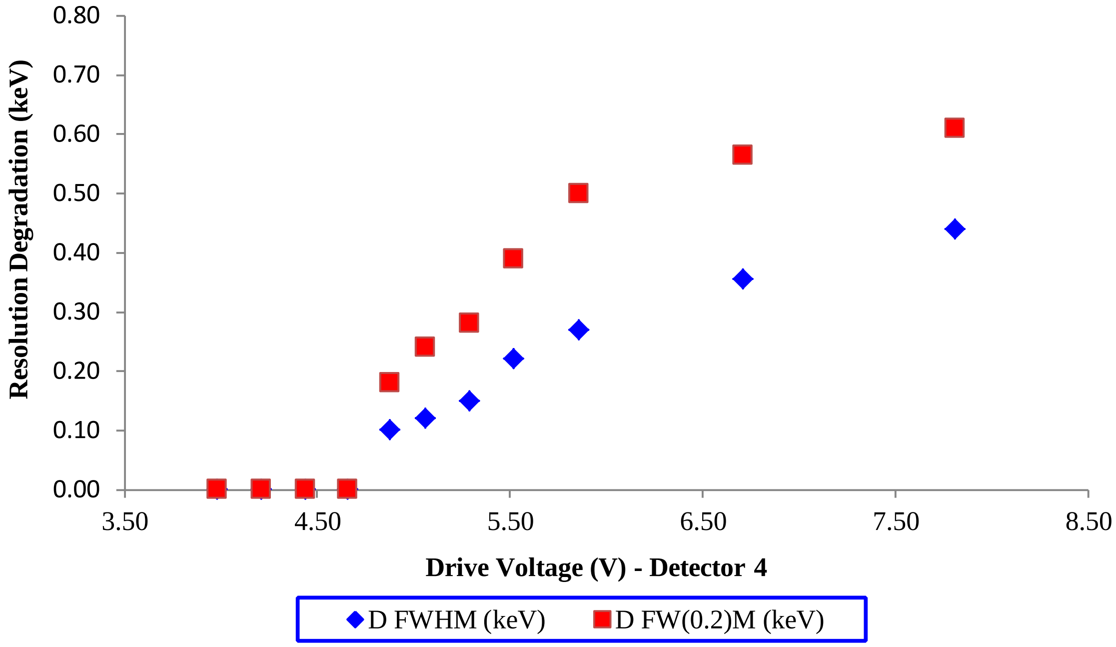

Figure 5.16: Energy resolution degradation at 122.1 keV plotted against drive voltage of the cryocooler (detector 4).

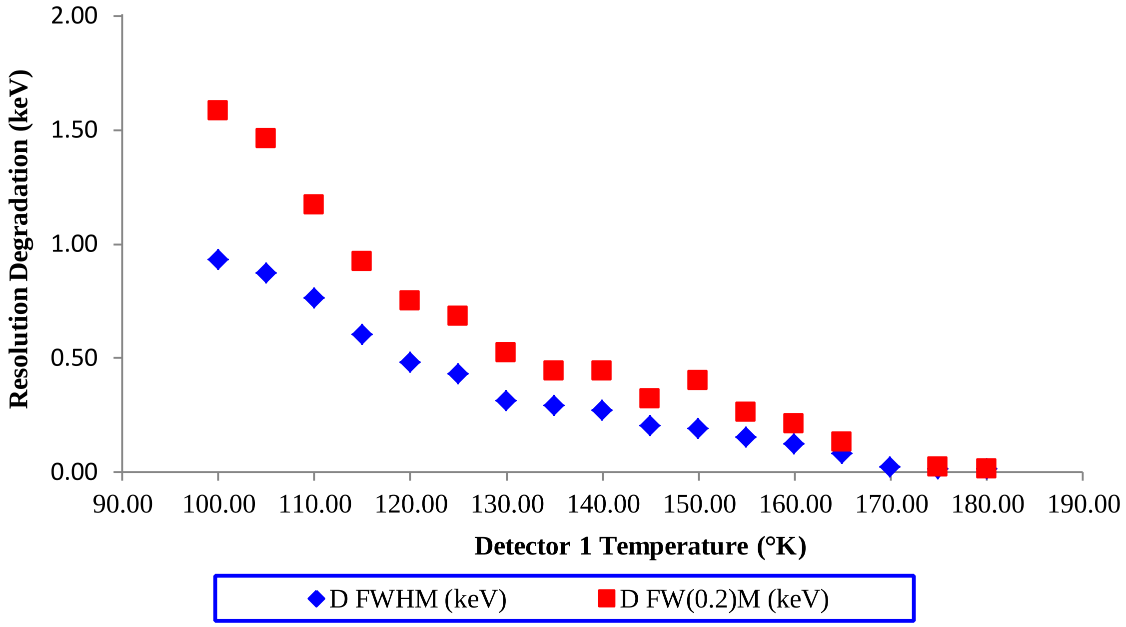

Figure 5.17: Energy resolution degradation at 122.1 keV plotted against detector temperature (°K) for detector 1.

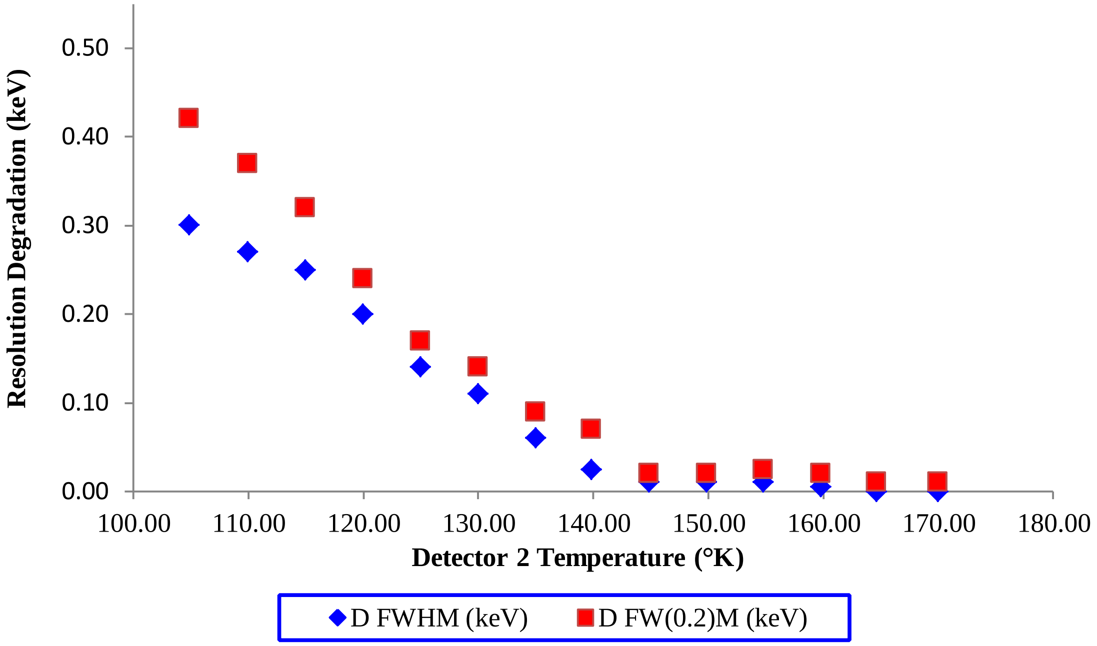

Figure 5.18: Energy resolution degradation at 122.1 keV plotted against detector temperature (°K) for detector 2.

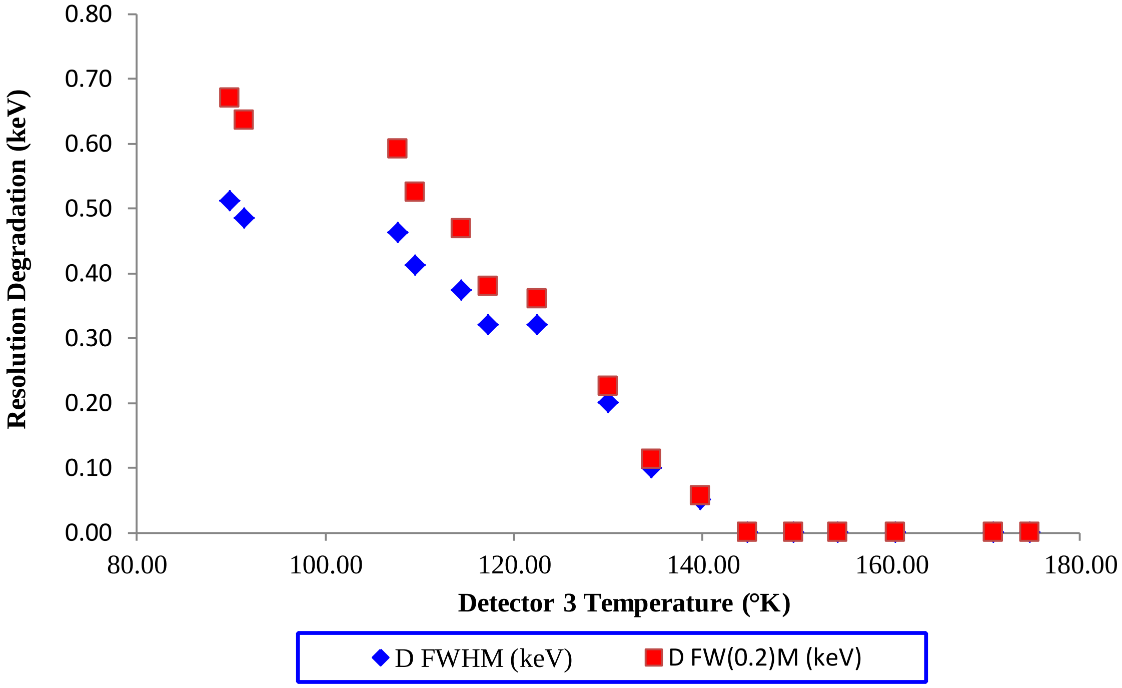

Figure 5.19: Energy resolution degradation at 122.1 keV plotted against detector temperature (°K) for detector 3.

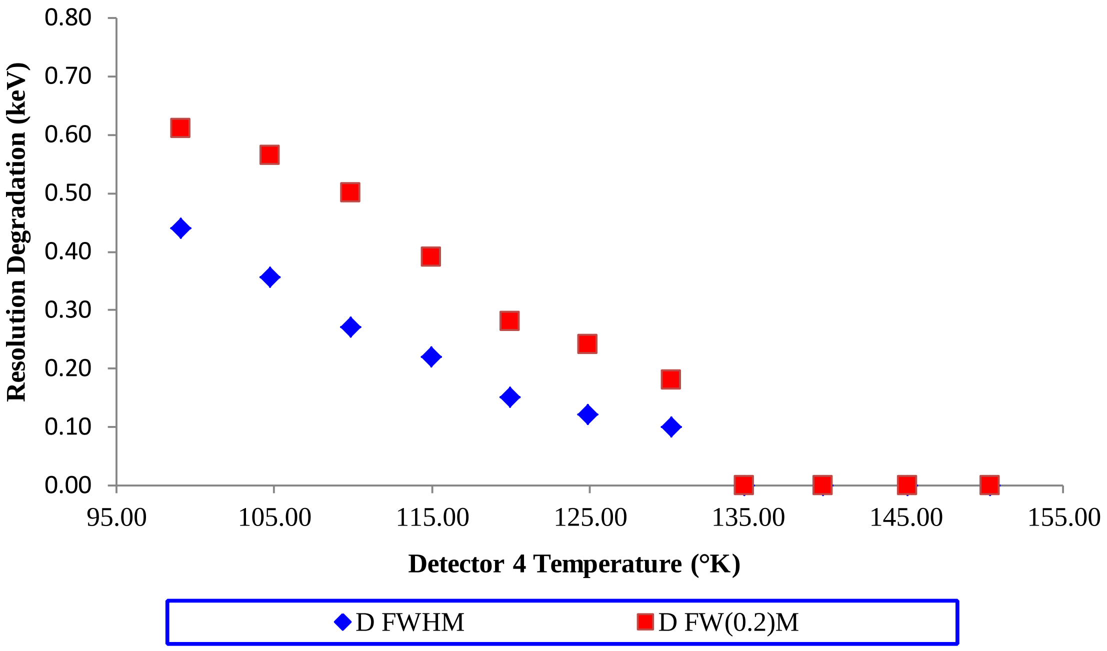

Figure 5.20: Energy resolution degradation at 122.1 keV plotted against detector temperature (°K) for detector 4.

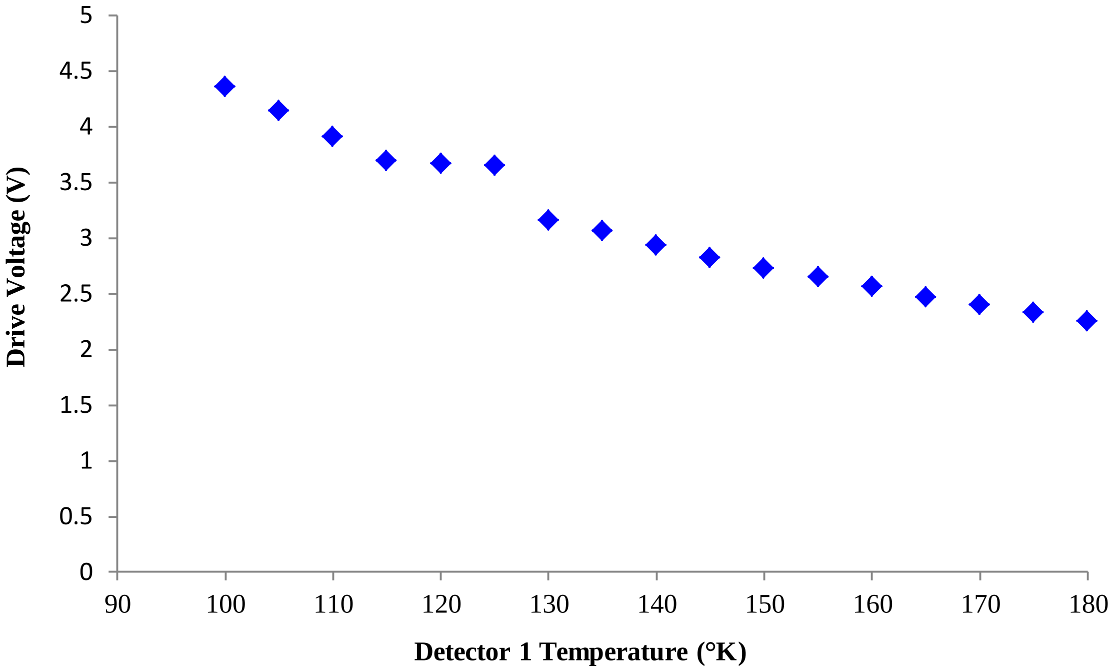

Figure 5.21: Cryocooler drive voltage (V) as a function of detector 1 temperature (°K).

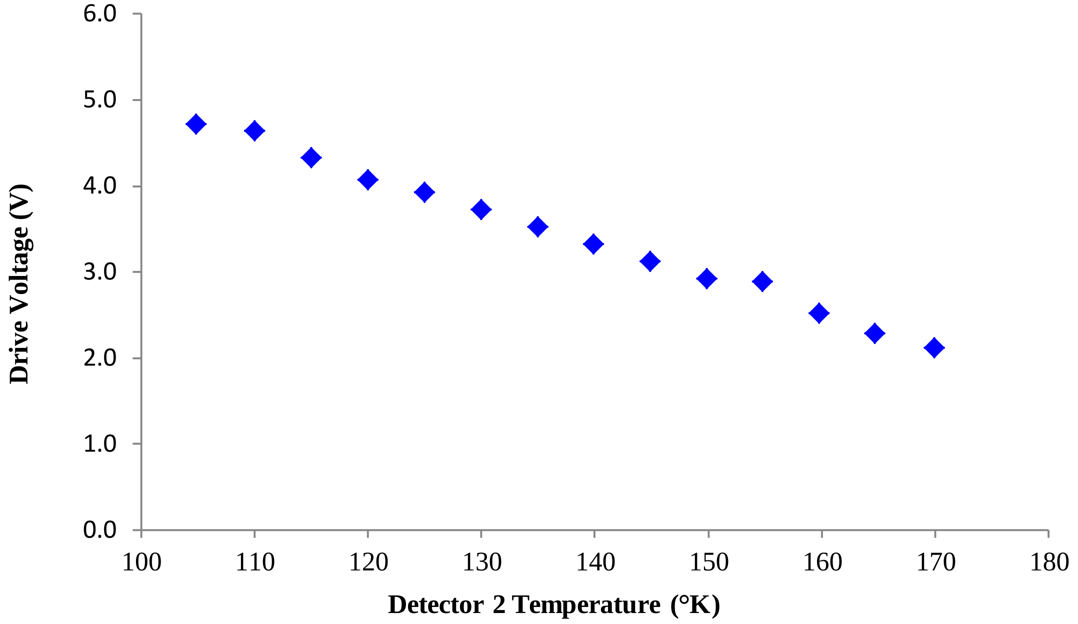

Figure 5.22: Cryocooler drive voltage (V) as a function of detector 2 temperature (°K).

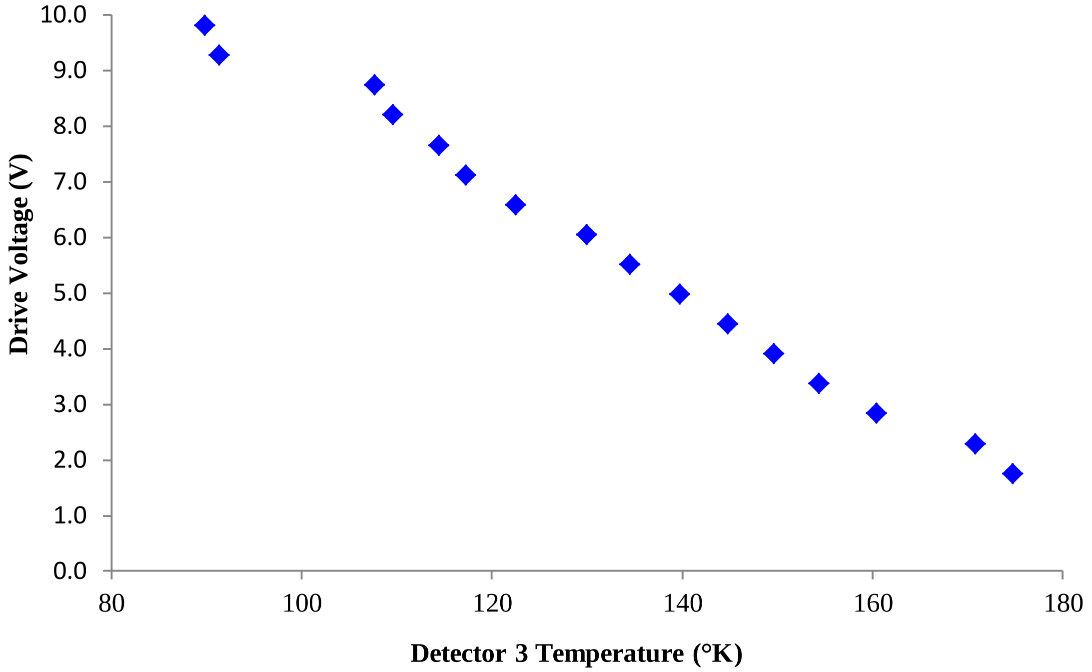

Figure 5.23: Cryocooler drive voltage (V) as a function of detector 3 temperature (°K).

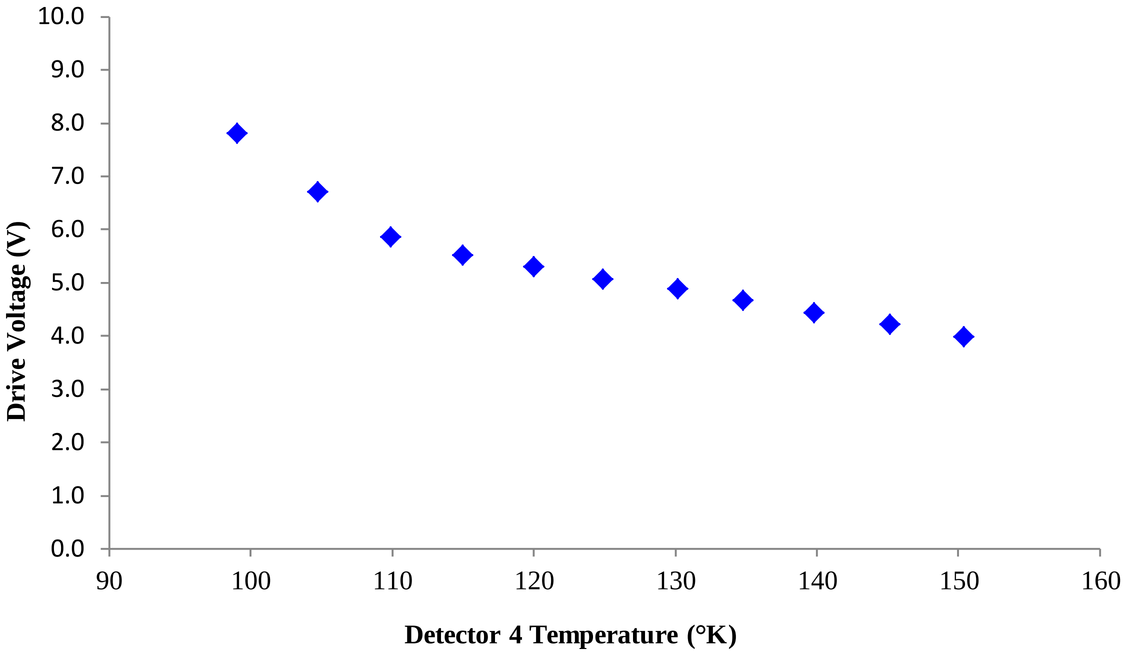

Figure 5.24: Cryocooler drive voltage (V) as a function of detector 4 temperature (°K).

5.3. Discussion

Two primary temperature dependent noise contributors became dominant as the detector temperature was increased beyond 130ºK. These contributors are charge trapping effects and internally generated detector noise. Charge trapping effects become dominant due to the fact that as temperature increases, carrier mobility decreases. Figures 2.24 and 2.25 provide an indication of carrier velocity as a function of temperature and voltage. From the aforementioned figures, it can be observed that the velocity decreases quickly as the temperature increases. It is important to note that charge trapping effects are different than trap-generated current flow, each of which represents a separate component of resolution degradation. As discussed in Section 2.6.2, the detector leakage current is made of various components including diffusion current, injected current, photon-generated current, breakdown current, and thermally generated current within the depletion region. Thermally generated current within the depletion region is caused by thermal ionization of electron-hole pairs in the bulk by direct transition (band-to-band) [22]. This particular form of bulk generated leakage current is of relevance due to its temperature dependence. It also becomes more pronounced with increased detector volumes. This was specifically pointed out and observed in the Nakano, Simpson, and Imhof research study of 1977, where 1) the ratios of the measured leakage current exceeded the ratio of their corresponding detector volumes and 2) varied with increasing temperature [79]. The effect of this leakage current increase and increased charge trapping effects with temperature is shown in Figure 5.21.

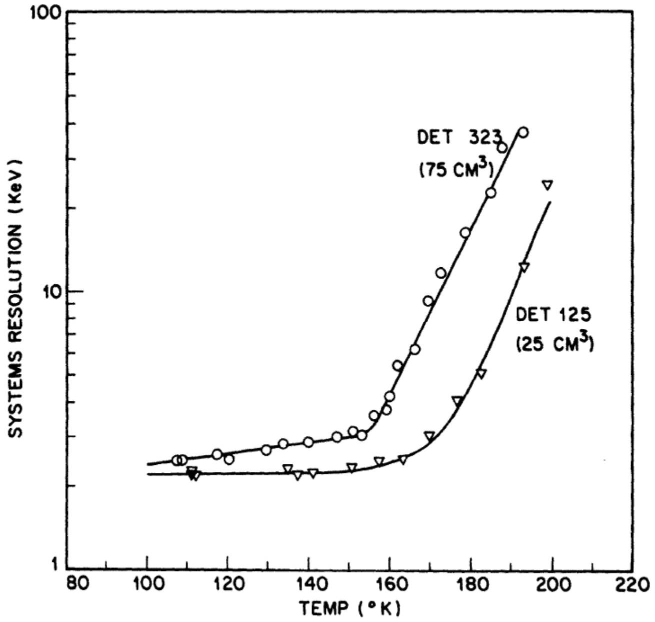

Figure 5.25: System resolution (keV) as a function of temperature obtained for the two detector systems reports in the Nakano, Simpson, and Imhof study of 1977 [79].

Subsequently, the same was observed in the measurements taken as a part of this research. This becomes most apparent when the energy resolution plots of detector 1 and detector 4 are compared. Detector 1 exhibits a fairly flat energy resolution curve up to about 150ºK prior to reaching the 'knee' of the curve, where significant degradation in energy resolution occurs. This same knee in detector 4 occurs at a much lower temperature, approximately 130ºK to 135ºK. This is due to the fact that the noise at high temperatures is dominated by leakage current and, based on prior research, becomes more prevalent as detector volume increases [79]. Accordingly, the larger detector exhibits increased degradation of energy resolution. This can be observed by plotting the approximate knee location versus the volume of the detector as shown in Figure 5.24. This relationship shows a strong linearity with a R^2 value of 0.9737.

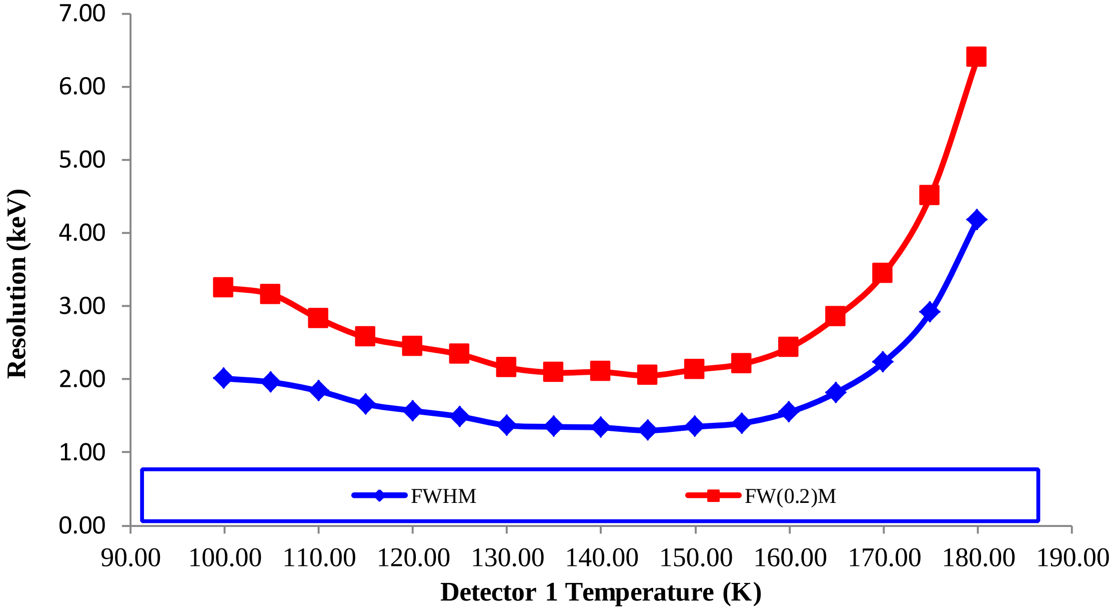

Figure 5.26: Energy resolution versus temperature for detector 1 at 122.1 keV.

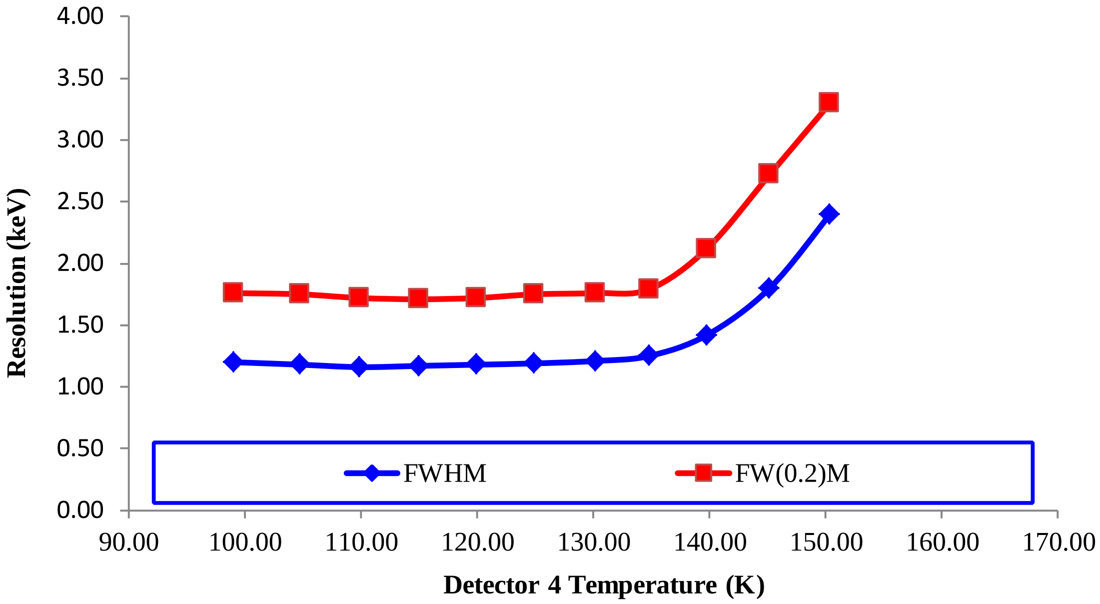

Figure 5.27: Energy resolution versus temperature for detector 4 at 122.1 keV.

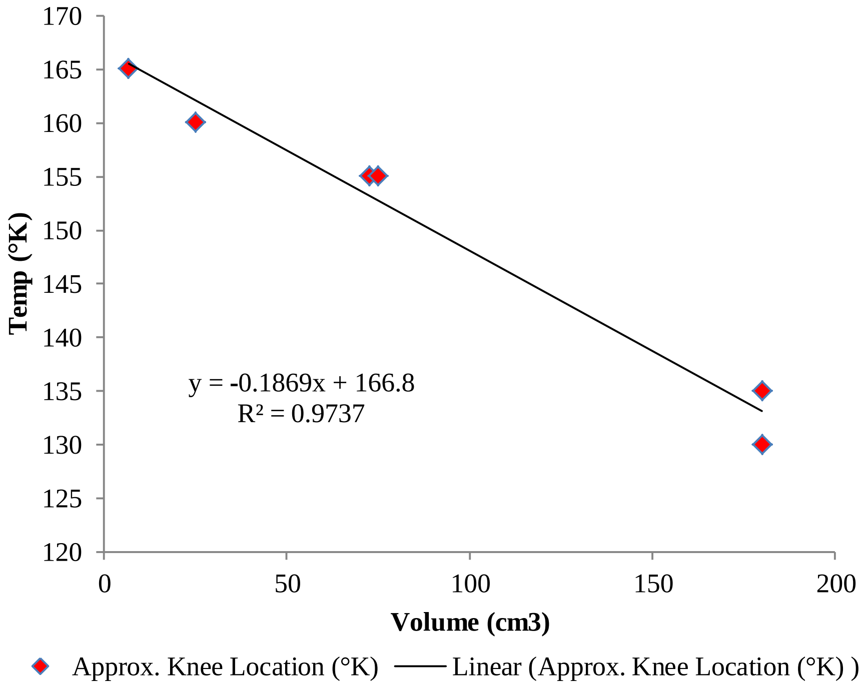

Figure 5.28: Approximate knee location for energy resolution at 122 keV for the four detectors used in this research as well as the two detectors used in in the Nakano, Simpson, and Imhof study of 1977 [79].

The energy resolution degradation at higher temperatures was dominated by leakage current. At lower temperatures (e.g., 130ºK), microphonic noise introduced through mechanical cooling of the detector system became more prominent. This is due to the fact that in order to achieve the cooler temperatures, the coolers tend to operate at a high percentage of maximum drive voltage. This results in a larger displacer travel and subsequently more mechanical vibration. As a result, the microphonic noise induced by the cooler tends to be largest at temperatures below 130ºK. By measuring the energy resolution of the detector assemblies with the cooler enabled and then again with the cooler disabled, this research has quantified the microphonic contribution on energy resolution in a new mechanically cooled HPGe detector design. This energy resolution degradation was most pronounced at very low temperatures (<110ºK) and has been shown to be a function of cooler drive voltage. This research shows that with the direct coupled design and with the smallest detector (detector 1) the energy resolution degradation observed can be as much as 1.5 keV at 122 keV. Despite the significant degradation observed at max drive voltage, the direct coupled design developed as a part of this dissertation was able to achieve a minimum value of resolution of 1.30 keV (i.e., highest energy resolution) at 122.1 keV. This was observed in detector 1. This compares well with historical first-revision designs. An example of this is a 50mm x 30mm Stirling cooler cooled design that showed a 2.1 keV energy resolution at 1332 keV in its first revisions [48]. Current state of the art HPGe handheld devices have improved on this result achieving as low as 1.0 keV FWHM at 122 keV. These results are shown again in figures 5.25 & 5.26.

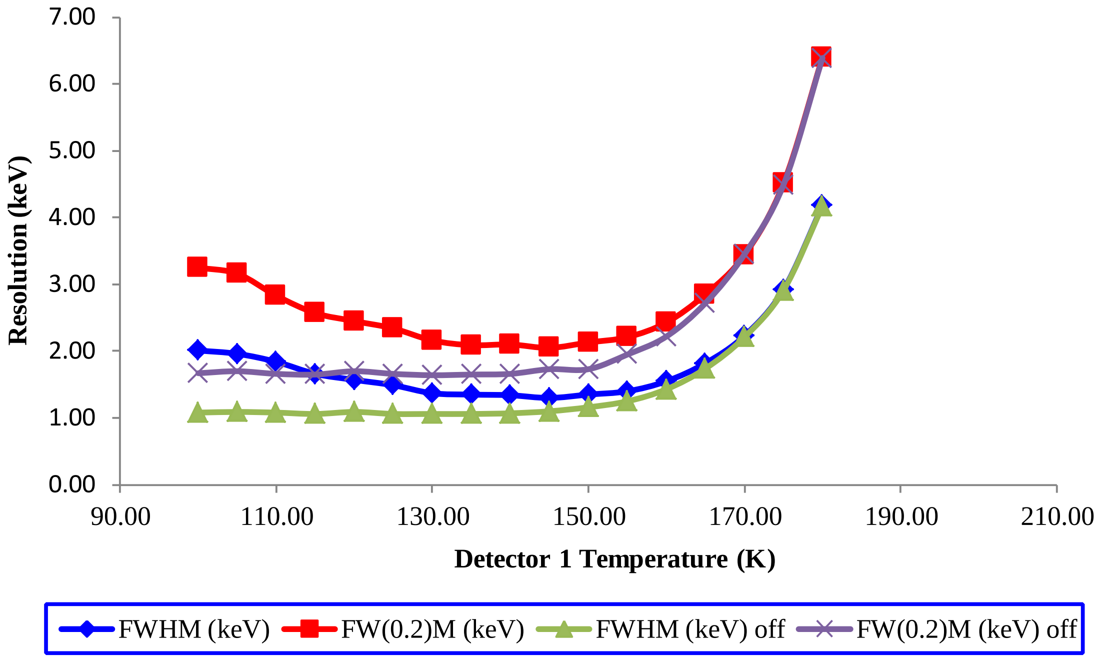

Figure 5.29: Energy resolution versus temperature for detector 1 at 122.1 keV provided with cooler on and cooler off.

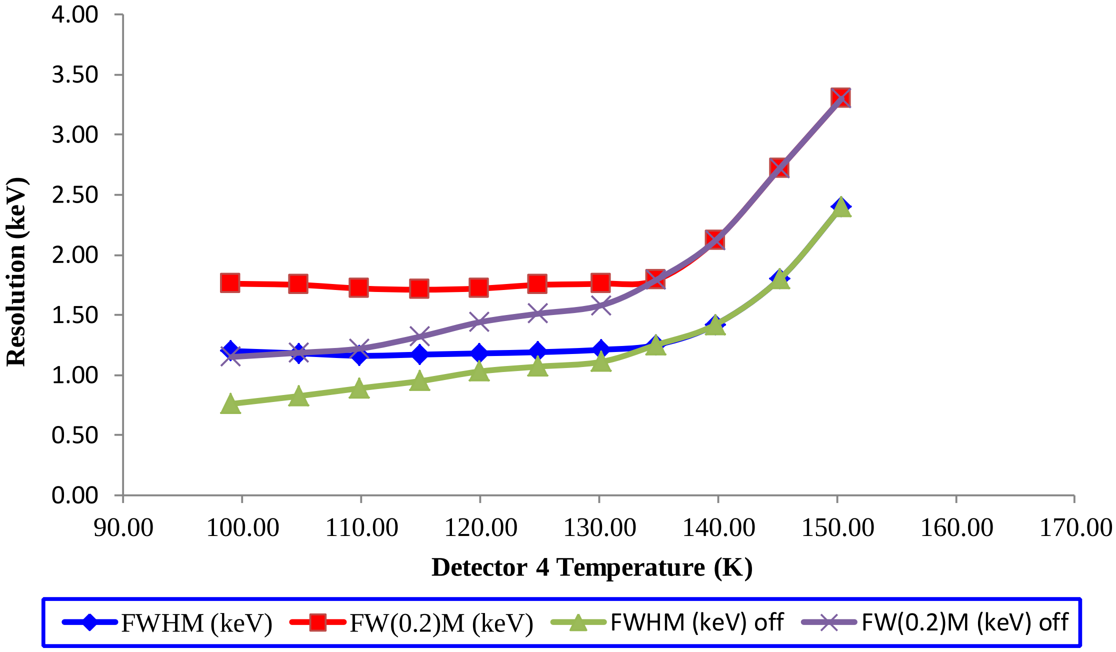

Figure 5.30: Energy resolution versus temperature for detector 4 at 122.1 keV provided with cooler on and cooler off.

It can be clearly observed that the microphonic induced energy resolution degradation is most prevalent at the lower temperatures. This is a direct result of the percentage of max capacity at which the cooler is required to work as a function of temperature in order to maintain detector temperature. To demonstrate this point, the difference in the energy resolution versus the cooler drive voltage has been plotted for all detectors in Chapter 5.2. In each case, the difference in energy resolution for the system degrades in a monotonically increasing fashion with the drive voltage of the cryocooler. This is due to the fact that as the drive voltage increases, the distance traveled by the displacer increases, resulting in increased microphonic noise [80].

As a means of further analyzing the cooler's contribution to the performance of each detector system, a series of additional plots has been provided. These additional plots include plots for energy resolution degradation as a function of temperature (included in figures 5.17 through 5.20) and plots for drive voltage as a function of temperature (included in figures 5.21 through 5.24). The energy resolution degradation decreases in a linear manner as the temperature is increased. This can be observed in figures 5.17 through 5.20. For each cooler assembly, the maximum degradation of energy resolution occurs at the lowest temperatures (<110°K) and reduces in a linear fashion to approximately 140°K where the degradation is negligible. In the case of the detector 1 assembly the degradation did not approach zero contribution until approximately 160°K. It is believed that this effect is due to the smaller mass of detector 1. In order to understand this further, the drive voltage as a function of temperature has also been plotted. This has been done in figures 5.21 through 5.24. It can be clearly observed that drive voltage shows a linear relationship with the temperature of the detector assembly. This was the case in all detector assemblies, and it is the expected result. In a similar relationship to what was observed in the figures showing the energy resolution versus temperature, the drive voltage is highest at the point of coldest detector temperatures (<110°K). This is reasonable intuitively, as the cooler is closest to its maximum capacity at this point.

Chapter 6

Conclusions and Outlook

6.1. Summary of Work Performed

This research investigates four different, split-Stirling cooled, high purity germanium detector assemblies with detectors of varying geometry (diameter and length). All detectors used were coaxial, bulletized, high purity germanium detectors. Each detector assembly was evaluated for system resolution performance as a function of temperature. All testing was started at 100^{o}K (detector temperature) and progressively increased by 5^{o}K increments until the detector assembly resolution was observed to exhibit exponential increase. The term ‘detector assembly resolution’ is used due to the fact that noise contributions can originate in the detector as well as other components within the system. This becomes especially true for this particular area of research: mechanical cooler systems.

The primary differentiation between this research and that of the Nakano, Simpson, and Imhof study of 1977 is that this research is conducted with larger detectors that were mechanically cooled instead of cooled with liquid nitrogen. The largest detector used in the Nakano, Simpson, and Imhof study of 1977 was 75 cm^3; this research extends to detectors up to 180 cm^3. In field applications that require hand-held detectors, the use of liquid nitrogen for long periods of time is impractical, especially considering the remote locations where some detection measurements may be made. The consequence of using mechanical cooling in place of the more traditionally used liquid nitrogen is the introduction of an additional (and significant) generation of noise: microphonics.

6.2. Conclusions

This research is framed around the desire to extend the prior research in two separate regards. The first is to extend the energy-resolution versus temperature research into larger detector volumes up to 180 cm^3. The second area where this research has expanded on the prior research is with the introduction of a new mechanical cooling design that may lead to lower mass HPGe spectrometers. Due to the moving parts within a split Stirling cryocooler [71], an additional component of noise (and associated energy resolution degradation) is introduced into the system.

This research placed particular emphasis on measurements of the energy resolution of each detector in contrast to prior studies of temperature dependence of various solid-state effects including IV response curves. Accordingly, all measurements were conducted at relatively high bias voltages and have been presented in terms of observed energy resolution as a function of temperature. Consistent with prior research, good spectroscopic performance of large coaxial high purity germanium detectors at elevated temperatures has been demonstrated. Furthermore, each new detector design demonstrated the feasibility of operating with good resolution of about 2 keV or better at 122.1 keV up to at least 130ºK. This operating temperature is higher than current commercially available mechanically-cooled detector systems which operate between 100°K and 120°K.

Detector noise is shown to become more significant in these split-Stirling detectors as the detector temperature is increased beyond 130ºK. This noise contributions include charge trapping effects and internally generated detector leakage current, each of which contribute to the overall degradation of the system energy resolution as the temperature of the system is increased.

An additional source of noise in mechanically cooled detector systems has also been considered as a part of this research. This noise contribution is from cooler generated microphonics which tends to be the dominant noise source that degrades energy resolution more noticeably at temperatures below 130ºK. By measuring the energy resolution of the detector assemblies with the cooler enabled and then again immediately with the cooler disabled, this research was successful at quantifying precisely how the energy resolution is affected by the microphonic noise created by the split-Stirling cryocooler. The contribution may be as large as 1.5 keV @ 122keV. The complete range of microphonic contribution to energy resolution for each detector is reported in tables A5 though A8 in the Appendix. It can be clearly observed that the microphonic induced energy resolution degradation is most prevalent at the lower operating temperatures, and its relative contribution becomes insignificant at higher temperatures. This is a result of the percentage of max capacity at which the cooler is required to work in order to maintain the detector temperature. In each case, the energy resolution for the system was shown to degrade as the drive voltage of the cryocooler increases. Typical liquid nitrogen cooled detectors ranging in size from 10% to 150% detectors will cool down sufficiently within 2-6 hours of filling [74]. The cool down time as shown in this research ranges from 45 min on the smallest detector (detector 1), approximately 4 hours on detector 2 and approximately six hours on the largest detectors (detectors 3 and 4). Faster cool down times can be achieved by increasing the size (capacity) the cooler. Much larger coolers are commercially available. Subsequently, increasing the size of the cooler also adversely affects the overall mass of the device. The cooler used for this research was selected to provide an acceptable cool-down time (<6 hours for the largest detectors) at as low as possible overall mass. On a final note, mechanical cooling is rarely faster than LN_2 at achieving cool down times due to the much large cooling capacity present in a LN_2 filled dewar.

Further analysis of the cryocooler was able to show clear relationships between the drive voltages of the cooler and the temperatures of the detector assemblies. Related to this, is the relationship of energy resolution degradation as a function of temperature. In figures 5.21 through 5.24 if can be clearly observed that the drive voltage of the cryocooler is at a maximum as the point of lowest detector temperature (<110°K). Intuitively this is a reasonable observation. In order to achieve this level of cooling, the cooler is required to work at a level closest to its maximum capacity. This is observed as a higher drive voltage. This higher drive voltage decreases linearly as the temperature of the detector assembly is increased. As the drive voltage is decreased (decreasing the temperature of the detector assembly) the travel of the piston/displacer decreases proportionately leading to a reduced microphonic contribution. This relationship is clearly observed in figures 5-17 through 5.20. The energy resolution degradation for each detector assembly decreases as a linear function of detector temperature.

This research, coupled with prior research studies, provide the basis for designing potentially lower mass, hand-held, mechanically cooled HPGe detectors with large crystals that operate at higher temperatures than liquid nitrogen cooled (and current mechanically-cooled) systems. Operating a mechanically cooled detector system between 130ºK and 150ºK allows for minimization of the required cooler size (weight and geometry). As commercially available cooling devices advance and cooling density continues to improve, radiation detection serves to directly benefit. It is suggested here that the key to future compact RIID development involves a balance of elevating the detector temperature past the point where microphonic noise is the dominant contributor but simultaneously not past the point where energy resolution ultimately degrades at an exponential rate due to excessive leakage current. In the case of the detectors tested as a part of this research, the microphonic noise resulting from the cooler was reduced to a fraction of its maximum contribution by time a temperature of 120°K was reached. In addition, the energy resolution knee did not introduce itself until after 130°K, and its location was shown to depend on the volume of the detector (see Figure 5.20). This result could be used to predict desired maximum operating temperatures for split-Stirling based HPGe detectors with volumes extending up toward 400 cm^3 (although such large detector sizes are not appropriate for one man portable, handheld devices).

Operating a mechanically cooled detector system between 130ºK and 150ºK allows for smaller cooler options in hand held HPGe applications. The key to this future RIID development becomes a balance of elevating the detector temperature past the point where microphonic noise is the dominant contributor but simultaneously not past the point where leakage current becomes dominant and energy resolution ultimately degrades at an exponential rate. As shown in this research and prior research, this dominant leakage current varies with multiple variables. Minimizing the impact of leakage current should be considered in any detector assembly design.

6.3. Recommendations for Future Research

One particular area that has been identified as an opportunity for future research is further characterization of the microphonic contribution of the cryocooler. This research presented the results that quantified the impact of the cryocooler in terms of energy resolution degradation as a function of drive voltage for a single split Stirling cryocooler design. Additional studies are recommended as means of further understanding the impact of the harmonic microphonics on the detector performance.

For example, a study focusing on the characterization of different lift capacity split Stirling cryocoolers could be performed. As the heat load on the cryostat is reduced through continued development efforts, the capacity of the cooling (and, subsequently, the size of the cooler) required may also be reduced. This research presented energy resolution performance impact for a single cryocooler design. Each new detector/cooler design configuration will require independent evaluation to determine performance impact. In a similar manner, detectors larger than those tested as a part of this research will require larger cryocoolers with additional capacity. Similar characterization studies to understand performance impacts should also be conducted.

This research focused on split Stirling cryocoolers; however, there are alternative cooling technologies that are also suitable for use with HPGe detectors which could also be investigated as alternatives. A pulse tube cooler represents one such technology that could be further investigated. A unique feature of the pulse tube technology is the absence of cold moving parts. This innovation reduces the generated noise and vibration as compared to a split-Stirling cooler [83]. Advances in Joule–Thompson technology have also been shown to be effective in HPGe detector applications [84]. Each cooling technology can impact the resolution performance of the system differently [83].

Moreover, direct vibration measurement is recommended to quantify the microphonic contribution of each cooler design. This direct measurement approach could be achieved by fixing a vibration transducer onto a dummy detector of approximately the same mass. Suggested materials that could be used in place of an HPGe detector are brass or copper, each of which has comparable densities to that of germanium. Using materials that have approximately the same density as high purity germanium would provide a representation of the mass impact of the detector on the overall vibration of the design. These vibration measurements could then be compared against the energy resolution of the detector to fully characterize their impact.

Section 3.1.2 focused on the mechanical vibrations induced by the Stirling cooler. Specifically, inside the cold finger, a resonating mass made up from the piston and displacer form a single degree of freedom vibratory system which acts as a function of the mass flow of the working fluid. This reciprocating motion of the piston and displacer and the associated momentum imbalance manifests itself as the measured energy resolution degradation. Because the momentum imbalance remains constant for a cryocooler at a given drive voltage, the mass of the detector is believed to directly affect the level of microphonics observed. As the mass of the detector is increased and the force induced by the piston/displacer remains constant, the likely result is a reduced microphonic impact on the energy resolution of the system. This is heavily dependent on the detector design configuration. This provides an opportunity for continued research.

Another plausible technique that can be used to reduce the overall microphonic noise contribution to the detector energy resolution is oversizing of the cooler. This research was effective at demonstrating that the energy resolution degradation is a function of the drive voltage of the cooler. Oversizing of the cooler allows for the drive voltage at operational temperatures to be reduced. A larger cooler, however, would come at the expense of additional mass. This proposed technique would need to be verified through additional testing and provides an additional opportunity for continued research.

Bibliography

[1] *U.S. Nuclear Weapons Complex Homeland Security Opportunities.* Washington, D.C.: Project on Government Oversight, 2005. Print.

[2] *Radioisotope Identification of Shielded and Masked SNM RDD Materials*. Washington, D.C.: United States. Dept. of Defense;, 2010. Print.

[3] Sutcliffe, W.G., "Warheads and fissile materials: declarations and counting," *Nuclear Science Symposium and Medical Imaging Conference, 1991., Conference Record of the 1991 IEEE* , vol., no., pp.16,23 vol.1, 2-9 Nov. 1991.

[4] Moss, C.E.; Byrd, R.C.; Feldman, W.C.; Auchampaugh, G.F.; Estes, G.P.; Ewing, R.I.; Marlow, K.W., *Detection of uranium-based nuclear weapons using neutron-induced fission*, Nuclear Science Symposium and Medical Imaging Conference, 1991., Conference Record of the 1991 IEEE , vol., no., pp.1218,1221 vol.2, 2-9 Nov. 1991.

[5] *Disposal of Surplus Weapons Grade Plutonium*. Washington, D.C.: United States. Dept. of Energy; 2000. Print.

[6] *Low-resolution Gamma-ray Measurements of Uranium Enrichment*. Washington, D.C.: United States. Dept. of Energy;, 1996. Print.

[7] Boardman, D.; Flynn, A., *Performance of a Fisher Linear Discriminant Analysis Gamma-Ray Identification Algorithm*, Nuclear Science, IEEE Transactions on , vol.60, no.2, pp.482,489, April 2013.

[8] *Advanced Infrared Detectors and Systems: International Conference, 29-30 October, 1981, London.* London: Institution of Electrical Engineers, 1981. Print.

[9] Martyniuk, P., "HOT HgCdTe infrared detectors," *Numerical Simulation of Optoelectronic Devices (NUSOD), 2014 14th International Conference on* , vol., no., pp.173,174, 1-4 Sept. 2014.

[10] Rogalski, Antoni, Infrared Detectors. Boca Raton, FL: CRC Press, 2011. Print.

[11] Nibir K. Dhar, Ravi Dat and Ashok K. Sood (2013). *Advances in Infrared Detector Array Technology, Optoelectronics - Advanced Materials and Devices*, Prof. Sergei Pyshkin (Ed).

[12] Looker, Quinn. *Fabrication Process Development for High-Purity Germanium Radiation Detectors with Amorphous Semiconductor Contacts*. 2014. Print.

[13] Lutz, Gerhard. *Semiconductor Radiation Detectors Device Physics*. Berlin: Springer, 2007. Print.

[14] Knoll, Glenn F. *Radiation Detection and Measurement*. New York: Wiley, 1979. Print.

[15] Grundmann, Marius. *The Physics of Semiconductors: An Introduction including Devices and Nanophysics*. Berlin: Springer, 2006. Print.

[16] Devreese, J. T. *Electron Correlations in Solids, Molecules, and Atoms*. New York: Plenum :, 1983. Print.

[17] W. Shockely, *Jour. of Appl. Pysics* 9, 635 (1938).

[18] S. Ramo, Proc. of the I. R. E. 27, 584 (1939).

[19] Brajnik, D., and M. Tiringer. *Silicon Surface Barrier Detectors with Depletion Depth Greater than 2 Mm*. Ljubljana: IJS, 1968. Print.

[20] Evans, Robley Dunglison. *The Atomic Nucleus*. New York: McGraw-Hill, 1955. Print.

[21] ORTEC *High Purity Germanium (HPGe) Detector Manufacturing* available from ORTEC (Advanced Measurement Technologies Inc.).

[22] Drummond, William Eric. *Characteristics of High Purity Germanium and Silicon Radiation Detectors*. Ann Arbor, Mich.: U Microfilms, 1970. Print.

[23] Duffar, Thierry. *Crystal Growth Processes Based on Capillarity Czochralski, Floating Zone, Shaping and Crucible Techniques*. Chichester, U.K.: Wiley, 2010. Print.

[24] Mehrer, Helmut. *Diffusion in Solids: Fundamentals, Methods, Materials, Diffusion-controlled Processes*. Berlin: Springer, 2007. Print.

[25] *Extent of Environmental Contamination by Naturally Occurring Radioactive Material (NORM) and Technological Options for Mitigation*. Vienna: International Atomic Energy Agency, 2003. Print.

[26] J. Cl. Philippot, IEEE Trans. Nucl. Sci. NS-17/3 (1970) 446.

[27] G.A. Armantrout, *IEEE Trans. Nucl. Sci.*, NS-19, No. 3, 289 (1972).

[28] G. Bertolini, A Coche, Semiconductor Detectors. American Elsevier Publishing Company, Inc. New York, NY, 1968.

[29] Helmuth Spieler, *Semiconductor Detector Systems*, OUP Oxford, Aug 25, 2005.

[30] Tan, L.J.J.; Ong, D.S.G.; Jo Shien Ng; Chee Hing Tan; Jones, S.K.; Yahong Qian; David, J.P.R., "Temperature Dependence of Avalanche Breakdown in InP and InAlAs," *Quantum Electronics, IEEE Journal of* , vol.46, no.8, pp.1153,1157, Aug. 2010.

[31] *Physics with Chemically and Isotopically Pure Semiconductors*. Berkeley, Calif.: Lawrence Berkeley National Laboratory;, 1993. Print.

[32] M. J. Chen et al., Japanese Journal of Applied Physics 45, 6576-6588 (2006).

[33] Debertin, Klaus, and Richard G. Helmer. *Gamma and X-ray Spectrometry with Semiconductor Detectors*. Amsterdam: North-Holland;, 1988. Print.

[34] S. M. Sze, *Physics of Semiconductor Devices*. New York: Wiley-Interscience, 1969, p. 103.

[35] G. A. Armantrout, *Trapping and Tailing Effects in Ge(Li) Detectors*, Ph. D. Thesis, Purdue University, Lafayette, Ind., Aug 1969; Lawrence Livermore Laboratory, University of California, Livermore, Calif., Rept. UCRL-50485.

[36] ORTEC *The Best Choice of High Purity Germanium (HPGe) Detector* available from ORTEC (Advanced Measurement Technologies Inc.).

[37] Rosenberg, H. M. *The Solid State: An Introduction to the Physics of Solids for Students of Physics, Materials Science, and Engineering*. 3rd ed. Oxford: Oxford UP, 1988. Print.

[38] Rosenberg, H. M. *Low Temperature Solid State Physics: Some Selected Topics*. Oxford: Clarendon, 1963. Print.

[39] Lutz, Gerhard. *Semiconductor Radiation Detectors Device Physics*. Berlin: Springer, 2007. Print.

[40] Blair, J. M. *Charge Trapping in Semiconductor Detectors - Theoretical Approach*. 1971. Print.

[41] P. S. Barbeau, J. I. Collar, *Large-Mass Ultra-Low Noise Germanium Detectors: Performance and Applications in Neutrino and Astroparticle Physics*. arXiv:nucl-ex/0701012 (2007).

[42] G. H. Nakano, W. L. Imhof, IEEE Trans. Nucl. Sci., NS-18, No. 1, 258 (1971).

[43] ORTEC *Review of the Physics of Semiconductor Detectors* available from ORTEC (Advanced Measurement Technologies Inc.).

[44] E. Sakai, H. L. Malm and I. L. Fowler, *Semiconductor Nuclear Particle Detectors and Circuits (Proceedings of Gatlinburg Conference, May 1967)*, ed. By W. L. Brown, W. A. Higginbotham, G. L. Miller and R. L. Chase, NAS Publications, 1953 (1069).

[45] R. Pehl, E. Haller and R. Cordi, *IEEE Trans. Nucl. Sci.*, NS-20, No. 1, 494 (1973).

[46] H. D. Choi, *Signal Shapes from a Closed-ended Coaxial HPGe Detector,* Journal of the Korean Nuclear Society, Volume 29, No. 6, 451-458, 1997.

[47] G.H. Nakano, D.A.Simpson, and W.L. Imhof, *IEEE Trans. Nucl. Sci.* **NS-24**(1), 68 (1977).

[48] ORTEC *New Cooling Methods for HPGe Detectors and Associated Electronics,* available from ORTEC (Advanced Measurement Technologies Inc.).

[49] A. Lavietes, G. Mauger, E. Anderson, "*Electromechanically-Cooled Germanium Radiation Detector System*", UCRL-JC-129695, 1998.

[50] W. Parker, et al. "*A Portable System for Nuclear, Chemical, and High Explosives Identification*," UCRL-JC-132722, June 1999.

[51] US Patent Number 6,396,061.

[52] M. Burks, GeMini: *The Next Generation Mechanically-Cooled Germanium Spectrometer,* INMM: Institute of Nuclear Materials Management, July 2008.

[53] Princeton Gamma-Tech, *Nuclear Products Catalog*, available from Princeton Gamma-Tech.

[54] E. Broerman, D. Upp, T. Twomey, W. Little, "*Performance of a New Type of Electrical Cooler for HPGe Detector Systems*," Presented at the Institute of Nuclear Materials Management Conference, Indian Head, CA, 2001.

[55] Laszlo, Zoltan. *Adaptive Vibration Control Algorithm for Stirling-cycle Cryocoolers*. 1997. Print.

[56] *Initial Evaluation of a New Electromechanical Cooler for Safeguards Applications*. Washington, D.C: United States. Dept. of Energy, 2002. Print.

[57] ORTEC *Micro-Detective-HX; Enhanced Capability, Ultra-Ligh, High-Fidelity, Hand- held Radioisotope Identifier*, available from ORTEC (Advanced Measurement Technologies Inc.).

[58] *GeMini the Next Generation Mechanically-Cooled Germanium Spectrometer*. Washington, D.C.: United States. Dept. of Energy, 2008. Print.

[59] Romer, Alfred. *The Restless Atom; the Awakening of Nuclear Physics*. Garden City, N.Y.: Anchor ; Available through Wesleyan UP, Columbus, Ohio, 1960. Print.

[60] Chen, E. C. M., and E. S. D. Chen. *The Electron Capture Detector and the Study of Reactions with Thermal Electrons*. Hoboken, N.J.: Wiley-Interscience, 2004. Print.

[61] *High-Energy Beta Decay of Light Elements*. Washington, D.C.: U.S. Atomic Energy Commission;, 1958. Print.

[62] *Mechanisms of Interaction of Radiation with Matter*. Washington, D.C.: United States. Dept. of Energy ;, 1992. Print.

[63] Willett, Edward. *The Basics of Quantum Physics: Understanding the Photoelectric Effectand Line Spectra*. New York: Rosen Pub. Group, 2005. Print.

[64] Wissmann, Frank. *Compton Scattering and the Structure of the Nucleon*. 1. Aufl. ed. Göttingen: Cuvillier, 2001. Print.

[65] Wick, G. C. *Detection of [gamma]-ray Polarization by Pair Production*. Berkeley, Ca.: [Lawrence] Radiation Laboratory. ;, 1950. Print.

[66] Robinson, James W. *Practical Handbook of Spectroscopy*. Boca Raton: CRC, 1991. Print.

[67] *Compton Scattering*. Livermore, Calif: Lawrence Livermore National Laboratory;, 1979. Print.

[68] Williams, Brian G. *Compton Scattering: The Investigation of Electron Momentum Distributions*. New York: McGraw-Hill International, 1977. Print.

[69] Venverloo, L. A. J. *Practical Gamma Spectroscopy*. Eindhoven: Philips Gloeilampenfabrieken, 1963. Print.

[70] Web. 20 Mar. 2015. <http://upload.wikimedia.org/wikipedia/en/9/9a/Split_Stirling_Cooler.jpg>.

[71] Organ, Allan J. *Stirling and Pulse-tube Cryo-coolers the inside Story*. London: Professional Engineering Pub., 2005. Print.

[72] Manmohan Singh, Mukesh Sadana, Sunil Sachdev, and Gaurav Pratap, *Development of Miniature Stirling Cryocooler Technology for Infrared Focal Plane Array,* Defence Science Journal, Vol. 63, No. 6, November 2013.

[73] S.A. Collins, A. H. von Flotow, J. D. Paduano, Adaptive Vibration Cancellation for Split-Cycle Stirling Cryocoolers, Plenum Press, New York, NY, 1994. Print.

[74] Canberra, *Germanium Detectors User's Manual*, Canberra Industries, Inc. 800 Research Parkway, Meriden, CT, 2003.

[75] Russell E. Gritzo, Kevin R. Jackman, Steven R. Biegalski, *A Software Package Using a Mesh-grid Method for Simulating HPGe Detector Efficiencies,* Methods in Analytical Radiochemistry (MARC) VIII.

[76] "IEEE Test Procedures for Germanium Detectors for Ionizing Radiation," ANSI/IEEE Standard 325-1986.

[77] ANSI N42.34-2006: *American National Standard Performance Criteria for Hand-Held Instruments for the Detection and Identification of Radionuclides*.

[78] Weiqi Huang; Yigang Yang; Yuanjing Li; Yi Liu; Yang Tian; Qiyan Zheng; Jianbo Yang, "*Detection of high-Z materials using 7MeV X-rays scattering*," *Nuclear Science*.

[79] *Field Deployable Gamma Radiation Detectors for DHS Use*. Oak Ridge, Tenn.: Distributed by the Office of Scientific and Technical Information, U.S. Dept. of Energy, 2007. Print.

[80] Chen, ChuangRong. *Theory and Design of a Split-Type Stirling Cooler*. 2013. Print.

[81] Euler, Bruce Alfred. *Approximate Methods for Calculation of Intrinsic Total Absorption and Double-escape Peak Efficiencies for Ge(Li) Detectors*. 1969. Print.

[82] Tavendale, A. J. *A Large, Coaxial, Lithium-drift Germanium Diode for Gamma-Ray Spectroscopy*. Lucas Heights, N.S.W.: Research Establishment, Australian Atomic Energy Commission, 1965. Print.

[83] M. E. Cournoyer, J. M. Pecos, S.D. Chunglo, C. Bonner, R.J. Maez, *Pulse Tube Refrigeration for Detectors*, Journal of Radioanalytical and Nuclear Chemistry, Vol. 1, April 2012.

[84] D. L. Upp et al, *Journal of Radioanalytical and Nuclear Chemistry*, Vol. 276, 2008.

Appendix

Table A.1: FWHM and FW(0.2)M test results for detector 1.

FWHM Test and Measurement Data				
Detector Temperature (K)	**(@122 keV)**		**(@ 1332.5 keV)**	
	FWHM (keV)	**FW(0.2)M (keV)**	**FWHM (keV)**	**FW(0.2)M (keV)**
100.00	2.01	3.25	2.56	4.05
105.00	1.96	3.16	2.38	3.82
110.00	1.84	2.83	2.26	3.60
115.00	1.66	2.57	2.21	3.42
120.00	1.57	2.45	2.18	3.32
125.00	1.49	2.34	2.11	3.20
130.00	1.37	2.16	2.03	3.14
135.00	1.35	2.09	1.98	3.09
140.00	1.34	2.10	1.96	3.02
145.00	1.30	2.05	1.99	3.07
150.00	1.35	2.13	2.03	3.13
155.00	1.40	2.21	2.04	3.16
160.00	1.55	2.43	2.19	3.27
165.00	1.82	2.85	2.35	3.57
170.00	2.23	3.44	2.62	4.15
175.00	2.92	4.51	3.07	4.89
180.00	4.18	6.40	4.38	6.74

Table A.2: FWHM and FW(0.2)M test results for detector 2.

FWHM Test and Measurement Data				
Detector Temperature (^{o}K)	**(@122 keV)**		**(@ 1332.5 keV)**	
	FWHM	**FW(0.2)M**	**FWHM**	**FW(0.2)M**
104.90	1.28	2.01	1.94	2.92
110.00	1.34	2.05	1.95	2.94
115.00	1.36	2.09	2.01	3.02
120.00	1.38	2.12	2.04	3.10
125.00	1.46	2.23	2.06	3.20
130.00	1.54	2.36	2.13	3.28
135.00	1.60	2.47	2.21	3.40
139.90	1.75	2.65	2.36	3.60
144.90	2.01	3.08	2.54	3.85
149.90	2.38	3.61	2.89	4.38
154.80	2.89	4.21	3.48	5.27
159.80	3.40	4.77	4.29	6.68
164.70	4.00	5.37	5.63	8.66
170.00	4.80	6.12	7.10	10.60

Table A.3: FWHM and FW(0.2)M test results for detector 3.

FWHM Test and Measurement Data				
Detector Temperature (^oK)	**(@122 keV)**		**(@ 1332.5 keV)**	
	FWHM	**FW(0.2)M**	**FWHM**	**FW(0.2)M**
100.00	1.56	2.42	2.31	3.64
105.00	1.49	2.31	2.27	3.59
109.60	1.50	2.25	2.25	3.51
114.50	1.50	2.26	2.20	3.48
119.30	1.51	2.18	2.19	3.40
124.90	1.52	2.20	2.31	3.58
130.00	1.67	2.40	2.64	4.08
134.60	2.20	3.21	2.92	4.45
139.80	2.89	4.18	3.81	5.90
144.80	3.60	5.12	4.70	7.40
149.70	4.31	6.11	5.88	8.99
154.40	5.11	7.10	6.89	10.65

Table A.4: FWHM and FW(0.2)M test results for detector 4.

FWHM Test and Measurement Data				
Detector Temperature (K)	**(@122 keV)**		**(@ 1332.5 keV)**	
	FWHM keV	**FW(0.2)M keV**	**FWHM keV**	**FW(0.2)M keV**
99.10	1.20	1.76	2.28	3.50
104.80	1.18	1.75	2.26	3.47
109.90	1.16	1.72	2.33	3.51
115.00	1.17	1.71	2.35	3.65
120.00	1.18	1.72	2.44	3.87
124.90	1.19	1.75	2.62	4.02
130.20	1.21	1.76	2.90	4.41
134.80	1.25	1.79	3.16	4.66
139.80	1.42	2.12	3.60	5.32
145.20	1.80	2.72	4.35	6.15
150.40	2.40	3.30	5.20	7.12

Table A.5: Energy resolution for detector 1 with cooler on and cooler off and the difference of the two measurements for each respective detector temperature. In addition, the cooler drive voltage has been included for reference.

Detector 1 Energy Resolution							
Drive Voltage (V)	**Detector Temp (K)**	**(@122 keV) Cooler On**		**(@122 keV) Cooler Off**		**(@122 keV)**	
		FWHM (keV)	**FW(0.2)M (keV)**	**FWHM (keV) off**	**FW(0.2)M (keV) off**	**Δ FWHM**	**Δ FW(0.2)M**
4.36	100.00	2.01	3.25	1.08	1.67	0.93	1.58
4.14	105.00	1.96	3.16	1.09	1.70	0.87	1.46
3.91	110.00	1.84	2.83	1.08	1.66	0.76	1.17
3.69	115.00	1.66	2.57	1.06	1.65	0.60	0.92
3.67	120.00	1.57	2.45	1.09	1.70	0.48	0.75
3.65	125.00	1.49	2.34	1.06	1.66	0.43	0.68
3.16	130.00	1.37	2.16	1.06	1.64	0.31	0.52
3.06	135.00	1.35	2.09	1.06	1.65	0.29	0.44
2.93	140.00	1.34	2.10	1.07	1.66	0.27	0.44
2.82	145.00	1.30	2.05	1.10	1.73	0.20	0.32
2.73	150.00	1.35	2.13	1.16	1.73	0.19	0.40
2.65	155.00	1.40	2.21	1.25	1.95	0.15	0.26
2.56	160.00	1.55	2.43	1.43	2.22	0.12	0.21
2.47	165.00	1.82	2.85	1.74	2.72	0.08	0.13
2.40	170.00	2.23	3.44	2.21	3.45	0.02	-0.01
2.33	175.00	2.92	4.51	2.91	4.49	0.01	0.02
2.25	180.00	4.18	6.40	4.17	6.39	0.01	0.01

Table A.6: Energy resolution for detector 2 with cooler on and cooler off and the difference of the two measurements for each respective detector temperature. In addition, the cooler drive voltage has been included for reference.

Detector 2 Energy Resolution

Drive Voltage	Detector Temp (K)	(@122 keV) Cooler On		(@122 keV) Cooler Off		(@122 keV)	
		FWHM (keV)	FW(0.2)M (keV)	FWHM (keV)	FW(0.2)M (keV)	Δ□ FWHM	Δ□FW(0.2M
4.72	104.90	1.28	2.01	0.98	1.59	0.30	0.42
4.64	110.00	1.34	2.05	1.07	1.68	0.27	0.37
4.32	115.00	1.36	2.09	1.11	1.77	0.25	0.32
4.07	120.00	1.38	2.12	1.18	1.88	0.20	0.24
3.92	125.00	1.46	2.23	1.32	2.06	0.14	0.17
3.72	130.00	1.54	2.36	1.43	2.22	0.11	0.14
3.52	135.00	1.60	2.47	1.54	2.38	0.06	0.09
3.32	139.90	1.75	2.65	1.73	2.58	0.02	0.07
3.12	144.90	2.01	3.08	2.00	3.06	0.01	0.02
2.92	149.90	2.38	3.61	2.37	3.59	0.01	0.02
2.88	154.80	2.89	4.21	2.88	4.19	0.01	0.03
2.52	159.80	3.40	4.77	3.40	4.75	0.00	0.02
2.28	164.70	4.00	5.37	4.00	5.36	0.00	0.01
2.12	170.00	4.80	6.12	4.80	6.11	0.00	0.01

Table A.7: Energy resolution for detector 3 with cooler on and cooler off and the difference of the two measurements for each respective detector temperature. In addition, the cooler drive voltage has been included for reference.

Detector 3 Resolution							
Drive Voltage	**Detector Temperature (K)**	**(@122 keV) Cooler On**		**(@122 keV) Cooler Off**		**(@122 keV)**	
		FWHM (keV)	**FW(0.2)M (keV)**	**FWHM (keV) off**	**FW(0.2)M (keV) off**	**Δ FWHM**	**Δ FW(0.2)M**
9.80	89.90	1.58	2.48	1.07	1.81	0.51	0.67
9.26	91.40	1.56	2.42	1.08	1.78	0.49	0.64
8.73	107.70	1.49	2.31	1.03	1.72	0.46	0.59
8.19	109.60	1.50	2.25	1.09	1.72	0.41	0.53
7.65	114.50	1.50	2.26	1.13	1.79	0.37	0.47
7.12	117.30	1.51	2.18	1.19	1.80	0.32	0.38
6.58	122.50	1.52	2.20	1.20	1.84	0.32	0.36
6.04	130.00	1.67	2.40	1.47	2.18	0.20	0.23
5.51	134.60	2.20	3.49	2.10	3.38	0.10	0.11
4.97	139.80	3.00	4.55	2.95	4.49	0.05	0.06
4.43	144.80	3.60	5.38	3.60	5.38	0.00	0.00
3.90	149.70	4.10	5.90	4.10	5.90	0.00	0.00
3.36	154.40	4.59	6.65	4.59	6.65	0.00	0.00
2.82	160.50	5.49	7.70	5.49	7.70	0.00	0.00
2.29	170.90	6.89	9.61	6.89	9.61	0.00	0.00
1.75	174.80	7.45	10.21	7.45	10.21	0.00	0.00

Table A.8: Energy resolution for detector 4 with cooler on and cooler off and the difference of the two measurements for each respective detector temperature. In addition, the cooler drive voltage has been included for reference.

Detector 4 Energy Resolution							
Drive Voltage	**Detector Temperature (K)**	**(@122 keV) Cooler On**		**(@122 keV) Cooler Off**		**(@122 keV)**	
		FWHM (keV)	**FW(0.2)M (keV)**	**FWHM (keV) off**	**FW(0.2)M (keV) off**	**Δ FWHM**	**Δ FW(0.2)M**
7.81	99.10	1.20	1.76	0.76	1.15	0.44	0.61
6.71	104.80	1.18	1.75	0.83	1.19	0.36	0.57
5.86	109.90	1.16	1.72	0.89	1.22	0.27	0.50
5.52	115.00	1.17	1.71	0.95	1.32	0.22	0.39
5.29	120.00	1.18	1.72	1.03	1.44	0.15	0.28
5.07	124.90	1.19	1.75	1.07	1.51	0.12	0.24
4.88	130.20	1.21	1.76	1.11	1.58	0.10	0.18
4.66	134.80	1.25	1.79	1.25	1.79	0.00	0.00
4.44	139.80	1.42	2.12	1.42	2.12	0.00	0.00
4.21	145.20	1.80	2.72	1.80	2.72	0.00	0.00
3.98	150.40	2.40	3.30	2.40	3.30	0.00	0.00

Vita

Joseph Benjamin McCabe was born in Colorado Springs, Colorado on November 6, 1977. In May of 2001, Joseph earned a Bachelor of Science Degree in Mechanical Engineering with a focus in advanced thermodynamic heat transfer and fluid dynamics from Minnesota State University. Immediately after graduation, Joseph joined Kato Engineering (an Emerson Electric Company) in Mankato Minnesota. Kato Engineering specializes in the design and manufacture of generators (alternators), motor-generator sets, and controls used for prime, standby, and peak-shaving power applications. During his time at Kato Engineering, Joseph worked as a mechanical engineer and project manager for the military sales team. In 2003, Joseph continued his professional career with a position of director of engineer at Kato Engineering's sister company, Leroy Somer in Lexington, Tennessee. In this position, Joseph gained extensive experience in electromechanical systems and was fascinated with the interdependence of the electrical and mechanical portions of the alternator designs. Joseph acted on this fascination through continued education at Iowa State University where he earned dual master's degrees in mechanical engineering and electrical engineering. During his period as director of engineering with Emerson Electric Joseph learned a very valuable lesson that was perhaps most effectively manifested in the life of Steve Jobs as CEO of Apple. The most significant advancements in business and technology can be mutually inclusive and synergistic. In 2005, Joseph continued his education at Union University in Jackson, Tennessee where he earned his Masters of Business Administration with a focus in Finance and Executive Management. Driven primarily by a desire and need to make more significant impacts in his career, Joseph took a position as a Division Vice President at Advanced Measurement Technology Inc. in Oak Ridge, Tennessee. It was in this position that Joseph was introduced to the field of radiation and nuclear detection and identification. In his role as head of research and development, Joseph lead a highly-talented research and development team in the conceptualization, design, and manufacture of; high resolution germanium detectors, pulse-processing electronics, spectrometry instruments and systems for measuring energy and time distributions of gamma rays, and neutrons. Fascinated by the technology, Joseph enrolled at the University of Tennessee, Knoxville and set out to earn his Master of Science in Nuclear Engineering. In May of 2014, Joseph was successful in earning his Master of Science in Nuclear Engineering with a major concentration in radiological engineering. Joseph's masters research focused on the design and test of high purity germanium detector systems with a person interest in radioisotope identification devices (RIIDs). Encouraged by his major professor, Dr. Hayward and the University of Tennessee, Knoxville, Joseph continued his education in the field of Nuclear Engineering and began working on his Doctor of Philosophy in Nuclear Engineering. This PhD study and research excellently coincided with Joseph's continued position as Division Vice President at Advanced Measurement Technology. Joseph earned his Doctor of Philosophy in Nuclear Engineering at the University of Tennessee at Knoxville in May of 2015.